

# FOURIER TRANSFORM TECHNIQUES FOR FAST PHYSICAL OPTICS MODELING

DISSERTATION

FOR THE ACQUISITION OF THE ACADEMIC TITLE  
*doctor rerum naturalium* (Dr. rer. Nat.)

submitted to the Council of the Faculty of Physics and Astronomy  
of the *Friedrich-Schiller-Universität Jena*

by M. Sc. Zongzhao Wang  
born in Tianjin, China, on 20 December 1989

**Supervisor:** Prof. Dr. Frank Wyrowski, Friedrich-Schiller-Universität Jena

**Reviewer:** Prof. Dr. Jürgen Jahns, FernUniversität in Hagen

**Reviewer:** Prof. Dr. Jari Turunen, University of Eastern Finland

**Date of the Disputation:** 09 February 2021

**Dissertation, Friedrich-Schiller-Universität Jena, 2021**

# ABSTRACT

Motivated by the ever-growing demand for high-quality optical systems, the field tracing approach becomes increasingly significant in physical-optics modeling. Instead of employing a universal Maxwell solver for the whole system, we follow the concept of field tracing, to decompose the system into regions and apply various regional Maxwell solvers. The field solvers may work in the spatial ( $x$ ) or the spatial frequency ( $k$ ) domain. To enable the connection of different solvers and functions, the transforming between the  $x$  and  $k$  domains is a crucial step.

Since the Fourier transform gives the connection between these two domains, it becomes paramount to optimize the Fourier-transforming step. The Fast Fourier Transform (FFT) constitutes a huge improvement on the original Discrete Fourier Transform (DFT), since its (the former's) numerical effort is approximately linear on the sample number of the function to be transformed. However, this orders-of-magnitude improvement in the number of operations required can fall short in optics, where the tendency is to work with field components that present strong wavefront phases. In this work, we propose two innovative Fourier transform techniques. The Semi-analytical Fourier Transform (SFT) is a rigorous approach without any approximation, in which we avoid the sampling of quadratic phases, handling them analytically instead. The homeomorphic Fourier transform (HFT) is an approximate approach, but highly efficient and accurate for fields with intense wavefront phases.

Furthermore, we investigate these Fourier transform techniques (FFT, SFT, and HFT) applied to the problem of light propagation, to verify their influence on the system modeling. Consequently, the unified free space propagation operator is concluded. All proposed techniques in this thesis are implemented and diverse numerical examples are presented to illustrate their vast potential.

# ZUSAMMENFASSUNG

Motiviert durch die steigende Nachfrage an hochqualitativen optischen Systeme wird der "Field Tracing" Ansatz stetig signifikanter im Bereich der physikalisch-optischen Modellierung. Anstatt einen allgemeinen Lösungsalgorithmus für das gesamte System zu verwenden, folgen wir den Ansatz des "Field Tracings", bei dem das System in verschiedene Regionen aufgeteilt und anschließend für jede Region ein passender "Maxwell Solver" verwendet wird. Diese Algorithmen können für die Raum( $x$ )- oder die Raumfrequenz-Domäne ( $k$ ) definiert sein. Um verschiedene Lösungsalgorithmen verbinden zu können sind entsprechende Transformationen zwischen  $x$ - und  $k$ - Domäne von entscheidender Bedeutung.

Da die Fourier-Transformation bekanntermaßen die Verbindung zwischen diesen beiden Domänen beschreibt, ist es entscheidend diese Art der Operationen zu optimieren. Die "Fast Fourier Transformation" (FFT) stellt dabei eine deutliche Verbesserung gegenüber der originalen "Discrete Fourier Transform" (DFT) dar, weil der numerischen Aufwand von erstere approximiert linear mit der Zahl der verwendeten Sampling-Punkten der zu transformierenden Funktion steigt. Allerdings kann diese um Größenordnungen reduzierte Anzahl an notwendigen Operationen für Anwendungen im Bereich der Optik zu kurz greifen, da dort tendenziell eher mit Feld-Komponenten gearbeitet wird, die starke Wellenfronten aufweisen. In dieser Arbeit stellen wir zwei neue, innovative Fourier Transformationen vor. Die "Semi-Analytical Fourier Transform" (SFT) ist ein rigoroser Ansatz, bei welchem das Absampeln der quadratischen Phase vermieden und diese stattdessen analytisch berechnet wird. Die homeomorphe Fourier Transformation (HFT) ist ein approximativer Ansatz, der allerdings hoch effizient und akkurat für Felder mit ausgeprägter Wellenfront Phase verwendet werden kann.

Außerdem untersuchen wir diese Fourier-Transformationen (FFT, SFT, HFT) angewendet auf das Problem der Lichtpropagation, um ihren Einfluss auf die Systemmodellierung zu klären. Folglich wird ein "Unified Free Space Operator" definiert. Alle vorgestellten Techniken in dieser Thesis sind implementiert und diverse numerische Experimente werden präsentiert, um ihr Potenzial zu verdeutlichen.

## CONTENTS

---

1	INTRODUCTION	3
2	SEMI-ANALYTICAL FOURIER TRANSFORM	9
2.1	Theorem derivation . . . . .	10
2.1.1	Semi-analytical Fourier transform . . . . .	10
2.1.2	Inverse semi-analytical Fourier transform . . . . .	15
2.1.3	Hybrid semi-analytical Fourier transform and its inverse operation . . . . .	16
2.1.4	Handling of the quadratic phase . . . . .	19
2.1.5	Validity condition and the numerical criterion . . . . .	21
2.2	Numerical examples . . . . .	23
2.2.1	Fourier transform of a field with a purely quadratic phase . . . . .	24
2.2.2	Fourier transform of a field with a spherical phase . . . . .	26
2.2.3	Fourier transform of a field with a general wavefront phase . . . . .	29
3	HOMEOMORPHIC FOURIER TRANSFORM	31
3.1	Theorem derivation . . . . .	32
3.1.1	Homeomorphic Fourier transform . . . . .	32
3.1.2	The inverse homeomorphic Fourier transform . . . . .	37
3.1.3	Validity condition and the numerical criterion . . . . .	39
3.1.4	Pointwise Fourier transform in the case of a non-bijective wavefront phase . . . . .	42
3.2	Numerical examples . . . . .	45
3.2.1	Fourier transform of a field with spherical phase . . . . .	45
3.2.2	Fourier transform of a field with a simple aberrant phase . . . . .	51
3.2.3	Fourier transform of a field with a general, bijective, wavefront phase . . . . .	53
3.2.4	Fourier transform of a field with a non-bijective wavefront phase . . . . .	56
4	APPLICATION IN THE FREE SPACE PROPAGATION	65
4.1	Unified free space propagation operator via the k-domain . . . . .	66

4.1.1	Propagation operator between parallel planes . . . . .	67
4.1.2	Extension to the arbitrarily oriented planes . . . . .	68
4.1.3	Automatic selection of the Fourier transform techniques . .	70
4.2	Generalization of two <b>diffraction integrals</b> . . . . .	72
4.2.1	Generalized Debye integral . . . . .	72
4.2.2	Generalized far-field integral . . . . .	76
4.3	Interpretation of two fast <b>propagation operators</b> . . . . .	81
4.3.1	<b>Pointwise operator: ray tracing algorithm</b> . . . . .	81
4.3.2	<b>Paraxial domain operator: Fresnel integral</b> . . . . .	84
4.4	Numerical examples . . . . .	87
4.4.1	Focusing of an aberrant field . . . . .	88
4.4.2	Propagation of an aberrant divergent wave . . . . .	91
4.4.3	Propagation of the light field to the inclined planes . . . .	97
5	SUMMARY AND OUTLOOK . . . . .	99
A	APPENDIX . . . . .	101
A.1	Homeomorphism condition for the smooth phase function . . . .	101
	BIBLIOGRAPHY . . . . .	107

## INTRODUCTION

---

With the ongoing progress in optical manufacturing and processing, there is a tendency for optical systems to become ever more miniaturized and precise [1]. This is accompanied by an increasing demand for the capability to model and analyze these sophisticated systems [2–4]. Nowadays, conventional ray optics is nowhere near enough to sustain the continued innovation in optical modeling and design [5–7]. Physical optics, based on Maxwell’s equations, enables the inclusion of both electromagnetic field properties and wave properties, e.g., interference, coherence, and diffraction [8–10]. However, one widespread misunderstanding has still not been completely overcome: that physical optics performs slowly in simulation. This is due to the fact that physical-optics is still associated in the field with the indiscriminate application of a single universal Maxwell solver, e.g., the Fourier Modal Method (FMM) [11–14] and the Finite Element Method (FEM) [15–17], to the modeling of an entire complicated system.

During the last two decades, Wyrowski et al. have proposed and refined the concepts of field tracing [18–20]. Driven by these innovative notions, fast physical optics becomes possible with, in some cases, even faster simulations than ray tracing can provide. The field-tracing strategy overcomes the numerical drawbacks of the single universal Maxwell solver by tearing the system into sub-domains. As shown in Fig. 1, each sub-domain can be modeled by a different method. For example, there is a system containing both gratings and lenses. To know the fields before and after interaction with the different optical components in the system, we can employ FMM for the gratings, the Local-Plane-Interface Approximation (LPIA) [21, 22] for the lenses, and the free-space propagation operator for the spaces in-between. In short, the field tracing concept enables the smooth combination of different field solvers and achieves unified modeling. Selected modeling techniques need to offer convincing arguments in terms of both efficiency and accuracy. They may either work in the spatial ( $x$ )

domain or the spatial frequency ( $k$ ) domain. As a consequence, we can see that one technique in particular is frequently used in the field tracing diagram to interconnect different field solvers, i.e., the Fourier transform operation. Typically, the modeling of sophisticated systems involves various field solvers and requires multiple trips between the different domains [23, 24]. The transforming between the  $x$  and  $k$  domains is a crucial modeling step, and the performance of the Fourier transform technique will significantly influence the efficiency of the simulation.

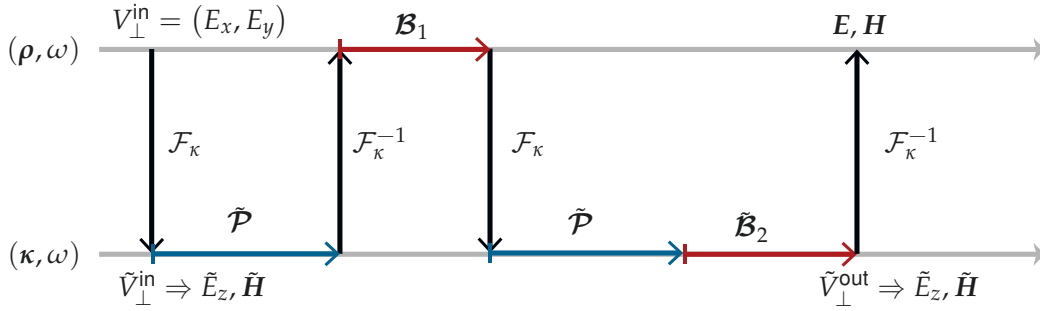


Figure 1: Illustration of the physical-optics modeling of a light path by a field-tracing diagram.  $\tilde{\mathcal{P}}$  indicates the free-space propagation operator in the  $k$  domain.  $\mathcal{B}$  and  $\tilde{\mathcal{B}}$  denote the physical response of an optical element in the  $x$  or in the  $k$  domain respectively. The entire process includes the handling of all six electromagnetic field components.

The Fourier transform is one of the essential mathematical tools for computing the frequency representation of a given function [25–27]. It is widely used in different disciplines, like image processing, communications, astronomy, as well as optical modeling and design. Considering the usage of the Fourier transform in practice, we come to the question of the different computational implementations of the mathematical operation. The brute-force approach that stems from simply discretizing the Fourier integral is commonly referred to as the Discrete Fourier Transform (DFT) [28] and presents a complexity of  $\mathcal{O}(N^2)$  for a function with  $N$  sampling points. The computational effort of the operation is already greatly reduced by the Fast Fourier Transform (FFT) [29, 30], the most famous version of which is the one introduced by Cooley and Tukey, and which requires  $\mathcal{O}(N \log N)$  individual computations. However, even this orders-of-magnitude improvement in the number of operations required can fall short



in optics, where the tendency is to work with field components that present **strong wavefront phases**: this translates, as per the Nyquist-Shannon sampling theorem [31, 32], into a **huge sample number**; that is the case for a spherical wave with moderately high numerical aperture (NA). Only **the most paraxial fields can be feasibly Fourier-transformed with the FFT**. This caveat for the practicality of the FFT in optics comes as a consequence of the need to resolve the complex amplitude with a  $2\pi$ -modulo (or wrapped) phase [33–35].

Since the same numerical issue caused by the  $2\pi$ -modulo phase also occurs in typical optical simulation scenes, e.g., propagation of the light field, our initial idea of the advanced Fourier transform is inspired by some well-demonstrated algorithms. The optics community recognizes a series of papers based on the Chirp Z-transform (CZT) [36–38]. This technique is established on the convenient property whereby the quadratic phase term in the Fourier transform is extracted. It can be used to advantage in terms of numerical effort since, according to convolution theory, a single Fourier-transform operation can be replaced by a pair of Fast Fourier Transform steps, which, even together, require a much lower sampling number. Another useful trick included in this technique is that the Fourier transform of a quadratic phase turns out to also be quadratic. However, the discussion of this quadratic-phase trick tends to be limited to one-dimensional ( $x^2$ ) or, at most, separable problems ( $x^2, y^2$ ), without including the cross term  $xy$  which constitutes a prominent part of diffraction theory. What's more, in some cases, the scaling factors of the quadratic phase term are deduced via the paraxial approximation (which mathematically translates as using the Taylor expansion of a spherical phase around its center, instead of the full spherical phase). Consequently, **the performance and accuracy of any approaches thus limited may suffer in the face of non-paraxial configurations**. Enlightened by this notable work, we introduce an algorithm, which we have named “**semi-analytical Fourier transform**” [39], whose aim is to efficiently **compute the Fourier transform of a field without reverting to any approximations**. We describe the full derivation in Chapter 2, taking as our starting point the **mathematical definition of the Fourier transform** and using convolution theory.

Although the semi-analytical Fourier transform is a rigorous algorithm and enables certain relief of the sampling effort, its **scope of application** is restricted to the problem **caused by quadratic phases**. This kind of advantage can promptly

fail for fields with more general wavefront phases. Therefore, we explore, in parallel, a different line of thought. From the mathematical point of view, the Fourier-transform integrals are rapidly oscillating functions in the case of strong wavefront phases. There is a mathematical method, working on the basis of an asymptotic approximation to integrals of such rapidly varying functions, which occasionally comes up in wave theory, applied usually with the aim of obtaining an analytical solution to a specific problem (as is the case with the Debye integral): the Method of Stationary Phase (MSP) [40, 41]. Jakob J. Stamnes already revealed the connection between waves and rays with the application of the Method of Stationary Phase in his publication [42]. Performing the method of stationary phase in the Fourier transform integral, we can see the Fourier integral operator reduces mathematically to a pointwise operation, a behavior of the Fourier transform which was already discussed by Bryngdahl in the context of geometric transformations in optics [43]. In Chapter 3, the full derivation process is presented. We named this fast, pointwise, approximated and accurate Fourier transform operation “homeomorphic Fourier transform” [44, 45]. Different from the semi-analytical Fourier transform, there is no constraint on the type of the wavefront phase. Furthermore, to ensure a good level of accuracy, we also derive the application conditions of the homeomorphic Fourier transform and deduce some reasonable criteria for practical simulations.

Counting also the FFT, we have at our disposal three advanced Fourier transform techniques in total. It is meaningful to utilize these novel tools when solving real modeling tasks. However, instead of more sophisticated systems, in the present work we intend to start our investigation from the most fundamental and widely used modeling scenario: the problem of light propagation in free space (where, by “free space”, we understand any isotropic and homogeneous medium) [46, 47]. It is one of the most crucial parts of physical-optics modeling and design. Any improvements in accuracy and speed are helpful. On this problem, there are two rigorous Maxwell’s solvers, the method of the angular spectrum of plane waves (SPW) [48, 49] and the Rayleigh-Sommerfeld integral [50–54], which work, respectively, in the  $k$  and the  $x$  domain. However, since both rigorous approaches are integral operators, when the propagating field presents an intense wavefront phase, they would suffer from massive numerical effort [55–57]. Thus, various approximate diffraction integrals were developed to deal with

different specific types of configurations [58–61]. For instance, the Debye integral is commonly used to efficiently tackle the problem of focusing light in lens design, and the far-field integral is used to calculate the diffraction pattern at large distances [62, 63]. Despite both the derivation process and the application scope of these approximate operators having already been discussed in the literature, the comprehensive understanding of their intrinsic connection is still missing. In Chapter 4, we propose a unified free-space propagation operator via the k-domain analysis alongside the advanced Fourier transform techniques. The unified operator follows directly from the SPW approach by performing an automatic selection of the Fourier transform techniques in different propagation scenes. Also, the propagation between non-parallel planes is taken into account [64, 65]. To drive the point home, we generalize and interpret several well-known and influential diffraction integrals and propagation operators, e.g., the Debye integral [66, 67], the far-field integral [68, 69] and the Fresnel integral [70, 71]. We have proven that these diffraction integrals can be understood as a special case of the unified propagation operator. All techniques drawn from this work are implemented in the physical-optics modeling and design software VirtualLab Fusion [72]. In each chapter, simulation results are presented alongside the theoretical derivation to illustrate the potential of the Fourier transform techniques as well as the unified free-space propagation operator.



## SEMI-ANALYTICAL FOURIER TRANSFORM

In this chapter, we propose an algorithm, which we have named “semi-analytical Fourier transform”, whose aim is to efficiently carry out the Fourier transform of a field without reverting to any approximations. The full derivation process is presented in section 2.1. The idea of the proposed method is to extract the quadratic phase from the input field/spectrum with the help of some numerical evaluation techniques, e.g., the Gaussian Newton fitting method [73, 74] or the Levenberg-Marquardt fitting method (LMM) [75]. By grouping the rest of the phase alongside the amplitude part, we obtain the residual field whose sampling effort must be less than the original complete field. Then, the semi-analytical Fourier transform (SFT) can be used to replace the regular FFT of the fully sampled field by two FFTs of complex functions that require much fewer sampling points. The sampling issue is entirely dependent on the residual field so that in contrast to the regular FFT, the numerical effort is reduced significantly. Also, by combining the regular FFT and the semi-analytical Fourier transform, we develop the so-called hybrid semi-analytical Fourier transform algorithm, which generalizes the usage of the semi-analytical Fourier transform to the field with a one-dimensional quadratic phase. In section 2.2, we consider the application of the algorithm to numerical simulations. Simulation results illustrate the vast potential of the semi-analytical Fourier transform. Two fundamental simulation scenes, free-space propagation of the higher-order Gaussian mode and calculation of the  $E_z$  component, are discussed in relation to the proposed technique. On the other hand, different fitting methods are taken into account in the numerical simulations to extract a polynomial of the second order from said general phase component. According to the simulation results, we obtain a more precise awareness about how to reduce the sampling effort for fields with a general wavefront phase.

## 2.1 THEOREM DERIVATION

### 2.1.1 Semi-analytical Fourier transform

We assume a general electromagnetic field at a certain plane

$$V_\ell(\boldsymbol{\rho}) = |V_\ell(\boldsymbol{\rho})| \exp[i\gamma_\ell(\boldsymbol{\rho})] , \quad (1)$$

where the index  $\ell = 1, \dots, 6$  is used to account all six electromagnetic field components  $\{E_x, E_y, E_z, H_x, H_y, H_z\}$ . In our notation,  $\mathbf{r} = (x, y, z)$  and  $\boldsymbol{\rho} = (x, y)$  are respectively the position vector and its projection onto the transversal plane. As shown in Eq. (1), the complex amplitude  $V_\ell(\boldsymbol{\rho})$  can be written into two parts, amplitude,  $|V_\ell(\boldsymbol{\rho})|$ , and phase,  $\exp[i\gamma_\ell(\boldsymbol{\rho})]$ .

As we all know that the complex exponential function can be written into two trigonometric functions, namely  $\exp[i\gamma_\ell(\boldsymbol{\rho})] = \cos \gamma_\ell(\boldsymbol{\rho}) + i \sin \gamma_\ell(\boldsymbol{\rho})$ . Because of the periodic nature of the trigonometric functions, all phase points are constrained to the range  $(-\pi, \pi]$ . It is referred to as a “ $2\pi$ -wrapped phase” or “ $2\pi$ -modulo phase”. Generally, a “smooth” ( $C^1$ ) phase function becomes jaggedly discontinuous when it is wrapped. It is important to remark that as the slope of the original unwrapped phase function increases, the teeth of its wrapped counterpart become denser. According to the Shannon-Nyquist theorem that at least two sampling points must be used per period of the exponential phase function, the sampling effort is corresponding to the smallest period of the wrapped function. Here, the periods are inversely proportional to the slope of the unwrapped phase function, i.e., to the local gradient of  $\gamma_\ell(\boldsymbol{\rho})$ . Because of that, it is very typical that an easily sampled smooth wavefront becomes much more difficult sampled in the form of  $2\pi$ -modulo.

The most straightforward method to overcome such sampling overkill is to eschew the sampling of wrapped phase terms but handle them analytically. Mathematically, there are lots of analytical polynomials that can be used to represent the smooth phase function. Meanwhile, with the suitable fitting technique, the majority of the smooth phase can be extracted from the numerical sampled data and stored analytically. However, to employ them into the Fourier transform, some available property is exceptionally significant. For instance, The well-known shift theorem benefits from the properties of the linear phase and

the convolution, where the Fourier transform of a linear phase turns out to a Dirac delta function, and the effect of convolving a function with the Dirac delta function is to shift the function by the same amount. Unfortunately, it is not easy to generalize the shift theorem to other higher-order phase terms. First of all, for other phase terms, it is not easy to find the analytical expression of their Fourier transform.

Furthermore, even though we obtain their Fourier transforms, the deduction of the convolution might be unsolvable. Therefore, in the following, we concentrate precisely on the way to tackle the Fourier transform that eschews the sampling of quadratic phase terms. The corresponding trick is that the Fourier transform of a quadratic phase turns out also to be quadratic. L. Mandel and E. Wolf have demonstrated the application of the trick to different diffraction integrals. Most of the discussion is still limited to the one-dimensional ( $x^2$ ) or separable problems ( $x^2, y^2$ ). The cross term  $xy$ , which constitutes a prominent part of diffraction theory, is not involved [76, 77].

On the other hand, in most optical scenes, the scaling factors of the quadratic phase terms are determined by the Taylor expansion. In the paraxial approximation, the spectral bandwidth of the electromagnetic field is so small that the local approximation method can provide accurate results. But, in the face of non-paraxial configuration, the performance and accuracy of this approach may suffer limitations.

The fast calculation of the field distribution in the focal region of a non-paraxial imaging system is a vital topic in physical optical modeling [78, 79]. Various publications based on the Chirp Z-transform (CZT) have been proposed in the last decades. The foundation of CZT is as same as the semi-analytical Fourier transform, which is the convenient property whereby we extract the quadratic phase term in the Fourier transform. It should be noted that the consideration of two dimensions and the cross-talk term in the CZT has been done in [80]. And, the end result bears a definite resemblance to the conclusions we present below. However, the derivation of the CZT is centered on the Fourier-transform kernel of the already-discretized operation, while the method we put forth focuses, instead, on the field term.

Let us start from a new representation of the field

$$V_\ell(\boldsymbol{\rho}) = U_\ell(\boldsymbol{\rho}) \exp[i\psi_q(\boldsymbol{\rho})] , \quad (2)$$

with

$$|V_\ell(\boldsymbol{\rho})| = |U_\ell(\boldsymbol{\rho})| , \quad (3)$$

$$\arg[U_\ell(\boldsymbol{\rho})] = \gamma_\ell(\boldsymbol{\rho}) - \psi_q(\boldsymbol{\rho}) , \quad (4)$$

$$\psi_q(\boldsymbol{\rho}) = D_x x^2 + Cxy + D_y y^2 . \quad (5)$$

In Eq. (2) the quadratic phase terms are extracted with real-valued coefficients  $C$ ,  $D_x$  and  $D_y$ . Then, the amplitude and the remains of the phase are combined together and denoted by  $U_\ell(\boldsymbol{\rho})$ . In practice, we still must sample  $U_\ell(\boldsymbol{\rho})$ . Compared to the full phase function  $\arg[V_\ell(\boldsymbol{\rho})] = \gamma_\ell(\boldsymbol{\rho})$ ,  $\arg[U_\ell(\boldsymbol{\rho})]$  has a much less pronounced local gradient so that the sampling effort is reduced dramatically. However, this approach only works when the demanded FFT can be performed without the sampling of  $\exp[i\psi_q(\boldsymbol{\rho})]$ . It means that we must handle this information analytically in the entire process.

After that, we try to derive the Fourier transform of  $V_\ell(\boldsymbol{\rho})$  without sampling the quadratic phase term defined in Eq. (5).

Plugging Eq. (2) into the Fourier transform equation, we obtain

$$\begin{aligned} \tilde{V}_\ell(\boldsymbol{\kappa}) &= \mathcal{F}_\kappa[V_\ell(\boldsymbol{\rho})] = \frac{1}{2\pi} \iint_{-\infty}^{\infty} V_\ell(\boldsymbol{\rho}) \exp(-i\boldsymbol{\kappa} \cdot \boldsymbol{\rho}) d^2\rho \\ &= \mathcal{F}_\kappa \{ U_\ell(\boldsymbol{\rho}) \exp[i\psi_q(\boldsymbol{\rho})] \} , \end{aligned} \quad (6)$$

where  $\boldsymbol{\kappa} = (k_x, k_y)$  is the projection of the spatial frequency vector onto the plane transversal to  $z$ .

From the convolution theorem, we know that

$$\tilde{V}_\ell(\boldsymbol{\kappa}) = \frac{1}{2\pi} \mathcal{F}_\kappa[U_\ell(\boldsymbol{\rho})] * \mathcal{F}_\kappa \{ \exp[i\psi_q(\boldsymbol{\rho})] \} , \quad (7)$$

where the symbol “\*” indicates convolution.

In principle, the term  $\mathcal{F}_\kappa[U_\ell(\boldsymbol{\rho})]$  must be treated numerically. On the other hand, we find that the Fourier transform of the polynomial of second order  $\mathcal{F}_\kappa \{ \exp[i\psi_q(\boldsymbol{\rho})] \}$  can be solved with the integral formula

$$\int_{-\infty}^{\infty} \exp(-ax^2 + bx + c) dx = \sqrt{\frac{\pi}{a}} \exp\left(\frac{b^2}{4a} + c\right) , \quad (8)$$



which is valid for any  $a, b, c \in \mathbb{C}$ , provided that  $\Re\{a\} \geq 0$  and  $a \neq 0$ .

With the help of Eq. (8) [81], we deduce the Fourier transform of the polynomial of second order

$$\mathcal{F}_\kappa \{ \exp[i\psi_q(\rho)] \} = \alpha \exp[i\tilde{\psi}_q(\kappa)] \quad (9)$$

with

$$\tilde{\psi}_q(\kappa) = \tilde{D}_x k_x^2 + \tilde{C} k_x k_y + \tilde{D}_y k_y^2, \quad (10)$$

and with constant factors  $\alpha, \tilde{C}, \tilde{D}_x$  and  $\tilde{D}_y$

$$\alpha = \begin{cases} \sqrt{\frac{i}{\tilde{D}_x}} \sqrt{\frac{D_x}{i(C^2 - 4D_x D_y)}} , & D_x \neq 0 \\ \sqrt{\frac{i}{\tilde{D}_y}} \sqrt{\frac{D_y}{i(C^2 - 4D_x D_y)}} , & D_x = 0 \text{ and } D_y \neq 0 \\ \sqrt{\frac{1}{C^2 - 4D_x D_y}} , & D_x = 0 \text{ and } D_y = 0 \end{cases} . \quad (11)$$

and

$$\begin{aligned} \tilde{C} &= -\frac{C}{C^2 - 4D_x D_y} \\ \tilde{D}_x &= \frac{D_y}{C^2 - 4D_x D_y} \\ \tilde{D}_y &= \frac{D_x}{C^2 - 4D_x D_y} . \end{aligned} \quad (12)$$

It should be remarked that when  $C^2 - 4D_x D_y = 0$ , the two-dimensional phase function  $\psi_q(\rho)$  degenerates into a rotated one-dimensional function. For such special cases, we need to do the coordinate transformation and then treat them similarly in one dimension. More details of the special cases will be discussed in the next sections.

Substituting for  $\mathcal{F}_\kappa \{ \exp[i\psi_q(\rho)] \}$  in Eq. (7) and expanding the convolution, we get

$$\begin{aligned} \tilde{V}_\ell(\kappa) &= \frac{1}{2\pi} \iint_{-\infty}^{\infty} \mathcal{F}_{\kappa'} [U_\ell(\rho)] \alpha \exp[i\tilde{\psi}_q(\kappa - \kappa')] d^2 \kappa' \\ &= \alpha \exp[i\tilde{\psi}_q(\kappa)] \frac{1}{2\pi} \iint_{-\infty}^{\infty} \mathcal{F}_{\kappa'} [U_\ell(\rho)] \exp[i\tilde{\psi}_q(\kappa')] \\ &\quad \times \exp\left(-i\tilde{C}k_x k'_y - i\tilde{C}k_y k'_x - i2\tilde{D}_x k_x k'_x - i2\tilde{D}_y k_y k'_y\right) d^2 \kappa' . \end{aligned} \quad (13)$$

And by defining the **coordinate transform vector**  $\beta = (\beta_x, \beta_y)$

$$\begin{aligned}\beta_x &= -2\tilde{D}_x k_x - \tilde{C} k_y \\ \beta_y &= -\tilde{C} k_x - 2\tilde{D}_y k_y,\end{aligned}\tag{14}$$

the integral in Eq. (13) can be written as

$$\begin{aligned}\tilde{V}_\ell(\kappa) &= \alpha \exp[i\tilde{\psi}_q(\kappa)] \frac{1}{2\pi} \int_{-\infty}^{\infty} \mathcal{F}_{\kappa'} [U_\ell(\rho)] \exp[i\tilde{\psi}_q(\kappa')] \exp(i\beta_x k'_x + i\beta_y k'_y) d^2 \kappa' \\ &= \alpha \exp[i\tilde{\psi}_q(\kappa)] \mathcal{F}_\beta^{-1} \{ \mathcal{F}_{\kappa'} [U_\ell(\rho)] \exp[i\tilde{\psi}_q(\kappa')] \} \\ &= \alpha \exp[i\tilde{\psi}_q(\kappa)] \mathcal{F}_\beta^{-1} \{ \tilde{U}_\ell(\kappa) \exp[i\tilde{\psi}_q(\kappa)] \}.\end{aligned}\tag{15}$$

The interpretation of Eq. (15) as the product of a Fourier transform and a polynomial of the second order

$$\begin{aligned}\tilde{V}_\ell(\kappa) &= \mathcal{F}_\kappa^{\text{semi}} [V_\ell(\rho)] \\ &= \tilde{A}_\ell(\kappa) \exp[i\tilde{\psi}_q(\kappa)]\end{aligned}\tag{16}$$

with

$$\tilde{A}_\ell(\kappa) = \alpha \mathcal{F}_\beta^{-1} \{ \tilde{U}_\ell(\kappa) \exp[i\tilde{\psi}_q(\kappa)] \}\tag{17}$$

has the same form as the field representation in the spatial domain, that is, a **numerical spectrum and an analytical quadratic phase term**. In a numerical implementation of the method here proposed, all the above-presented formulas can be written in the **discrete, finite-dimensional version**, e.g.  $V_\ell(x_m, y_n) = U_\ell(x_m, y_n) \exp(i\psi_q(x_m, y_n))$ ,  $x_m \in \left(-\frac{\Delta X}{2}, \frac{\Delta X}{2}\right)$  and  $y_n \in \left(-\frac{\Delta Y}{2}, \frac{\Delta Y}{2}\right)$ . According to sampling theory, the sampling number is determined by the extension of  $V_\ell(x_m, y_n)$  and  $\tilde{V}_\ell(k_{xm}, k_{yn})$  in both domains, i.e.  $N_x = \Delta X / \frac{2\pi}{\Delta K_x}$  and  $N_y = \Delta Y / \frac{2\pi}{\Delta K_y}$ . These numbers refer to the full field  $V_\ell(x_m, y_n)$ . Then, considering our chosen field representation, in the case of a strong quadratic phase  $\psi_q(x_m, y_n)$ , at the boundary of the effective range there would be a **very high local gradient**  $\nabla_\perp \psi_q(x_m, y_n)$ , which will result in a **large extension in the other domain**: this is the reason behind the high sampling effort of the full field. On the other hand, **the sampling required for the residual field remains relatively small**. It is important to note that, in the **semi-analytical Fourier transform**, the quadratic

phase is always handled analytically. When the semi-analytical Fourier transform is being performed, the first FFT is numerically used on  $U_\ell(x_m, y_n)$ , with a much lower sampling number than that required for the full field. The second, inverse, FFT is not only applied to the residual spectrum, but also to an additional phase term. In Eqns. (10)-(11) we see that the quadratic phase factors in the spatial-frequency domain  $\tilde{D}_x$ ,  $\tilde{D}_y$  and  $\tilde{C}$  are inversely proportional to the quadratic factors in the spatial domain. Therefore, when the field possesses a strong quadratic phase in the spatial domain, the corresponding quadratic phase in the spatial-frequency domain will be very weak, which means we can neglect its influence on the sampling of  $\tilde{U}_\ell(\kappa) \exp[i\tilde{\psi}_q(\kappa)]$ . Therefore, even though an additional FFT is used, the numerical effort of performing two FFT is still smaller than that required for the FFT of the fully sampled, complete field.

### 2.1.2 Inverse semi-analytical Fourier transform

Analogously to the regular Fourier transform, the semi-analytical FT has its reverse operation, namely the inverse semi-analytical Fourier transform.

The spectrum in the spatial-frequency domain is written as

$$\begin{aligned}\tilde{V}_\ell(\kappa) &= |\tilde{V}_\ell(\kappa)| \exp[i\tilde{\gamma}_\ell(\kappa)] \\ &= \tilde{A}_\ell(\kappa) \exp[i\tilde{\psi}_q(\kappa)]\end{aligned}\tag{18}$$

with

$$\arg[\tilde{A}_\ell(\kappa)] = \tilde{\gamma}_\ell(\kappa) - \tilde{\psi}_q(\kappa)\tag{19}$$

where  $\tilde{\psi}_q(\kappa)$  is the polynomial of second order in the  $\kappa$ -domain which has been previously described in Eq. (10).

Using the same trick as Sec. 2.1.1, we can deduce the analytical representation of the inverse semi-analytical FT

$$\begin{aligned}V_\ell(\rho) &= \mathcal{F}_\kappa^{-1, \text{semi}} [\tilde{V}_\ell(\kappa)] \\ &= U_\ell(\rho) \exp[i\psi_q(\rho)]\end{aligned}\tag{20}$$

with

$$U_\ell(\rho) = \tilde{\alpha} \mathcal{F}_{\tilde{\beta}} \left\{ \mathcal{F}_\kappa^{-1} [\tilde{A}_\ell(\kappa)] \exp[i\psi_q(\rho)] \right\}\tag{21}$$

and the constant factor  $\tilde{\alpha}$

$$\tilde{\alpha} = \begin{cases} \sqrt{\frac{i}{\tilde{D}_x}} \sqrt{\frac{\tilde{D}_x}{i(\tilde{C}^2 - 4\tilde{D}_x\tilde{D}_y)}} & , \quad \tilde{D}_x \neq 0 \\ \sqrt{\frac{i}{\tilde{D}_y}} \sqrt{\frac{\tilde{D}_y}{i(\tilde{C}^2 - 4\tilde{D}_x\tilde{D}_y)}} & , \quad \tilde{D}_x = 0 \text{ and } \tilde{D}_y \neq 0 \\ \sqrt{\frac{1}{\tilde{C}^2 - 4\tilde{D}_x\tilde{D}_y}} & , \quad \tilde{D}_x = 0 \text{ and } \tilde{D}_y = 0 \end{cases} \quad (22)$$

and,

$$\begin{aligned} C &= -\frac{\tilde{C}}{\tilde{C}^2 - 4\tilde{D}_x\tilde{D}_y} \\ D_x &= \frac{\tilde{D}_y}{\tilde{C}^2 - 4\tilde{D}_x\tilde{D}_y} \\ D_y &= \frac{\tilde{D}_x}{\tilde{C}^2 - 4\tilde{D}_x\tilde{D}_y} . \end{aligned} \quad (23)$$

and with the coordinate transform vector  $\tilde{\beta} = (\tilde{\beta}_{k_x}, \tilde{\beta}_{k_y})$

$$\begin{aligned} \tilde{\beta}_{k_x} &= 2D_x x + Cy , \\ \tilde{\beta}_{k_y} &= Cx + 2D_y y . \end{aligned} \quad (24)$$

Up to this point, we have obtained the representation of the inverse semi-analytical FT. Similar to the forward operation, the polynomial of the second order  $\tilde{\psi}_q(\kappa)$  in  $\kappa$ -domain is fully analytically handled in the entire process. The sampling effort depends on the two FFTs of the spectrum with less sampling, the  $\tilde{A}_\ell(\kappa)$  in Eq. (21).

### 2.1.3 Hybrid semi-analytical Fourier transform and its inverse operation

Without the loss of generality, in the practical modeling, we might need to work with the electromagnetic field whose quadratic phase is very intense only on one dimension. The most typical examples are the cylindrical wave and the astigmatism Gaussian beam. In this kind of situation, the resulting quadratic phase factor (determinant of the Hessian matrix) becomes zero or relatively small, i.e.,  $C^2 - 4D_x D_y \approx 0$ . Consequently, all the above-concluded formulas cannot be used. Meanwhile, because of the sampling effort of this one-dimensional quadratic phase, the regular FFT faces a huge numerical issue. Therefore, we would like to develop a new technique to overcome it. In what follows, we will extend the semi-analytical Fourier transform algorithm to the singularity cases.

First of all, from the mathematical point of view, the possibilities of singularity cases and their physical meaning are demonstrated. According to the numerical criterion, we can classify the possible situation into three groups:

- $C^2 - 4D_x D_y = 0$  ( $D_x \neq 0, D_y = 0, C = 0$ ): the quadratic phase only is on the X-axis.
- $C^2 - 4D_x D_y = 0$  ( $D_x = 0, D_y \neq 0, C = 0$ ): the quadratic phase only is on the Y-axis.
- $C^2 - 4D_x D_y = 0$  ( $D_x \neq 0, D_y \neq 0, C \neq 0$ ): the quadratic phase only is on a tilted direction.

In principle, since the physical model behind them are the same, we can use the same strategy to deal with all these three singularity cases. The only difference between them is the working coordinate system. By rotating the coordinate system, we can always transform the latter two cases into the first kind of situation. Therefore, in the following part, we will concentrate on the theoretical derivation for the first case. The related formulas for the other two cases are given in the Appendix.

Let us consider the one-dimensional quadratic phase on the X-axis and rewrite the Eq. (2) and Eq. (5) to

$$V_\ell(\boldsymbol{\rho}) = U_\ell(\boldsymbol{\rho}) \exp[i\psi_q(x)] , \quad (25)$$

with

$$\psi_q(x) = D_x x^2. \quad (26)$$

Like that for the standard semi-analytical Fourier transform, with the help of the property of the quadratic phase and the convolution trick, we can carry out a similar derivation process and obtain the analytical expression of the hybrid semi-analytical Fourier transform.

$$\tilde{V}_\ell(\boldsymbol{\kappa}) = \alpha \exp[i\tilde{\psi}_q(k_x)] \mathcal{F}_{\beta_x}^{-1, x} \{ \tilde{U}_\ell(\boldsymbol{\kappa}) \exp[i\tilde{\psi}_q(k_x)] \} \quad (27)$$

with

$$\tilde{\psi}_q(k_x) = -\frac{1}{4D_x} k_x^2 = \tilde{D}_x k_x^2 \quad (28)$$

and

$$\alpha = \sqrt{\frac{i}{2D_x}}. \quad (29)$$

Here, the quadratic phase function is independent of the variable  $y$ . And, the operator  $\mathcal{F}_{\beta_x}^{-1,x}$  denotes the one-dimensional Fourier transform operation and the one-dimensional coordinate transform operation on the x-axis. The coordinate transform factor  $\beta_x$  is defined as

$$\beta_x = \frac{k_x}{2D_x}. \quad (30)$$

It is relevant to highlight that the one-dimensional Fourier transform must be done row by row on the sampled data set. For instance, there is an equidistant sampled field with sampling points  $(N_x, N_y)$ . Assuming a strong quadratic phase on the x-dimension, in the case that Hybrid semi-analytical Fourier transform is allowed, we must execute 1D FFT per row, in total  $N_y$  times.

#### *Inverse hybrid semi-analytical Fourier transform*

In an analogous manner, we can perform the derivation of the inverse hybrid semi-analytical Fourier transform. Let us start from the spectrum of the field with one-dimensional quadratic phase on x-axis

$$\tilde{V}_\ell(\boldsymbol{\kappa}) = \tilde{A}_\ell(\boldsymbol{\kappa}) \exp[i\tilde{\psi}_q(k_x)], \quad (31)$$

where  $\tilde{\psi}_q(k_x)$  is the quadratic phase in k-domain whose definition is given in Eq. (28).

Again, carrying out a similar process, the field representation in the spatial domain is derived out.

$$V_\ell(\boldsymbol{\rho}) = \tilde{\alpha} \exp[i\psi_q(x)] \mathcal{F}_{\tilde{\beta}_x}^x \{ \tilde{A}_\ell(\boldsymbol{\rho}) \exp[i\psi_q(x)] \} \quad (32)$$

with

$$\tilde{\alpha} = \sqrt{\frac{i}{2\tilde{D}_x}} \quad (33)$$

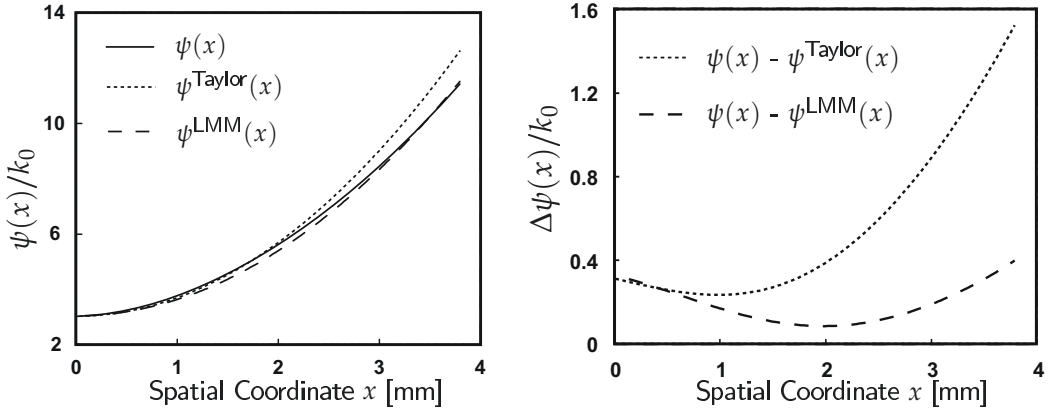
and with

$$\tilde{\beta}_x = -\frac{x}{2\tilde{D}_x}. \quad (34)$$

As same as the standard semi-analytical Fourier transform, the initial field  $V_\ell(\rho)$  is retrieved. The fact reveals the consistency of the hybrid semi-analytical Fourier transform and its inverse operation.

#### 2.1.4 Handling of the quadratic phase

As we have emphasized in the previous sections, by using the semi-analytical Fourier transform, we would like to **improve the computational efficiency of the Fourier transform operation**. The sampling effort of the semi-analytical Fourier transform has been well discussed at the end of section 2.1.1. In short, it is entirely dependent on the sampling of the residual **field  $U_\ell(\rho)$**  or the residual **spectrum  $\tilde{A}_\ell(\kappa)$** . In practice, the initial field is usually given in the form of the



(a) Quadratic phase fitting of  $\psi(\rho)$  (b) Fitting deviation of two methods

Figure 2: Extraction of the quadratic phase  $\psi_q(\rho)$  from a general phase function  $\psi(\rho)$  by using the Taylor expansion approach and the Levenberg-Marquardt fitting method. (a) Applying both methods to an aberrated phase function (spherical phase with coma and astigmatism aberration) in the spatial domain. (b) Comparison of the performance of the Taylor expansion method and Levenberg-Marquardt fitting method. Taylor expansion approach only works well locally around the central area. Both the function value and the gradient of the residual phase are higher with the Taylor expansion than with the LMM.

hybrid sampling strategy, i.e., equidistant sampled residual field/spectrum and non-equidistant sampled smooth phase component. Since the semi-analytical

Fourier transform can handle only the quadratic phase, we must try to extract the corresponding second-order phase terms as much as possible from the original smooth phase. One reasonable way that works is to minimize the gradient of the smooth phase  $\psi(\boldsymbol{\rho})$  or  $\tilde{\psi}(\boldsymbol{\kappa})$  over the given function support. To achieve this goal, we have to find an effective method of determining the optimal factors of the quadratic phase  $\psi_q(\boldsymbol{\rho})$  or  $\tilde{\psi}_q(\boldsymbol{\kappa})$ .

There are two alternatives, analytical or numerical. The most widely recognized analytical approach is the Taylor expansion. For a given smooth phase function  $\psi(\boldsymbol{\rho})$ , by using Taylor expansion up to the second order, we can obtain  $\psi_q(\boldsymbol{\rho})$  analytically

$$\begin{aligned}\psi(\boldsymbol{\rho}) &= (x - x_0)^2 \psi_{xx}(\boldsymbol{\rho}_0) + (x - x_0)(y - y_0) \psi_{xy}(\boldsymbol{\rho}_0) + (y - y_0)^2 \psi_{yy}(\boldsymbol{\rho}_0) + h(\boldsymbol{\rho}) \\ &= \psi_{xx}(\boldsymbol{\rho}_0) x^2 + \psi_{xy}(\boldsymbol{\rho}_0) xy + \psi_{yy}(\boldsymbol{\rho}_0) y^2 + \Delta\psi(\boldsymbol{\rho}) \\ &= \psi_q^T(\boldsymbol{\rho}) + \Delta\psi(\boldsymbol{\rho})\end{aligned}\tag{35}$$

where  $\psi_{xx}$ ,  $\psi_{xy}$  and  $\psi_{yy}$  are the entries of Hessian of the phase function  $\psi(\boldsymbol{\rho})$  at the reference point  $\boldsymbol{\rho}_0 = (x_0, y_0)$ . The  $h(\boldsymbol{\rho})$  presents the constant, linear and higher order Taylor polynomials.

Even though the analytical Taylor formula can directly provide us the desired quadratic phase factors without any numerical operations, two practical validity conditions constrain its usage and the performance in the real scenes. The first reason is because of the demand for an analytical phase function  $\psi(\boldsymbol{\rho})$ . The second point is the fact that the formula has only local validity. According to Eq. (35), we can say in a neighborhood that around the reference point, the gradient of  $\psi(\boldsymbol{\rho})$  would be quite small. However, in a range farther away from the reference point, we cannot conclude this. Besides the Taylor expansion, there are also various analytical approaches, e.g., the Avoort fit [82]. While these analytical approaches are applicable to some specific cases and have good performance, all of them have more or less some limitations.

It is for these reasons that we decide to use numerical approaches for more general situations. As an example, we can choose Gaussian Newton method and Levenberg-Marquardt method which are devoted to solving minimization



problems and is especially suitable for the least squares curve fitting. The fitting model of quadratic terms can be written as

$$\begin{aligned}\psi(\boldsymbol{\rho}) &= D_x x^2 + Cxy + D_y y^2 + \Delta\psi(\boldsymbol{\rho}) \\ &= \psi_q^L(\boldsymbol{\rho}) + \Delta\psi(\boldsymbol{\rho}).\end{aligned}\tag{36}$$

Here,  $\Delta\psi$  is the deviation between the value of the actual function and that of the fitting result. Typically, a numerical fitting is an iterative process and the merit function is set to the imperfect function value  $\Delta\psi$ . However, in this task our goal is to minimize the sampling, which is only related to the gradient of the residual phase. Therefore, we select  $\nabla_{\perp}(\Delta\psi(\boldsymbol{\rho}))$  as the merit function instead.

In order to compare the difference between the numerical and analytical approaches, we prepare an example to demonstrate their performance. Some analytical coma and astigmatism aberration are added on an analytically known spherical phase, and the solid line is shown in Fig. 2(a). Both the Taylor expansion and the Levenberg-Marquardt method are applied for the quadratic phase fitting. The comparison of the deviation of the Taylor expansion method and the LMM is shown in Fig. 2(b). We can see that the Taylor expansion method only works well locally around the central zone, which is the reference point of the expansion. In the range far from the central area, both the deviation of the function value and the gradient of the deviation at the edge are much larger than for the other approach. The facts prove that the numerical method provides better results than the analytical Taylor expansion method. Therefore, we recommend using numerical methods in practical tasks.

#### 2.1.5 Validity condition and the numerical criterion

Up to now, we have presented the theoretical derivation and the physical interpretation of the semi-analytical Fourier transform. As we mentioned, only for the input field with a strong quadratic phase, the proposed approach will show its advantages that can tackle the Fourier transform operation efficiently. Therefore, to carry out a robust and user-friendly algorithm in practice, a reasonable criterion to judge the validity of the SFT is necessary. As a competition of the proposed technique, the regular FFT is regarded as our reference. We will esti-

mate the required sampling points for both approaches and return the method whose required sampling points are less.

As an example, let us analyze the forward Fourier transform. In general, the equidistance sampled residual field/spectrum, and the quadratic phase factors are given as the input of the Fourier transform operator. We assume sampling parameters of the residual field: sampling points  $[N_x(U), N_y(U)]$  and sampling distance  $[\delta x(U), \delta y(U)]$ . We have concluded in section 2.1.1 that the numerical effort of semi-analytical Fourier transform depends only on the residual field. Then, we need to know the sampling effort of the regular FFT in the case that the quadratic phase dominates the sampling. In the following, we will analyze the contribution of different quadratic phase term individually.

*$D_x x^2$  term*

For the quadratic phase term  $D_x x^2$ , we can compute out its maximum frequency

$$k_x^{\max} = \frac{d}{dx} D_x x^2|_{x=x_{\max}} = D_x N_x(U) \delta x(U) \quad (37)$$

where the  $x_{\max} = \frac{1}{2} N_x(U) \times \delta x(U)$  is the half of the field size in x-dimension.

Based on this maximum frequency, we can estimate the sampling distance of the complete field  $V_\ell(\rho)$  in x-dimension by

$$\delta x(V) = \frac{2\pi}{2k_x^{\max}}. \quad (38)$$

So, the sampling points of the complete field  $V_\ell(\rho)$  in x-dimension is

$$N_x(V) = \frac{2x_{\max}}{\delta x(V)} = \frac{D_x [N_x(U) \delta x(U)]^2}{\pi}. \quad (39)$$

Finally, we define a factor to depict the difference of the sampling numbers between two approaches

$$\eta_{D_x} = \frac{N_x(V)}{N_x(U)} = \frac{D_x [\delta x(U)]^2 N_x(U)}{\pi}. \quad (40)$$

*$D_y y^2$  term*

Using the same method, we obtain the factor in y-dimension

$$\eta_{D_y} = \frac{N_y(V)}{N_y(U)} = \frac{D_y [\delta y(U)]^2 N_y(U)}{\pi}. \quad (41)$$

### *C<sub>xy</sub> term*

For the crosstalk term, we need to analyze the factor in both x- and y-dimension.

$$\begin{cases} \eta_{C_x} &= \frac{C\delta x(U)\delta y(U)N_y(U)}{2\pi} \\ \eta_{C_y} &= \frac{C\delta x(U)\delta x(U)N_y(U)}{2\pi} \end{cases} \quad (42)$$

For any input field, we can calculate the above four factors. If the corresponding factor is larger than 1, it means that the quadratic phase factor is strong enough that it dominates the sampling of the field in this dimension. And then, we can say it is possible to apply the semi-analytical Fourier transform. In the end, we conclude the following workflow in the implementation.

1. Examine the quadratic phase factor
  - if  $\eta_{D_x} > 1$ , keep  $D_x$  the same. Otherwise,  $D_x = 0$
  - if  $\eta_{D_y} > 1$ , keep  $D_y$  the same. Otherwise,  $D_y = 0$
  - if  $\eta_{C_x} > 1$  or  $\eta_{C_y} > 1$ , keep  $C$  the same. Otherwise,  $C = 0$
2. Make decision (the threshold value can be set by the user)
  - if  $\text{Max}(\eta_{D_x}, \eta_{D_y}, \eta_{C_x}, \eta_{C_y}) > \text{threshold}$ , use semi-analytical Fourier transform
  - if  $\text{Max}(\eta_{D_x}, \eta_{D_y}, \eta_{C_x}, \eta_{C_y}) < \text{threshold}$ , use regular fast Fourier transform

## 2.2 NUMERICAL EXAMPLES

So far in this chapter, we have concentrated on the theoretical derivation of the semi-analytical Fourier transform algorithm. And, we have implemented this new technique in the physical optics modeling and design software VirtualLab Fusion. In the coming section, therefore, we will apply this new approach to different numerical experiments to compare its performance with that of the regular FFT. All simulations were done with the optics software VirtualLab Fusion.

### 2.2.1 Fourier transform of a field with a purely quadratic phase

As our starting point, we would like to investigate the Fourier transform of an essential type of light field, i.e., the Gaussian beam [83, 84]. Specifically, we select the Laguerre Gaussian 01-mode. In the numerical simulation, we employ a linearly  $E_x$  polarized Gaussian field, with the Rayleigh length  $z_R =$  of 29.53 mm and a wavelength of 532 nm as the input. Its half-divergence angle is about

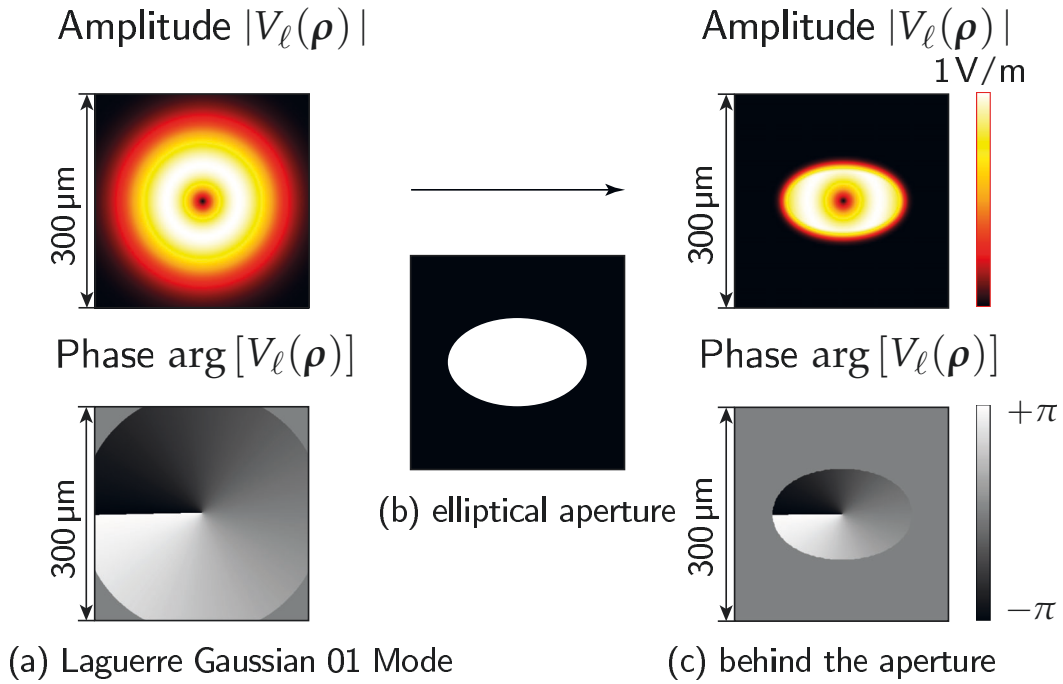


Figure 3: Truncated Laguerre Gaussian 01-mode at the waist plane. Panel (a) shows the amplitude and phase distribution of the  $E_x$ -component of the initial Laguerre Gaussian 01-mode. Panel (b) presents an elliptical aperture whose size is  $(150\ \mu\text{m} \times 80\ \mu\text{m})$  and with 10% soft edge. Panel (c) shows the amplitude and phase distribution of the Laguerre Gaussian field behind the aperture.

$0.194^\circ$ , and its beam waist radius is  $100\ \mu\text{m}$ . The amplitude distribution of the  $E_x$  component and the corresponding phase distribution are shown in Fig. 3(a). Then, an elliptical aperture, whose size is  $(150\ \mu\text{m} \times 80\ \mu\text{m})$  and with 10% soft edge, is used to truncate the given Laguerre Gaussian mode. The light field behind the aperture is presented in Fig. 3(b).

Considering the physical property of the semi-analytical Fourier transform, in the first example, we would like to investigate the influence of the purely quadratic phase. Here, we select a lower-order, symmetric aberration phase, namely defocus aberration, which can be described by the Zernike polynomials [85–87]. Its mathematical expression can be written as  $\psi_q(\rho) = \sqrt{3}kc_2^0 \left(2\frac{\rho^2}{\rho_{\max}^2} - 1\right)$ , where  $k = \frac{2\pi}{\lambda}\tilde{n}$ ,  $\lambda$  being the wavelength,  $\rho_{\max} = 200 \mu\text{m}$  indicates the normalized radius of the Zernike polynomials. In this set of experiments, we configure the

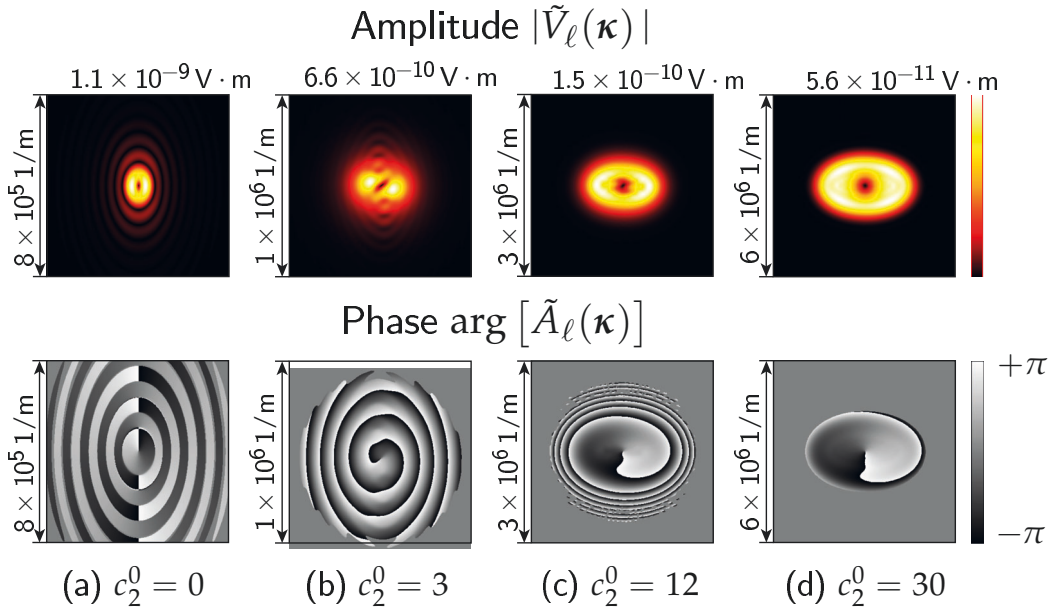


Figure 4: Semi-analytical Fourier transform of the truncated Laguerre Gaussian mode with different values of the quadratic phase coefficient. Panel (a)-(d) show the result of said Fourier transform operation (amplitude and residual phase distribution of  $E_x$  component). Since the quadratic phase is individual analytically handled in the SFT, we don't resample and present it in this picture. The required numbers of sampling points of SFT and FFT for each case are respectively given in Tab. 1.

input field by superposing different quadratic phase  $\psi_q(\rho)$  onto the truncated Laguerre Gaussian mode  $U_\ell(\rho)$ . In detail, we choose four typical quadratic phase coefficients and respectively perform the SFT. The resulting spectrum pattern are shown in Fig. 4. We can see that for all four cases the remaining phase term  $\arg[\tilde{A}_\ell(\kappa)]$  is not strong. Especially in case (d), the residual phase is only the vertex phase, which is caused by the higher-order Gaussian.

Table 1: Comparison of the required sampling points for the Fourier transform of a truncated Laguerre Gaussian 01-mode: SFT vs. FFT. Corresponding field distribution and Fourier transform result are respectively presented in Fig. 3 and Fig. 4 .

No.	$\psi_q(\rho)$ coefficients	FFT sampling points	SFT sampling points
Fig. 4 (a)	$c_2^0 = 0$	$(111 \times 119)$	$(111 \times 119)$
Fig. 4 (b)	$c_2^0 = 3$	$(225 \times 235)$	$(111 \times 119)$
Fig. 4 (c)	$c_2^0 = 12$	$(329 \times 235)$	$(111 \times 119)$
Fig. 4 (d)	$c_2^0 = 30$	$(659 \times 353)$	$(111 \times 119)$

To investigate the numerical performance comprehensively, we also perform FFT on the same fields and list the required Nyquist sampling points of both the regular FFT and the SFT in Table 1. By comparison, we can find that as the quadratic coefficients increases, the sampling number of FFT overgrows. But, the sampling number of SFT keeps a constant. It is because that in FFT, the quadratic phase must be fully sampled in  $2\pi$ -modulo. It would lead to an enormous sampling effort for a sizeable quadratic coefficient. On the other hand, in SFT, the quadratic phase is handled analytically so that the sampling number is just dependent on the residual field  $U_\ell(\rho)$ .

### 2.2.2 Fourier transform of a field with a spherical phase

In the practical simulation, it is not very common that the light field presents only the quadratic phase. In contrast, the spherical phase is a more substantial model for physical optical modeling. Thus, in the second example, we would like to concentrate on the Fourier transform of a field with a spherical phase. First of all, we build up a simple optical setup to generate the working field: a  $E_x$  polarized ideal plane wave is truncated by a circular mask whose size is  $(2\text{ mm} \times 2\text{ mm})$  and with 10% soft edge. Its wavelength is at 532 nm. Behind the mask, a divergent spherical phase is superimposed onto the light field. The spherical phase is expressed as  $\psi^{\text{sph}}(\rho) = \text{sgn}(R) k_0 \tilde{n} \sqrt{\rho^2 + R^2}$ , where factor  $R > 0$  denotes the radius of the curvature of the spherical phase.

Table 2: Comparison of the required sampling points for the Fourier transform of a truncated spherical wave: SFT vs. FFT. Corresponding field distribution and semi-analytical Fourier transform result are respectively presented in Fig. 5 and Fig. 6.

No.	spherical radius $R$	FFT sampling points	SFT sampling points
Fig. 5 (b)	$R = +\infty$	$(79 \times 79)$	$(79 \times 79)$
Fig. 5 (c)	$R = 50 \text{ mm}$	$(873 \times 873)$	$(173 \times 173)$
Fig. 6 (d)	$R = 10 \text{ mm}$	$(3743 \times 3743)$	$(233 \times 233)$
Fig. 6 (e)	$R = 3 \text{ mm}$	$(11031 \times 11031)$	$(289 \times 289)$
Fig. 6 (f)	$R = 2 \text{ mm}$	$(13521 \times 13521)$	$(501 \times 501)$

The amplitude and phase distribution of the residual field  $U_\ell(\boldsymbol{\rho})$  in the spatial domain are shown in Fig. 5(a). We can see that the residual phase is zero in the definition domain, i.e.,  $\arg[U_\ell(\boldsymbol{\rho})] = 0$ . It means that all phase information comes from the customized spherical phase. The complete field can be expressed as  $V_\ell(\boldsymbol{\rho}) = U_\ell(\boldsymbol{\rho}) \exp[i\psi^{\text{sph}}(\boldsymbol{\rho})]$ . In the numerical simulation, by adjusting the weight factor of the spherical phase, namely the spherical radius  $R$ , we obtained the desired working fields. By applying the Taylor expansion to the spherical phase function, the quadratic phase coefficients can be calculated analytically. Afterward, we can perform the semi-analytical Fourier transform and compare the resulting spectrum in the k-domain. Simulation results, for the spherical radius in the range of  $R \in (2 \text{ mm}, +\infty)$ , are presented in Fig. 5 and Fig. 6.

In this set of experiments, we fix the size of the input field but allow configuring the magnitude of the spherical phase factor  $R$ . More specifically, the smaller factor  $R$ , the larger numerical aperture(NA), and the more intense spherical phase. The result of the experiment showed, in the case of a large-valued spherical radius factor (corresponding to a very weak spherical phase), the residual phase  $\arg[\tilde{A}_\ell(\boldsymbol{\kappa})]$  in the k-domain is also very simple, e.g., Fig. 5 (b) and (c). It is because, for the low NA cases, the difference between the spherical function and the quadratic function is tiny. Then, when the spherical phase factor  $R$  increases, the residual phase  $\arg[\tilde{A}_\ell(\boldsymbol{\kappa})]$  becomes more and more complicated, shown in Fig. 6. Indeed, these residual phases require more sampling points and lead to

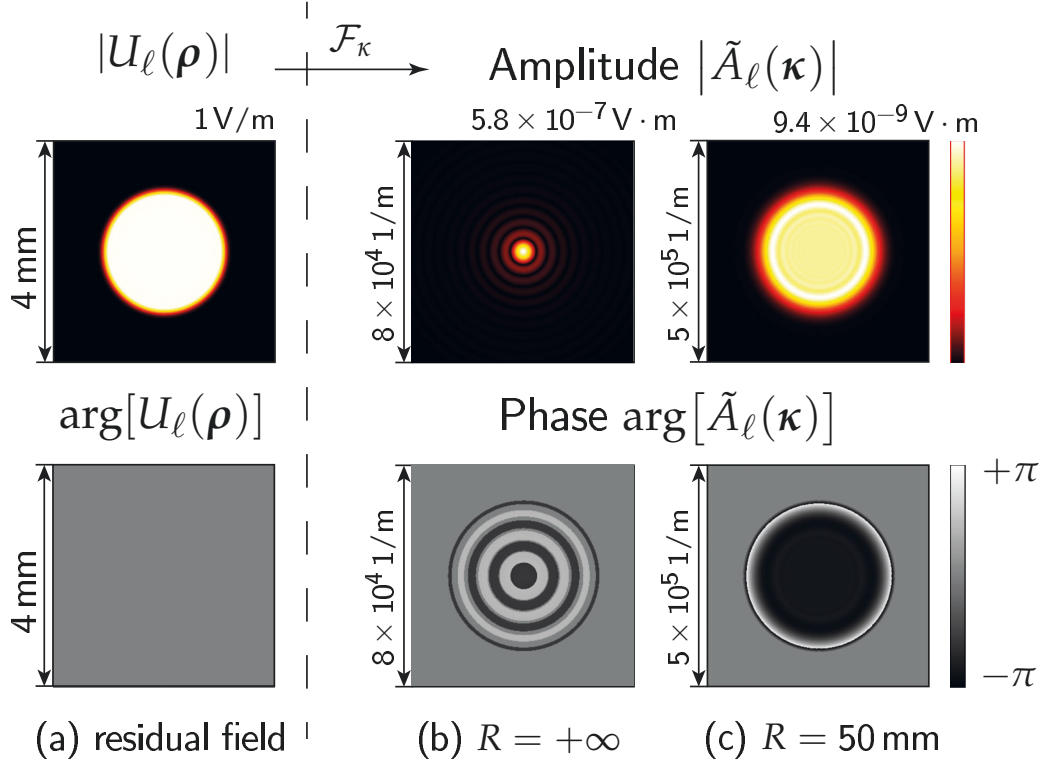


Figure 5: Semi-analytical Fourier transform of a field with a spherical phase, part I.

Panel (a) shows the amplitude distribution of the  $E_x$  component in the spatial domain and the phase distribution of the residual field. The complete working field is defined as  $V_\ell(\rho) = U_\ell(\rho) \exp[\psi^{\text{sph}}(\rho)]$ . Adjusting the spherical radius  $R$  and performing the semi-analytical Fourier transform, we obtain the residual spectrum  $\tilde{A}_\ell(\kappa)$  and analytical quadratic phase in the k-domain. Panel (b) and (c) present the result of semi-analytical Fourier-transform operation for different values of  $R$ .

higher computational effort. The required number of sampling points for FFT and SFT are listed in Table. 2. As we mentioned before, the SFT can deal with the quadratic phases only. Different from the situation of the pure quadratic phase, we can imagine when the spherical radius is very tiny, the resulting residual phase might be even harder sampling than the original spherical phase. The fact proves that the SFT can benefit the Fourier transform for the field with a small or medium spherical phase. But, for field involving an intense wavefront phase, We need other advanced Fourier transform techniques.



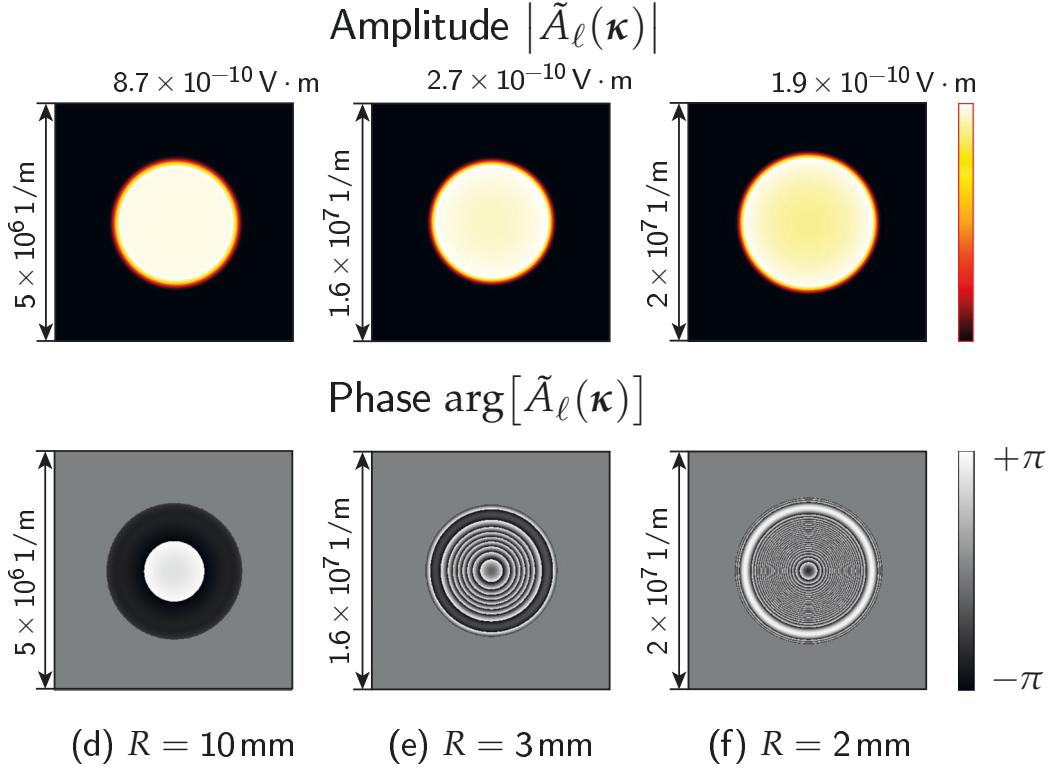


Figure 6: Semi-analytical Fourier transform of a field with a spherical phase, part II. Panels (d) to (f) present the result of semi-analytical Fourier-transform operation for different values of  $R$ . The residual phase  $\arg[\tilde{A}_\ell(\boldsymbol{\kappa})]$  is the phase excluding the quadratic terms. Please note the original light field in the spatial domain is given in Fig. 5(a).

### 2.2.3 Fourier transform of a field with a general wavefront phase

Up to this point, we have investigated the performance of SFT for the field with purely quadratic phases or a spherical phase. In the last example, we would like to consider an exactly practical situation, namely, a field including aberrant phases. We straightforward use the same optical setup as the last experiment to generate the testing light field. But, instead of a varying spherical phase, a general wavefront phase (including aberrant phase) is superimposed on the field behind the mask.

Simulation parameters of the wavefront phase are described in the form of Zernike polynomials and presented in Table. 3. In the last column of the table, the expectation of the quadratic phase handling is given from a mathematical

Table 3: Simulation parameters of the general wavefront phase for the example presented in Section 2.2.3.

name & type	expression	value	handling
spherical phase	$\psi^{\text{sph}} = \text{sgn}(R) k_0 \sqrt{\rho^2 + R^2}$	$R = -3 \text{ mm}$	partly analytical
vertical astigmatism	$Z_2^{-2} = x^2 - y^2$	$c_2^{-2} = 10$	fully analytical
oblique astigmatism	$Z_2^2 = 2xy$	$C_2^2 = 5$	fully analytical
horizontal coma	$Z_3^1 = -2x + 3x^3 + 3xy^2$	$C_3^1 = 2$	numerical

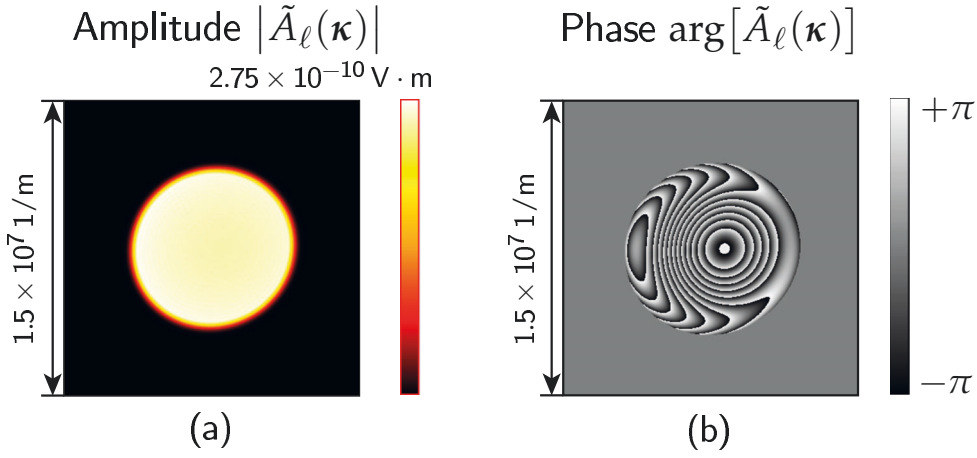


Figure 7: Semi-analytical Fourier transform of a field with a general wavefront phase. Panel (a) and (b) shows amplitude distribution of the  $\tilde{E}_x$ -component  $|\tilde{A}_\ell(\kappa)|$  and the residual phase  $\arg[\tilde{A}_\ell(\kappa)]$ . The original light field in the spatial domain is given in Fig. 5(a).

point of view. In contrast to the situation of a spherical phase, for a general wavefront phase, we cannot use Taylor expansion to estimate the quadratic phase coefficients in terms of the spherical phase factor. Still, we must perform some numerical fitting algorithm to extract the quadratic phase function. Simulation results of the SFT are shown in Fig. 7. Panel (b) presents the residual phase of the resulting spectrum. In line with our expectation, the remained non-quadratic phases are fully numerically handled. Furthermore, comparing the numerical effort of the SFT with the FFT, the sampling effort is significantly reduced from  $(13271 \times 12653)$  to  $(1721 \times 1683)$ .

## HOMEOMORPHIC FOURIER TRANSFORM

---

In Chapter 2, we proposed the so-called semi-analytical Fourier transform, which can be applied to carry out the Fourier transform of the field with a strong quadratic phase efficiently. This technique is established on the properties of the quadratic phase and the convolution and it is a rigorous algorithm. However, this kind of algorithm can fall short in non-paraxial cases. The sampling effort of the semi-analytical Fourier transform is entirely dependent on the sampling of the residual field/ spectrum, which is the remaining part of the electromagnetic field after the extracting of the quadratic phase. In the non-paraxial situation, the semi-analytical Fourier transform will suffer even in the case of the field with the most common spherical wavefront phase. Because of the increasing of the divergent angle, the difference between the spherical phase and the quadratic phase becomes too significant to be neglected. The residual phase has to be treated in the form of “ $2\pi$ -modulo” that the wrapped phase leads to much larger sample numbers necessary for good resolution. Therefore, in this chapter, we propose another approximated algorithm to compute the Fourier transform in such a situation.

Through several practical experiments, we observe that the Fourier transform of fields with strong wavefront phases exhibits behavior that can be described as a bijective mapping of the amplitude distribution. Hence, we name this operation “homeomorphic Fourier transform”. From the mathematical point of view, the Fourier-transform integrals are rapidly oscillating functions in the case of strong wavefront phases. There is a mathematical method, working on the basis of an asymptotic approximation to integrals of such rapidly varying functions, which occasionally comes up in wave theory, applied usually with the aim of obtaining an analytical solution to a specific problem (as is the case with the Debye integral): the Method of Stationary Phase (MSP). Jakob J. Stamnes already revealed the connection between waves and rays with the application of the Method of Stationary Phase in his publication. Despite the MSP being an

algorithm with a much more general scope of application to the Fourier integral [88], the author restricted its application only to the spherical phase or the quadratic phase [89]. In what follows, we generalize the usage of the method of stationary phase to the Fourier transform integral without any constraints on the wavefront phase. The full derivation is presented in Section 3.1, taking as our starting point an alternative expression of the electromagnetic field in which the wavefront phase is extracted, and using the method of stationary phase to solve the integrand. After that, in Section 3.2 we consider the application of the algorithm to numerical simulations. In four groups of experiments, we select different wavefront phases and test their influence on the Fourier transform, from the most fundamental spherical phase, through the case where a single aberration term is present, to a general arbitrary numerical phase. Simulation results are presented alongside an accuracy and efficiency analysis to illustrate the advantages of the homeomorphic Fourier transform.

### 3.1 THEOREM DERIVATION

#### 3.1.1 Homeomorphic Fourier transform

Like the semi-analytical Fourier transform in Section 2.1.1, let us start from the general expression of any electromagnetic field component that we can write the field component in terms of its amplitude and phase,

$$V_\ell(\boldsymbol{\rho}) = |V_\ell(\boldsymbol{\rho})| \exp\{i \arg[V_\ell(\boldsymbol{\rho})]\}. \quad (43)$$

In optics, it is very typical to encounter fields that possess a smooth wavefront, which is common to all field components, for instance, the spherical phase in the far-field region. In such kind of situation, Eq. (43) can be reformulated to yield

$$V_\ell(\boldsymbol{\rho}) = U_\ell(\boldsymbol{\rho}) \exp[i\psi(\boldsymbol{\rho})]. \quad (44)$$

Here, we extract the smooth wavefront phase  $\psi(\boldsymbol{\rho})$  and grouped the rest of the phase alongside the amplitude  $|V_\ell(\boldsymbol{\rho})|$  into  $U_\ell(\boldsymbol{\rho})$ . From a mathematical point of view, there is no approximation in the reformulation of Eq. (44). It merely constitutes an alternative way to express  $V_\ell(\boldsymbol{\rho})$ .

We have now rewritten the expression of our field component in a way which isolates the troublesome phase term  $\exp[i\psi(\rho)]$ , so now, considering that the present discussion is not merely concerned with the underlying mathematics, but also with the implementation of the method for simulation purposes, in order to numerically store  $V_\ell(\rho)$  we could follow a hybrid sampling strategy, one which employs different sampling and interpolation techniques for the two terms involved, namely,  $U_\ell(\rho)$  and  $\exp[i\psi(\rho)]$ : a strict equidistant Nyquist sampling applied to the residual complex amplitude  $U_\ell(\rho)$ , and a non-equidistant sampling approach for the smooth wavefront phase  $\psi(\rho)$ , with such varied options as spline or quadratic interpolation methods available for  $\psi(\rho)$ . The application of this hybrid approach provides a workaround that allows us to avoid having to sample the exponential term associated with the wavefront phase, as  $N\{\exp[i\gamma(\rho)]\} \gg N[\gamma(\rho)]$ . Very often, in the absence of the wrapped wavefront phase, the sampling of  $U_\ell(\rho)$  does not pose much of a challenge, and  $N(V) \gg N(U)$ . Consequently, for strong wavefront phases, the hybrid sampling strategy can result in a dramatic decrease of the computational effort.

Then, from a practical point of view, let us analyze the practicalities of the hybrid sampling strategy. The most important two questions are how to obtain the smooth wavefront phase and how to deal with it in actual simulations of optical systems. The complete solution to obtain the optimal smooth wavefront phase from arbitrary complex field data is to combine the phase unwrapping algorithm and an appropriate interpolation algorithm. However, it is common for the wavefront phase to be directly established with the model of the source, e.g., an ideal spherical wave. And then, for most optical components, the physical response of the element on the wavefront phase is known. For instance, in the case of lenses and interfaces. However, for Fourier transform operations, there is no straightforward solution: the Fast Fourier Transform (FFT) algorithm cannot handle a field sampled in a hybrid manner. With an eye to taking the numerical advantage of the hybrid sampling strategy into the Fourier transform, we have developed the following algorithm.

Now, let us consider the Fourier transform integral and insert the alternative expression of the field into it.

$$\begin{aligned}\tilde{V}_\ell(\boldsymbol{\kappa}) &= \frac{1}{2\pi} \iint_{-\infty}^{\infty} V_\ell(\boldsymbol{\rho}) \exp(-i\boldsymbol{\rho} \cdot \boldsymbol{\kappa}) d^2\rho \\ &= \frac{1}{2\pi} \iint_{-\infty}^{\infty} U_\ell(\boldsymbol{\rho}) \exp[i\psi(\boldsymbol{\rho}) - i\boldsymbol{\rho} \cdot \boldsymbol{\kappa}] d^2\rho,\end{aligned}\tag{45}$$

where the tilde in  $\tilde{V}$  makes explicit reference to a function defined in the spatial frequency domain, spanned by  $\boldsymbol{\kappa}$ , as opposed to a function defined in the space domain – spanned by  $\boldsymbol{\rho}$ , as already introduced above – which would have no diacritic.

Comparing Eq. (45) with the stationary phase approximation formula, we can see several glaring similarities. The main idea of stationary phase methods relies on the cancellation of triangular function with a rapidly varying phase. The derivation and working assumption can be found in the work by XXX. Consequently, from the cited literature, we can directly extract the following two precondition for the usage of the stationary phase method:

- The term  $U_\ell(\boldsymbol{\rho})$  must be slowly varying.
- In the domain where the transversal position vector  $\boldsymbol{\rho}$  is defined, there is one and only one critical point of the first kind defined by the formula  $\nabla_\perp [\psi(\boldsymbol{\rho}) - \boldsymbol{\rho} \cdot \boldsymbol{\kappa}] = 0$ .

Mathematically, the first condition means that the exponential term in Eq. (45) has a character of high-frequency oscillation in the given definition domain. The exponential term dominates the integrand so that  $U_\ell(\boldsymbol{\rho})$  can be regarded as a constant term and be taken out of the integral. From the second condition, we can conclude a bijective mapping from the spatial domain to the spatial frequency domain, i.e. a homeomorphism.

With the help of the method of stationary phase, the following result can be deduced from Eq. (45):

$$\tilde{V}_\ell(\boldsymbol{\kappa}) \approx a[\boldsymbol{\rho}(\boldsymbol{\kappa})] U_\ell[\boldsymbol{\rho}(\boldsymbol{\kappa})] \exp\{i\psi[\boldsymbol{\rho}(\boldsymbol{\kappa})] - i\boldsymbol{\kappa} \cdot \boldsymbol{\rho}(\boldsymbol{\kappa})\},\tag{46}$$

with the bijective mapping relation  $\boldsymbol{\rho} \rightarrow \boldsymbol{\kappa}$

$$\nabla_\perp \psi(\boldsymbol{\rho}) = \boldsymbol{\kappa},\tag{47}$$

and with

$$a(\boldsymbol{\rho}) = \begin{cases} \sqrt{\frac{i}{\psi_{xx}(\boldsymbol{\rho})}} \sqrt{-\frac{i\psi_{xx}(\boldsymbol{\rho})}{\psi_{xy}^2(\boldsymbol{\rho}) - \psi_{xx}(\boldsymbol{\rho})\psi_{yy}(\boldsymbol{\rho})}} & , \quad \psi_{xx}(\boldsymbol{\rho}) \neq 0 \\ \frac{1}{|\psi_{xy}(\boldsymbol{\rho})|} & , \quad \psi_{xx}(\boldsymbol{\rho}) = 0 \end{cases}, \quad (48)$$

where  $\psi_{x_i x_j} \stackrel{\text{def}}{=} \frac{\partial^2 \psi}{\partial x_i \partial x_j}$ .

Remarkably, we can also write the Eq. (48) into a compact form,

$$a(\boldsymbol{\rho}) = \sigma(\boldsymbol{\rho}) \frac{1}{\sqrt{|\psi_{xy}^2(\boldsymbol{\rho}) - \psi_{xx}(\boldsymbol{\rho})\psi_{yy}(\boldsymbol{\rho})|}} \quad (49)$$

with

$$\sigma(\boldsymbol{\rho}) = \begin{cases} \sqrt{i} \cdot \sqrt{i} & = i \\ \sqrt{i} \cdot \sqrt{-i} & = 1 \\ \sqrt{-i} \cdot \sqrt{-i} & = -i \end{cases}. \quad (50)$$

where  $\sqrt{i} = \frac{1+i}{2}$  and  $\sqrt{-i} = \frac{1-i}{2}$  indicate the sign of the square root term in Eq. (48).

The sign (in a broad sense of the word) of the amplitude scaling factor  $a(\boldsymbol{\rho})$  defined in Eq. (49), i.e.,  $\sigma(\boldsymbol{\rho}) = \text{sgn}[a(\boldsymbol{\rho})]$ , can take one of the three possible values:  $i$ ,  $-i$  and  $1$ . Each of these three options has its own physical implications: the first two have already been analyzed in literature and correspond, respectively, to a convergent wavefront or a divergent wavefront of the light field. The third case,  $\text{sign}[\sigma(\boldsymbol{\rho})] = 1$ , denotes a situation in which the light field possesses an astigmatic wavefront phase, namely, the light field is convergent on one dimension and divergent on the other dimension.

Then, let us have deep learning on the relationship between the wavefront and the sign of the amplitude scaling factor from the mathematical point of view. From Eq. (48), we know that the sign of the amplitude scaling factor are determined by the second derivative term  $\psi_{xx}(\boldsymbol{\rho}) / \psi_{yy}(\boldsymbol{\rho})$  and the determinant term  $\psi_{xy}^2(\boldsymbol{\rho}) - \psi_{xx}(\boldsymbol{\rho})\psi_{yy}(\boldsymbol{\rho})$ . Hence, it is essential to know how these terms associate with the wavefront of the field. In differential geometry, we find the concept of “the second fundamental form” [90, 91] which is a quadratic form on the tangent plane of a smooth surface in the three-dimensional Euclidean space.



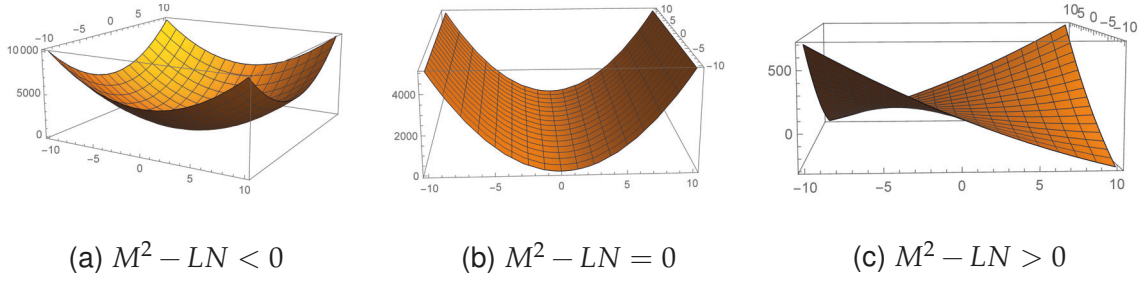


Figure 8: Illustration of the relationship between the geometric shape and the second fundamental form of a smooth parametric surface. Panel (a) shows that when the determinant of the second fundamental form is negative-valued, there is only one intersection point between the parametric surface and its tangent plane. Panel (b) presents that in the case of the determinant of the second fundamental form is zero-valued, the surface intersects its tangent plane with one line, which passes through the selected local point. Panel (c) illustrates when the determinant of the second fundamental form is positive-valued, the surface intersects its tangent plane with two lines, which intersect at the selected local point.

It serves to qualify the extrinsic invariant of the surface, its principal curvatures. The second fundamental form of any smooth surface can be written as

$$\begin{aligned} \mathbb{I}_\psi &= Ldx^2 + 2Mdx dy + Ndy^2 \\ &= \psi_{xx}(\rho) dx^2 + 2\psi_{xy}(\rho) dx dy + \psi_{yy}(\rho) dy^2. \end{aligned} \quad (51)$$

Based on the knowledge of differential geometry, we have the following conclusions:

- $M^2 - LN = \psi_{xy}^2(\rho) - \psi_{xx}(\rho)\psi_{yy}(\rho) < 0$ : There is no intersection between the surface and its tangent plane except the selected local point. Fig. 8 (a)
- $M^2 - LN = \psi_{xy}^2(\rho) - \psi_{xx}(\rho)\psi_{yy}(\rho) = 0$ : The surface intersects its tangent plane with one line, which passes through the selected local point. Fig. 8 (b)
- $M^2 - LN = \psi_{xy}^2(\rho) - \psi_{xx}(\rho)\psi_{yy}(\rho) > 0$ : The surface intersects its tangent plane with two lines, which intersect at the selected local point. And this point is called hyperbolic point. Fig. 8 (c)

Consequently, we know that the shape of the parametric surface is corresponding to the sign of the determinant term. Meanwhile, Eq. (49) tells us that the



Table 4: Physical implications of the amplitude scaling factor of the forward homeomorphic Fourier transform.

$\psi_{xx}(\boldsymbol{\rho})$ and $\psi_{yy}(\boldsymbol{\rho})$	$\psi_{xy}(\boldsymbol{\rho})$	$\psi_{xy}^2(\boldsymbol{\rho}) - \psi_{xx}(\boldsymbol{\rho})\psi_{yy}(\boldsymbol{\rho})$	wavefront	$\sigma(\boldsymbol{\rho})$
one/both = 0	$\neq 0$	$> 0$	astigmatic	1
different sign	any	$> 0$	astigmatic	1
same sign (+ / -)	large	$> 0$	astigmatic	1
same sign (+)	small	$< 0$	divergent	i
same sign (-)	small	$< 0$	convergent	-i

determinant term can not be zero-valued. Thus, considering the constraints of the second derivative term of the wavefront phase and all possibilities of permutation and combination for the sign of the second derivative terms, we can summarize the physical meaning of the scaling factor in Tab. 4.

So far, so forth, the full derivation of the homeomorphic Fourier transform and the corresponding physical interpretation are given in detail. It should be noted that the derivation presented above incurs no approximation whatsoever up to and including Eq. (45). It is only when the two preconditions for the validity of the stationary phase method are employed in the simplification of the Fourier integral to produce Eq. (46) that we finally abandon the path of full rigor. The resulting expression (namely, as already stated, Eq. (46)) constitutes an approximation, albeit a good and accurate one as long as the two aforementioned preconditions hold.

### 3.1.2 The inverse homeomorphic Fourier transform

The derivation of the inverse operation can be performed in an analogous manner. Let us then start from the spectrum of the field,  $\tilde{V}_\ell(\boldsymbol{\kappa})$ , and rewrite it by extracting a smooth wavefront phase term, like we did for the direct homeomorphic Fourier transform in Eq. (44):

$$\tilde{V}_\ell(\boldsymbol{\kappa}) = \tilde{A}_\ell(\boldsymbol{\kappa}) \exp[i\tilde{\psi}(\boldsymbol{\kappa})]. \quad (52)$$

Identifying this expression with the direct homeomorphic Fourier transform presented in Eq. (46) it is possible to write  $\tilde{A}_\ell(\boldsymbol{\kappa})$  and  $\tilde{\psi}(\boldsymbol{\kappa})$  as follows:

$$\begin{cases} \tilde{A}_\ell(\boldsymbol{\kappa}) &= \alpha[\boldsymbol{\rho}(\boldsymbol{\kappa})] U_\ell[\boldsymbol{\rho}(\boldsymbol{\kappa})] \\ \tilde{\psi}(\boldsymbol{\kappa}) &= \psi[\boldsymbol{\rho}(\boldsymbol{\kappa})] - \boldsymbol{\kappa} \cdot \boldsymbol{\rho}(\boldsymbol{\kappa}) \end{cases}. \quad (53)$$

We can then use Eq. (52) to substitute for  $\tilde{V}_\ell(\boldsymbol{\kappa})$  in the definition of the inverse Fourier transform integral

$$\begin{aligned} V_\ell(\boldsymbol{\rho}) &= \frac{1}{2\pi} \iint_{-\infty}^{\infty} \tilde{V}_\ell(\boldsymbol{\kappa}) \exp(i\boldsymbol{\rho} \cdot \boldsymbol{\kappa}) d^2\boldsymbol{\kappa} \\ &= \frac{1}{2\pi} \iint_{-\infty}^{\infty} \tilde{A}_\ell(\boldsymbol{\kappa}) \exp[i\tilde{\psi}(\boldsymbol{\kappa}) + i\boldsymbol{\rho} \cdot \boldsymbol{\kappa}] d^2\boldsymbol{\kappa}. \end{aligned} \quad (54)$$

Again, carrying out a similar process as that for the direct transform, the smooth phase term  $\tilde{\psi}(\boldsymbol{\kappa})$  will provide the inverse bijective mapping relation  $\boldsymbol{\kappa} \rightarrow \boldsymbol{\rho}$ ,

$$\tilde{\nabla}_\perp \tilde{\psi}(\boldsymbol{\kappa}) = -\boldsymbol{\rho}. \quad (55)$$

Applying the method of stationary phase, the integral in Eq. (54) becomes

$$V_\ell(\boldsymbol{\rho}) = \tilde{a}[\boldsymbol{\kappa}(\boldsymbol{\rho})] \tilde{A}_\ell[\boldsymbol{\kappa}(\boldsymbol{\rho})] \exp\{i\tilde{\psi}[\boldsymbol{\kappa}(\boldsymbol{\rho})] + i\boldsymbol{\rho} \cdot \boldsymbol{\kappa}(\boldsymbol{\rho})\}, \quad (56)$$

with

$$\tilde{a}(\boldsymbol{\kappa}) = \begin{cases} \sqrt{\frac{i}{\tilde{\psi}_{k_x k_x}(\boldsymbol{\kappa})}} \sqrt{-\frac{i\tilde{\psi}_{k_x k_x}(\boldsymbol{\kappa})}{\tilde{\psi}_{k_x k_y}^2(\boldsymbol{\kappa}) - \tilde{\psi}_{k_x k_x}(\boldsymbol{\kappa}) \tilde{\psi}_{k_y k_y}(\boldsymbol{\kappa})}} & , \quad \tilde{\psi}_{k_x k_x}(\boldsymbol{\kappa}) \neq 0 \\ \frac{1}{|\tilde{\psi}_{k_x k_x}(\boldsymbol{\kappa})|} & , \quad \tilde{\psi}_{k_x k_x}(\boldsymbol{\kappa}) = 0 \end{cases}. \quad (57)$$

As same as the forward homeomorphic Fourier transform, we can also rewrite the scaling factor for the inverse transformation in a compact form,

$$\tilde{a}(\boldsymbol{\kappa}) = \tilde{\sigma}(\boldsymbol{\kappa}) \sqrt{\frac{1}{|\tilde{\psi}_{k_x k_y}^2(\boldsymbol{\kappa}) - \tilde{\psi}_{k_x k_x}(\boldsymbol{\kappa}) \tilde{\psi}_{k_y k_y}(\boldsymbol{\kappa})|}}. \quad (58)$$

According to the sign of the second derivative terms, we can justify the characteristics of the wavefront for the given spectrum. In Table. 5, we present the examining conditions and corresponding physical interpretation. It is then possible to identify the terms

$$\begin{cases} U_\ell(\boldsymbol{\rho}) &= \tilde{a}[\boldsymbol{\kappa}(\boldsymbol{\rho})] \tilde{A}_\ell[\boldsymbol{\kappa}(\boldsymbol{\rho})] \\ \psi(\boldsymbol{\rho}) &= \tilde{\psi}[\boldsymbol{\kappa}(\boldsymbol{\rho})] + \boldsymbol{\rho} \cdot \boldsymbol{\kappa}(\boldsymbol{\rho}) \end{cases}, \quad (59)$$

in Eq. (56), so that after subsequent application of first the direct and then the inverse homeomorphic Fourier transforms, the original expression of the field  $V_\ell(\boldsymbol{\rho})$  is retrieved, thus proving the consistency of the method.

Table 5: Physical implications of the amplitude scaling factor for the inverse homeomorphic Fourier transform.

$\tilde{\psi}_{k_x k_x}(\kappa)$ and $\tilde{\psi}_{k_y k_y}(\kappa)$	$\tilde{\psi}_{k_x k_y}(\kappa)$	$\tilde{\psi}_{k_x k_y}^2(\kappa) - \tilde{\psi}_{k_x k_x}(\kappa) \tilde{\psi}_{k_y k_y}(\kappa)$	wavefront	$\tilde{\sigma}(\kappa)$
one/both = 0	$\neq 0$	$> 0$	astigmatic	1
different sign	any	$> 0$	astigmatic	1
same sign (+/-)	large	$> 0$	astigmatic	1
same sign (+)	small	$< 0$	convergent	i
same sign (-)	small	$< 0$	divergent	-i

### 3.1.3 Validity condition and the numerical criterion

The present discussion is not merely concerned with the theoretical derivation, but also with the implementation of the method for practical simulation. It is worthwhile at this point to emphasize the numerical criterion for the validity conditions of the homeomorphic Fourier transform. As presented in the last two sections, when the homeomorphic Fourier transform is allowed, two preconditions must be fulfilled. Thus, we can design a practical criterion in terms of these two conditions.

*Condition one: “slowly varying”*

Let us start from the first condition: the residual field  $U_\ell(\rho)$  is slowly varying. Physically, “slowly varying” means that the given field doesn’t involve high-frequency components. Since both “slowly varying” or “high-frequency” are relative concepts, an appropriate reference is inevitable. Apparently, we should select the entire field  $V_\ell(\rho)$  as a reference for the comparison. Theoretically, we need respectively to perform the Fourier transform on the residual field and the entire field and then compare their spectrum bandwidth. If the bandwidth of the residual field is much smaller than the bandwidth of the entire field, we can say that the wavefront phase dominates the Fourier transform. Here, we introduce four variables to indicate the bandwidth of the residual/entire field on x-and y-dimension.

- $(\Delta k_x^U, \Delta k_y^U)$ : bandwidth of the residual field  $\mathcal{F}_\kappa [U_\ell(\rho)]$ .
- $(\Delta k_x^V, \Delta k_y^V)$ : bandwidth of the entire field  $\mathcal{F}_\kappa^h \{U_\ell(\rho) \exp [i\psi(\rho)]\}$ ,

According to the hybrid sampling strategy, the residual field is sampled numerically on the equidistant grid. Therefore, we can directly perform FFT to calculate its spectrum  $\mathcal{F}_\kappa [U_\ell(\rho)]$ . On the other hand, instead of the fully sampling of the exponential phase term, we only store the information of the wavefront phase numerically in the manner of non-equidistant sampling [92]. It doesn't make sense to resample the wavefront phase and use FFT to the calculation of the spectrum of the entire field. Therefore, in practice, we recommend enforcing the pointwise Fourier transform on the entire field,  $\mathcal{F}_\kappa^h \{U_\ell(\rho) \exp [i\psi(\rho)]\}$ . Here, the mapping relation follows the gradient of the wavefront phase, given in Eq. (47). Finally, we obtain the Fourier transform for both the residual field and the entire field.

Remarkably, the determination of the bandwidth is based on the theory of second-order moments. Corresponding physical operators and mathematical expression can be found in the book. Besides, since the vector's feature of the electric field, i.e.,  $E(\rho) = \{E_x(\rho), E_y(\rho), E_z(\rho)\}$ , need to be taken into account, the above calculation must be done for all three electric-field components. To this end, we would like to introduce two variables to describe the resulting ratio of the bandwidth:

$$\begin{cases} p_x = \text{Min}\left(\frac{\Delta k_x^{V_1}}{\Delta k_x^{U_1}}, \frac{\Delta k_x^{V_2}}{\Delta k_x^{U_2}}, \frac{\Delta k_x^{V_3}}{\Delta k_x^{U_3}}\right) \\ p_y = \text{Min}\left(\frac{\Delta k_y^{V_1}}{\Delta k_y^{U_1}}, \frac{\Delta k_y^{V_2}}{\Delta k_y^{U_2}}, \frac{\Delta k_y^{V_3}}{\Delta k_y^{U_3}}\right) \end{cases}. \quad (60)$$

Consequently, when the bandwidth of the entire field is much larger than the residual field, the resulting ratio factors are some values much larger than 1. In this situation, we can say the residual field is slowly varying and the Fourier transform is dominated by the wavefront phase term. Finally, we would like to emphasize that the user can specify the threshold value adjustable. Based on our experience, the selection of the threshold refers to the Fresnel number and we recommend setting the critical value is equal to 200,  $p^{\text{critical}} = 200$ .

*Condition two: homeomorphism*

The second validity condition is about the **constraint of the wavefront phase**. It requires that in the definition domain of the coordinates, there is one and only **one critical point of the first kind** defined by the formula  $\nabla_{\perp} [\psi(\rho) - \rho \cdot \kappa] = 0$ . From a mathematical point of view, the qualified **wavefront must be smooth** (continuous and differentiable). It also must be capable of generating a bijective mapping relation, following the gradient equation, between the Fourier domain and the original domain. Thus, the second validity condition can be referred to as the **homeomorphism condition or the bijectivity condition**. The characteristics of the bijection and how they relate to the generation of a homeomorphism are shown in the Appendix. In a short, for the given smooth wavefront phase  $\psi(\rho)$ , the homeomorphism condition is contained in the requirement that the determinant of the Hessian matrix  $\psi_{xy}^2(\rho) - \psi_{xx}(\rho) \psi_{yy}(\rho)$  are all non-negative or non-positive.

As we mentioned in the previous sections, in practice, the wavefront phase is numerically stored in the manner of non-equidistant sampling. That means we need to compute the determinant of the Hessian matrix per data points and examine whether their signs are the same. However, in general, we only store the coordinates vector, the gradient vector, and the phase value per data point. Due to the lack of the second derivative terms, it is not straightforward to achieve the Hessian determinant. To overcome this difficulty, we must select some appropriate interpolation technique, which allows the evaluation of the derivative terms. Comparing to some regular techniques, e.g., cubic interpolation [93] or quadratic interpolation [94], we recommend using the B-spline interpolation method [95–97]. Importantly, the construction of the B-Spline interpolation requires only the function value, and then it allows the evaluation for both the function value and gradient value. In our case, by providing the gradient vector information, we can obtain the corresponding second derivative terms. Finally, we can achieve the calculation of the determinant of the Hessian matrix.

As a summary of this section, we conclude the two numerical criteria to examine whether the HFT or IHFT is valid for the given field/spectrum.

1. The slowly varying condition

both  $p_x$  and  $p_y$  are larger than the threshold (The selection of the threshold can refer to the Fresnel number, which establishes a coarse criterion to define the near and far-field approximations. We recommend setting the threshold is equal to 200,  $p^{\text{critical}} = 200$ .)

2. The homeomorphism condition

the determinants of the Hessian matrix  $\psi_{xy}^2(\boldsymbol{\rho}) - \psi_{xx}(\boldsymbol{\rho}) \psi_{yy}(\boldsymbol{\rho})$  are all non-negative or non-positive in the definition domain of the light field.

### 3.1.4 Pointwise Fourier transform in the case of a non-bijective wavefront phase

In the previous sections, the precondition of the homeomorphic Fourier transform and the corresponding numerical criteria have been demonstrated in detail. However, in an optics context, it is very common to encounter the working field or spectrum with strong aberration. In such kind of situation, the pre-requisite for bijection is not fulfilled which leads to all formulas derived in the first two sections that will totally be unavailable. Therefore, we must develop another robust algorithm and extend the validity of the HFT.

As before, we start from the decomposition of the electric field as shown in the Eq. (44). In this step, we have total freedom when deciding exactly what part of the total phase is included in the wavefront phase  $\psi(\boldsymbol{\rho})$ , and what part remains in residual field  $U_\ell(\boldsymbol{\rho})$ . In the case of the non-bijective wavefront phase, we aim to extract the bijective part from the original smooth phase term  $\psi(\boldsymbol{\rho})$  and name it as  $\psi^{\text{map}}(\boldsymbol{\rho})$ .

$$\begin{aligned} V_\ell(\boldsymbol{\rho}) &= U_\ell(\boldsymbol{\rho}) \exp[i\psi(\boldsymbol{\rho})] = \\ &= U_\ell(\boldsymbol{\rho}) \exp[i\psi^{\text{res}}(\boldsymbol{\rho})] \exp[i\psi^{\text{map}}(\boldsymbol{\rho})] . \end{aligned} \quad (61)$$

In the following process, we employ the modified homeomorphic Fourier transform, which is based on the bijective part of the wavefront phase, on the given field. Thus, the choice of the bijective phase part will affect the accuracy of the HFT. Our aim is to contain as much of the bijective phase as possible from the original wavefront phase. But we must bear in mind that the condition for bijectivity must prevail, as on it hinges the consistency of the definition of the

HFT/IHFT method. Indeed, we need a workflow to eliminate the part of that non-bijectivity while leaving as much of the bijective phase as possible intact. For the numerical simulation of similar tasks, we propose the following workflow:

1. Perform phase fitting on the initial wavefront phase.

As a first step, with the help of fitting techniques, we sequentially extract the linear phase, spherical phase and Zernike terms from the initial smooth phase  $\psi(\rho)$ . The fitting result can be expressed as  $\psi(\rho) = \psi^{\text{fit}}(\rho) + \psi^{\text{res}}(\rho)$ , where the difference  $\psi^{\text{res}}$  between the original phase  $\psi$  and the fitted result  $\psi^{\text{fit}}$  should be very small so that it can be negligible.

$$\psi^{\text{fit}}(\rho) = \psi^{\text{linear}}(\rho) + \psi^{\text{sph}}(\rho) + \psi_0^{\text{zer}}(\rho) \quad (62)$$

where the  $\psi_0^{\text{zer}}(\rho)$  indicates the resulting Zernike phase, in terms of the default fitting module. Usually, the maximum order of the Zernike polynomial is customized by the user.

2. Elementary optimization.

Since the analytical expression of the fitting model is known, we can now examine whether the result of the fitting  $\psi^{\text{fit}}(\rho)$  is bijective, according to the homeomorphism criterion (as presented in the Appendix). Numerically, we compute the second derivatives of the fitted phase  $\psi^{\text{fit}}$  at the position of each sampling point, and check whether they have the same sign. If this check reveals a non-bijective phase, an iterative approach is introduced to omit the highest-order term in the list of Zernike polynomials and afterward re-examine the homeomorphism criterion. This step is repeated until a bijective phase  $\psi_0^{\text{map}}(\rho)$  is obtained.

$$\psi_0^{\text{map}}(\rho) = \psi^{\text{linear}}(\rho) + \psi^{\text{sph}}(\rho) + \psi^{\text{zer}}(\rho) \quad (63)$$

where  $\psi_0^{\text{map}}(\rho)$  is the first guess of the bijective phase and  $\psi^{\text{zer}}(\rho)$  corresponds to the residual bijective part of the Zernike phase.

3. Advanced optimization.

In the elementary optimization we roughly omit the highest-order Zernike

term, but it is important to note that Zernike polynomials are global functions which operate on the entirety of the definition domain, and many commonly encountered cases of non-bijective phases are caused by local phase defects. It would then make sense, taking the result of the elementary optimization as the starting point, to perform a more thorough investigation of the possible sources of the violation of bijectivity. In practice, due to the different methods used in the wavefront phase interpolation, the specific approach would be quite different. For example, if we use the quadratic interpolation method to store the initial wavefront phase information on a non-equidistant grid, we recommend applying the following strategy: First of all, we need to convert the elementary analytical result  $\psi_0^{\text{map}}(\boldsymbol{\rho})$  onto the same non-equidistant grid. Generally, we need two data sets. One is to store the coordinate information  $\boldsymbol{\rho} = (x, y)$ . The other one is to save the direction information  $\mathbf{s}(\boldsymbol{\rho}) = (s_x, s_y, s_z)$ . It should be noted that data of the position vector are the same for both phases, but data of the direction vector are different for the original phase and elementary bijective phase. In the second step, we propose an iterative optimization. For each sampled point, we try to modify the local bijective direction vector with the compensating direction. The compensating direction is equal to the difference between the original local direction and the local elementary bijective direction. Afterward, we need to examine the homeomorphism condition. If it is still bijective, we proceed with the next point. Otherwise, we can reduce the compensating direction vector half and repeat this process until ten times or fulfilling the homeomorphism condition. For a better result, we must scan all positions several times, and finally, we can obtain the optimal bijective phase part  $\psi^{\text{map}}(\boldsymbol{\rho})$ .

We would now, after the application of the steps described above, have succeeded in the extraction of the bijective phase part  $\psi^{\text{map}}(\boldsymbol{\rho})$ , which provides the mapping relation from spatial domain to the frequency domain  $\boldsymbol{\rho} \rightarrow \boldsymbol{\kappa}$ ,

$$\boldsymbol{\kappa}^{\text{map}} = \nabla_{\perp} \psi^{\text{map}}(\boldsymbol{\rho}). \quad (64)$$

We could now apply the stationary phase method to the expression Eq. (61), but this time using the mapping relation from Eq. (64). The resulting expression is



the same as the standard homeomorphic Fourier transform. It reveals that the only difference is that the general mapping relation has been replaced by the bijective mapping. The approximation intrinsic to the forced regularization of the mapping relation will certainly lead to a dislocation in the spectrum position and a resulting, inevitable, error. This error can be numerically investigated and compared against a given accuracy threshold, on the basis of which the final decision could be made whether to go ahead with the application of the homeomorphic Fourier transform in that specific case, or to discard it in favor of the rigorous variant.

### 3.2 NUMERICAL EXAMPLES

In the previous sections, the background knowledge and theoretical derivation of the homeomorphic Fourier transform algorithm have been introduced. However, one of the most promising aspects of this concept in pragmatic terms is its application in computer simulations of optical systems. In the following sections, we will present several illustrative examples of the application of this technique. All simulations were done with the physical optics modeling and design software VirtualLab Fusion.

#### 3.2.1 *Fourier transform of a field with spherical phase*

In the first example, we would like to consider the most simple optical scene: Fourier transform of a field with a spherical phase. To carry out the simulation, we build up the corresponding optical setup: an ideal plane wave illuminates a house-shaped mask behind which a divergent spherical phase is superimposed onto the field. The spherical phase can be expressed as  $\psi^{\text{sph}}(\rho) = \text{sgn}(R) k_0 \tilde{n} \sqrt{\rho^2 + R^2}$ , where the factor  $R$  indicates to the radius of the curvature of the spherical wavefront. Since the working spherical phase is divergent,  $R$  is taken on a positive value. In this set of experiments, we fix the ideal plane wave which is  $E_x$  polarized at 532 nm, and the size of the house-shaped mask. Therefore, the amplitude distribution of the working field is always the same, as per Fig. 9 (a), which shows the  $E_x$  component of the field behind the mask.

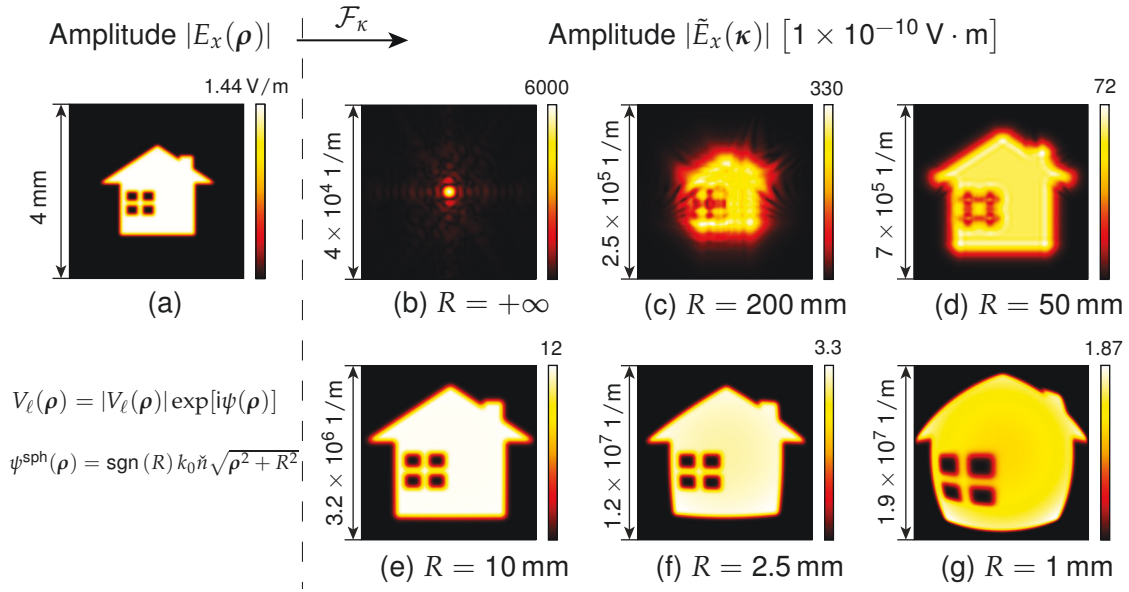


Figure 9: Fast Fourier transform of a field with house-shaped amplitude and different values of the spherical-phase radius. Panel (a) shows the amplitude distribution of the  $E_x$  component in the spatial domain, common starting point to all results. A spherical phase with radius of curvature  $R$  is then superimposed on this amplitude, and its Fourier transform computed. Panels (b) to (g) present the  $\tilde{E}_x$  component (i.e. the result of said Fourier-transform operation) for different values of  $R$ , as indicated below each of the individual panels. The required numbers of sampling points of fast Fourier transform for each case are given in Tab. 6.

In the functional phase plate, we can configure the radius of curvature  $R$  of the spherical phase and then superimpose it onto the amplitude. The factor  $R$  is employed as the variable in this set of experiments.

Simulation results of the Fourier transform corresponding to different values of  $R$  is then shown in Fig. 9 (b)–(g). The case of  $R = +\infty$ , which is pictured in panel (b), is the limit case of a planar wavefront. We cannot see any resemblance between its original pattern and its Fourier transform. It shows the integral nature of the Fourier-transform operation. On the other hand, as the magnitude of  $R$  progressively decreases, the importance of the spherical phase increases. Meanwhile, one can ever more and more easily discern a house-shaped distribution *also* in the Fourier transform. In panel (c) and (d), there are still some diffraction effects at the edge of the Fourier pattern. Panel (e) happens to be a

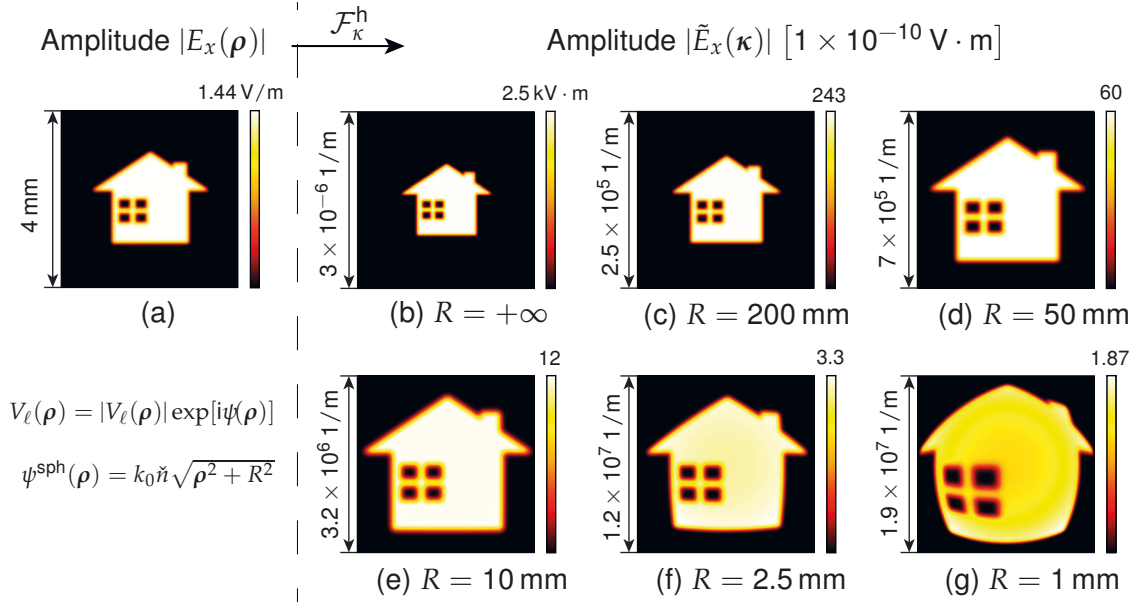


Figure 10: Homeomorphic Fourier transform of the same house-shaped amplitude with a superimposed spherical phase in comparison to Fig. 9. Panel (a) shows the amplitude distribution of the  $E_x$  component in the spatial domain. Panels (b) to (g) present the result of Homeomorphic Fourier-transform operation for different values of  $R$ . Please note the window size of panel (b) and the scale of panels (b) to (d) are different from Fig. 9. The required numbers of sampling points of homeomorphic Fourier transform for each case are given in Tab. 6.

particularly evident instance on that score – the one-to-one bijective mapping behavior is crystal clear by this point. Still, even for stronger distortion, as is the case for the results of panels (f) and (g), the bijective mapping behavior is incontestable, since distortion does not inherently violate the homeomorphism: the definition of a homeomorphism hinges on the fact that the coordinates may be changed by the transformation, but the neighbors of the points remain the same.

The purpose of this experiment is to investigate when the homeomorphic Fourier transform constitutes a good approximation of the rigorous integral. Serving as a contrast, we compute the homeomorphic Fourier transform of the same house-shaped fields, shown in Fig. 10. Besides, we have performed an analysis of the accuracy of the HFT using the FFT as reference. Here, according

Table 6: Comparison of the homeomorphic Fourier transform and the fast Fourier transform: number of sampling points and deviation. The numerical aperture (NA) is defined as  $n \sin \theta = \frac{na}{\sqrt{a^2 + R^2}}$ . Here,  $a$  is the radius of the aperture and  $n$  is the real part of the refractive index of the surrounding medium. Corresponding field distribution results are respectively shown in Fig. 9 and Fig. 10.

spherical radius	NA	sampling (FFT)	sampling (HFT)	deviation
$R = \infty$	NA = 0	$(59 \times 55)$	$(59 \times 55)$	99.99 %
$R = 200 \text{ mm}$	NA = 0.006	$(97 \times 95)$	$(59 \times 55)$	17.17 %
$R = 50 \text{ mm}$	NA = 0.026	$(281 \times 23)$	$(59 \times 55)$	4.1 %
$R = 10 \text{ mm}$	NA = 0.13	$(1299 \times 915)$	$(59 \times 55)$	0.28 %
$R = 2.5 \text{ mm}$	NA = 0.45	$(4557 \times 3323)$	$(59 \times 55)$	0.067 %
$R = 1 \text{ mm}$	NA = 0.71	$(7753 \times 6091)$	$(59 \times 55)$	0.021 %

to Wyrowski and Kuhn, the deviation between the FFT result and the HFT result is evaluated by

$$\text{deviation} := \frac{\sum_{x,y} |\tilde{V}^{\text{FFT}}(\kappa) - \tilde{V}^{\text{HFT}}(\kappa)|^2}{\sum_{x,y} |\tilde{V}^{\text{FFT}}(\kappa)|^2} \quad (65)$$

where the reference  $\tilde{V}^{\text{FFT}}(\kappa)$  is computed by the rigorous fast Fourier transform technique and  $\tilde{V}^{\text{HFT}}(\kappa)$  denotes the result obtained by the homeomorphic Fourier transform. For each case, the deviation between the two approaches is presented in Tab. 6. The deviation exhibits initially high values at the low-NA which rapidly drop as the NA increases, with an asymptotic tendency as the NA continues to increase even further. That is, when the smooth wavefront phase term is strong enough to dominate the Fourier transform, the HFT will yield a result that is in practice indistinguishable from that of the rigorous FFT integral.

The investigation of the behavior of the fast Fourier transform and the homeomorphic Fourier transform with respect to the significance of the smooth wavefront (of which a spherically shaped one is just one example) for a given field distribution illustrates, is the effect of the stationary phase condition on the Fourier transform. In other words, when the aforementioned smooth wavefront is strong enough, the stationary phase assumption will be fulfilled and the Fourier trans-

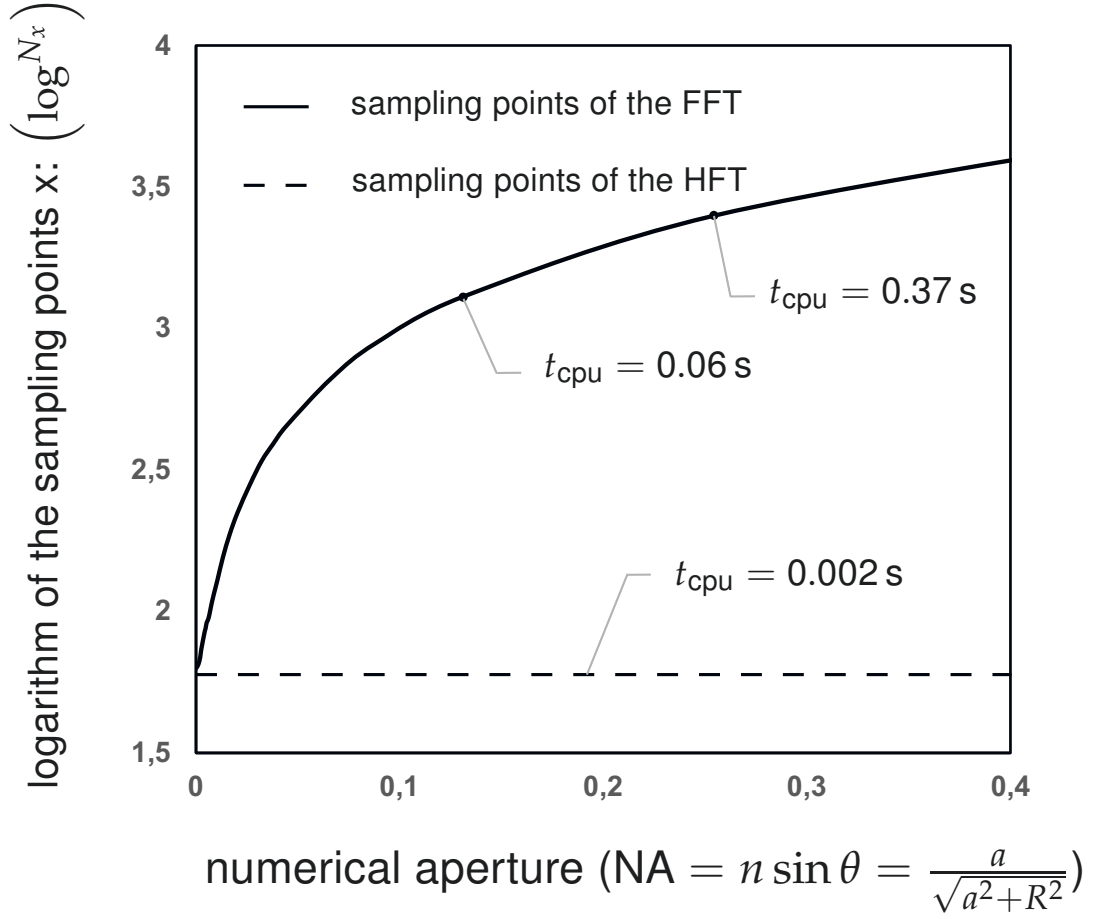


Figure 11: Comparison of the numerical effort of the homeomorphic and the Fast Fourier transforms (HFT and FFT respectively, for short) for the case of a house-shaped field with a spherical phase, for different values of the numerical aperture (NA) of said spherical phase. The abscissa records increasing values of the NA, which correspond to decreasing values of the radius of curvature  $R$  of the spherical phase. The ordinate corresponds to a logarithmic scale of the number of sampling points. The dashed line for the number of sampling points used to sample the function in the case of the HFT operation, and, the solid line for the number of sampling points necessitated by the computation of the FFT. Finally, the CPU time at two specific positions, where  $R = 10 \text{ mm}$  and  $R = 5 \text{ mm}$ , are pointed out.

form will cease to exhibit an integral behavior, and effect a mere homeomorphism between the space and the spatial frequency domains: when this is true, the substitution of the (albeit strictly speaking approximated) homeomorphic Fourier transform – as presented in Section 3.1.1 – for the rigorous Fourier integral will be justified.

Let us at this point retrieve another dimension of the discussion which was already mentioned in the previous section: numerical effort. When, in Section 3.1.1, we presented the theoretical derivation of the homeomorphic Fourier transform, we indicated how using a hybrid sampling strategy for a field given in the form of Eq. 44 could effectively massively reduce the sampling effort compared against an indiscriminate Nyquist sampling of the entire field, including the  $2\pi$ -wrapped wavefront phase. In the following experiment we seek to compare the numerical effort of computing the Fast Fourier Transform (FFT) against that required to calculate the corresponding homeomorphic Fourier transform (HFT) of the same function. Even though the number of sampling points has been given in Tab. 6, for better visualization of the results and gauging of conclusions, we have plotted in Fig. 11 the numerical effort of the FFT and of the HFT in terms of the number of sampling points as function of the numerical aperture (NA).

The graphs in Fig. 11 and Tab. 6 reveal that, as the numerical aperture increases as  $R$  decreases, there is a steep rise in the number of sampling points required by the sampling conditions of the FFT operation. In the case of the HFT, however, the number of necessary sampling points remains constant with increasing NA. This is due to the fact that the residual field  $U$  and the smooth phase  $\psi$  are sampled separately, following the aforementioned hybrid sampling strategy. How many samples it is necessary to handle in order to compute the HFT of a given function depends on which of the two terms demands a larger sampling number; in the particular case considered here, taking into account the fact that the smooth phase is a simple spherical phase, and sampling the residual field  $U(\rho)$  necessitates resolving all the details in the house-shaped aperture, the sampling heft of the latter clearly trumps that of the former. Finally, to clarify the performance of the HFT in practical tasks, we record the CPU time at two specific positions for both FFT and HFT, shown in Fig. 11. It reveals that the small number of sampling points translates into a short computational time.

HFT does contribute to reduce the numerical complexity and could have broad application prospects.

### 3.2.2 Fourier transform of a field with a simple aberrant phase

In the field of optical system design, the aberration theory plays the most important role and has a long and prominent history. Among other things, it is used to characterize the shape of wavefront phases, usually as a means of identifying and quantifying in what way and how much that phase differs from a certain reference. There are various alternatives to describe aberration. In this work, we select one of the most often encountered representations is that provided by the set of Zernike polynomials.

In last example, we discuss the Fourier transform of the field with an ideal spherical phase. So, in the second set of experiments, we intend to investigate a more common situation that is the influence of the aberrant phases on the Fourier transform. We selected a similar optical setup as the one used in the last work: an ideal plane wave is truncated by an aperture shaped as a sequence of letters spelling “Light”, after which aperture an aberrant phase is superimposed on the field. In this case, as shown in Fig. 12 (a), the amplitude distribution will remain unchanged throughout the sequence of experiments.

In the following set of experiments, we will vary the Zernike polynomial terms imposed on the field and study the effect of different types of aberrations on the Fourier transform. The smooth wavefront phase in the test can be mathematically described by means of its Zernike decomposition:

$$\psi(\rho) = \psi^{\text{zer}}(\rho) = k \sum_{m=0}^M \sum_{n=0}^N c_n^m Z_n^m(r, \theta), \quad (66)$$

where  $k = \frac{2\pi}{\lambda} \tilde{n}$ ,  $\lambda$  being the wavelength,  $r = \frac{|\rho|}{|\rho_{\max}|}$  and  $\theta = \arctan\left(\frac{y}{x}\right)$ ;  $c_n^m$  denotes the coefficients of the corresponding Zernike term. For the experiment, we have selected six types of lower-order Zernike phases, which we enumerate and express in Table 7. They all have the mathematical characteristic of being quadratic polynomial terms so that the resulting mapping relation  $\rho \rightarrow \kappa : \nabla_{\perp} \psi(\rho) = \kappa$  is an exactly linear transformation.



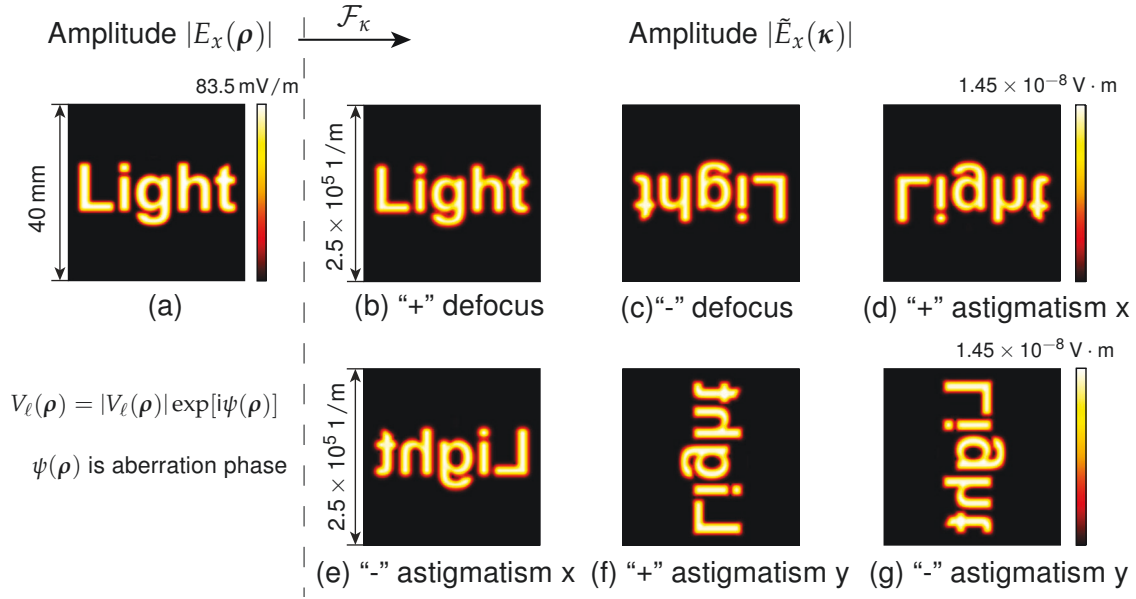


Figure 12: Homeomorphic Fourier tranform (FFT results are not shown, since deviation between HFT and FFT just 0.2%) of a field with amplitude shaped in the form of a letter sequence spelling “Light”, in the cases of different aberrant phases. Panel (a) shows the amplitude distribution of the  $E_x$  component in the space domain, common starting point to all results. Different aberrations are then superimposed on this amplitude, and its Fourier transform computed. The remaining panels present the  $\tilde{E}_x$  component (i.e. the result of said Fourier-transform operation) for (b) positive defocus, (c) negative defocus, (d) positive astigmatism  $x$ , (e) negative astigmatism  $x$ , (f) positive astigmatism  $y$  and (g) negative astigmatism  $y$ .

Table 7: Simulation parameters of the aberrant phase for the example presented in Section 3.2.2.

No.	name & type	expression (Zernike)	value
Fig. 12 (b)	defocus	$Z_2^0 = \sqrt{3} (2r^2 - 1)$	$c_2^0 = 100\lambda$
Fig. 12 (c)	defocus	$Z_2^0 = \sqrt{3} (2r^2 - 1)$	$c_2^0 = -100\lambda$
Fig. 12 (d)	vertical astigmatism	$Z_2^{-2} = \sqrt{6}r^2 \cos 2\theta$	$c_2^{-2} = 200\lambda$
Fig. 12 (e)	vertical astigmatism	$Z_2^{-2} = \sqrt{6}r^2 \cos 2\theta$	$c_2^{-2} = -200\lambda$
Fig. 12 (f)	oblique astigmatism	$Z_2^2 = \sqrt{6}r^2 \sin 2\theta$	$c_2^2 = 200\lambda$
Fig. 12 (g)	oblique astigmatism	$Z_2^2 = \sqrt{6}r^2 \sin 2\theta$	$c_2^2 = -200\lambda$



In Fig. 12, the result of the Fourier transform for different lower-order aberrations is presented. It must be emphasized that all the results presented in Fig. 12 are computed by the rigorous FFT. From Table 7, we know that the scaling factors for different aberrations are all larger than hundreds of the wavelength. It means that, as before, the smooth wavefront phase term is strong enough to dominate the Fourier transform. Therefore, for all the cases, the homeomorphic Fourier transform is employed for the comparison and would produce virtually the same results as the rigorous FFT, with  $\sim 0.2\%$  deviation when compared against the FFT reference. One can see that, regardless of the scaling, the Fourier-transform operation delivers either a rotation or a mirroring of the original pattern. Additionally, we discussed the appearance of distortion in the mapping in the case of the spherical phase, but it is worth mentioning that no such effect arises for the aberrations considered in this experiment. This is related to the fact, already pointed out above, that all the aberration terms we have selected produce a linear mapping relation between  $\rho$  and  $\kappa$ , and the fact that the scaling factor for the selected Zernike polynomials is symmetric for both the  $x$  and  $y$  dimensions.

### 3.2.3 *Fourier transform of a field with a general, bijective, wavefront phase*

The application of the homeomorphic Fourier transform to fields exhibiting spherical phases or simple aberrant phases has been demonstrated respectively and in isolation in the previous two sections with the help of two typical instances. In the third experiment, we would like to extend the case study to a more general optical scene. For this purpose, we build up a simple optical system: a spherical wave is truncated by a circular aperture with radius  $a = 12$  mm; at the plane where the aperture is located the spherical phase has a radius of curvature of  $R = 6$  mm or, in other words, the distance from the point source to the plane of the aperture is 6 mm. Then, a Zernike phase plate places directly behind the aperture mask. In what follows, we shall detect and compare the Fourier transform of the field with different Zernike aberrations obtaining by this system.

Table 8: Simulation parameters of the aberrant phase for the example in Section 3.2.3.

No.	name & type	expression (Zernike)	value
Fig. 13 (c)	trefoil $x$	$Z_3^3 = \sqrt{8}r^3 \cos 3\theta$	$c_3^3 = 300\lambda$
Fig. 13 (d)	coma $x$	$Z_3^1 = \sqrt{8}(3r^3 - 2r) \cos \theta$	$c_3^1 = 100\lambda$
Fig. 13 (f)	tetrafoil $y$	$Z_4^{-4} = \sqrt{10}r^4 \sin 4\theta$	$c_4^{-4} = 150\lambda$
Fig. 13 (g)	tertiary astigmatism $y$	$Z_6^{-2} = (15r^6 - 20r^4 + 6r^2) \sin 2\theta$	$c_2^{-2} = 40\lambda$
Fig. 13 (i)	pentafoil $x$	$Z_5^5 = \sqrt{12}r^5 \cos 5\theta$	$c_5^5 = 150\lambda$
Fig. 13 (j)	tertiary spherical	$Z_8^0 = \sqrt{9}(70r^8 - 140r^6 + 90r^4 - 20r^2 + 1)$	$c_8^0 = 30\lambda$

The amplitude of the field directly behind the mask is presented in Fig. 13 (a). The numerical aperture can be computed by the formula  $NA = \frac{an}{\sqrt{a^2 + R^2}} = 0.3$ , a value for which the HFT proves sufficiently accurate. The Fourier transform of the initial field – i.e. with only spherical phase – is given in Fig. 13 (b) which, in accordance with what we already know about the behavior of fields for which the HFT is an accurate choice, exhibits a very similar distribution to the original pattern of the field in the space domain. This case will serve as a reference for the following tests, where we will add different Zernike terms onto the initial spherical phase and observe their influence on the Fourier transform. We have selected six types of complex aberrant phases, so that one or a combination of several of them can be added to the starting-point case of a purely spherical phase.

We organize further experiments as follow: we have added the selected six types of complex aberrant phases, respectively and in isolation, to the purely spherical phase. The Fourier-transform results for the cases where a single higher-order Zernike phase term has been added to the initial field, are presented at the second and third columns in Fig. 13.

Afterward, we added the combination of two kinds of aberrations to the initial field. The fourth column corresponds to the Fourier transform of the same initial field, but this time the superimposed aberration term is a combination of the higher-order terms employed in the same row in columns two and three, so that the effect of both can be observed at the same time and in a combined manner. The specific simulation parameters can be consulted in Table 8. Fig. 13 illustrates

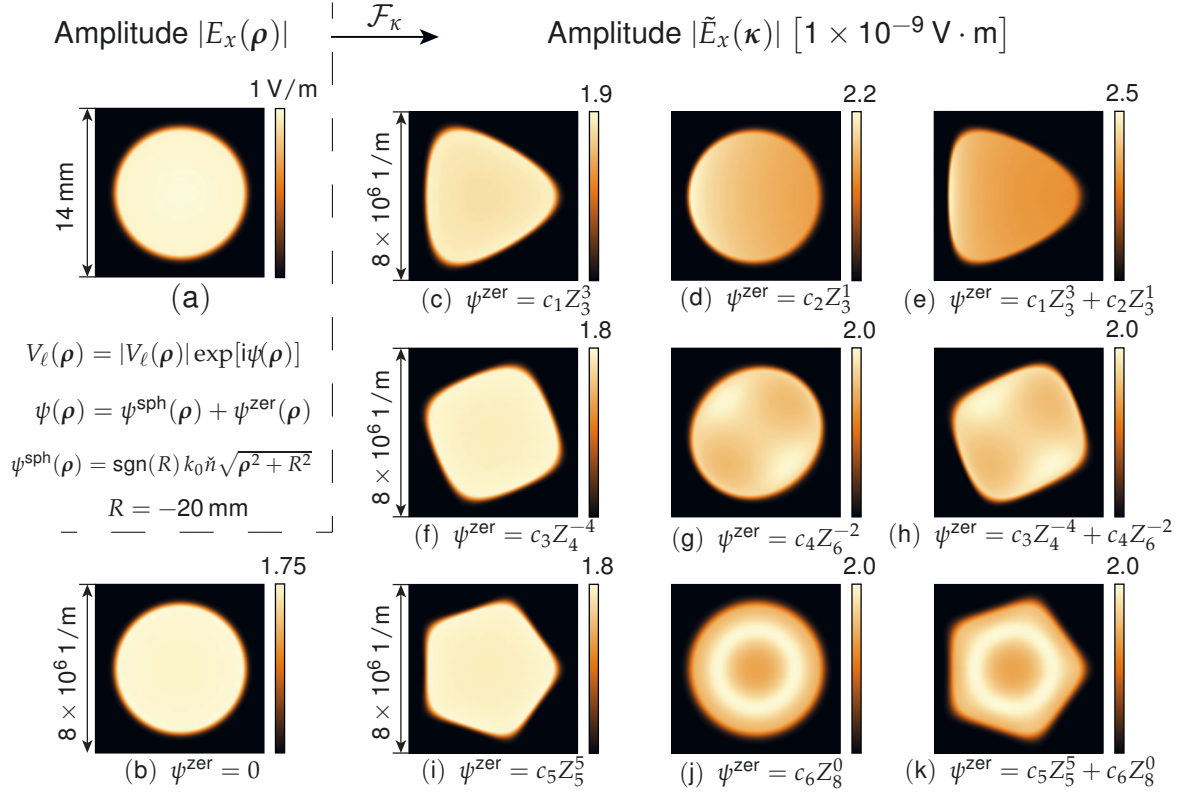


Figure 13: Homeomorphic Fourier transform (HFT results are not shown, since deviation between HFT and FFT just 0.2 %) of a field with a general bijective wavefront phase. Panel (a) should the amplitude distribution of the  $E_x$  component in the space domain, common starting point to all results. A spherical wavefront with different aberrations is then superimposed on this amplitude, and the Fourier transform computed. The remaining panels present the  $\tilde{E}_x$  component (i.e. the result of said Fourier-transform operation) for (b) a purely spherical phase, (c) spherical phase and trefoil  $x$ , (d) spherical phase and coma  $x$ , (e) spherical phase, trefoil  $x$  and coma  $x$ , (f) spherical phase and tetrafoil  $y$ , (g) spherical phase and tertiary astigmatism  $y$ , (h) spherical phase, tetrafoil  $y$  and tertiary astigmatism  $y$ , (i) spherical phase and pentafoil  $x$ , (j) spherical phase and tertiary spherical, and (k) spherical phase, pentafoil  $x$  and tertiary spherical. The corresponding Zernike terms are indicated under each panel.

how the inclusion of different aberration terms and combinations thereof modify and reshape the pattern and amplitude distribution of the spectrum.

It is important to note that for all the examples presented in this set of experiments the result of performing the Fourier transform with the homeomorphic operation was always compared against that obtained with the rigorous FFT algorithm. The deviation remained bounded throughout at under 0.2 %. A direct implication of this is that the homeomorphic Fourier transform algorithm can be applied to fields with *any* wavefront phase, as long as it sustains the bijectivity condition. In other words, there is no additional restriction on the type or shape of the wavefront phase, apart from the requirement for a bijective mapping.

#### 3.2.4 *Fourier transform of a field with a non-bijective wavefront phase*

Up to this point, we have only discussed those cases where the wavefront phase of the test field produced a bijective mapping when subjected to the algorithm of the HFT. Last but not least, we would like to delve into the pragmatically quite interesting case of how to extend the application of the HFT to situations in which the given wavefront phase violates the bijectivity condition. The basic workflow of how to go about this task numerically was already outlined in Section 3.1.4. Here let us focus on two specific, tangible instances of its application.

We take as the starting point for the first experiment, a field linearly polarized along  $E_x$  with a slowly varying amplitude, as shown in Fig. 14 (a). Its smooth wavefront phase is shown, numerically sampled, in Fig. 15 (a). In this example, we employ the hybrid sampling strategy, and we assume there is no extra phase information besides the smooth wavefront phase.

The next step, rather than straight away attempting to apply the HFT, is to examine whether the homeomorphism condition is fulfilled by the wavefront phase of the field in question. The mathematical criterion to establish or disprove this conformity rests on the sign of the second derivatives of the wavefront in the entire definition domain of the field: if the sign does not change, then the condition holds, the mapping relation can be obtained, and the HFT computed. If, on the other hand, the sign changes from positive to negative (or vice versa)

Table 9: Simulation parameters of the aberrant phase for the first example in Section 3.2.4.

name & type	fitting expression	coefficients	$\psi^{\text{map}}(\rho)$
spherical phase	$\psi^{\text{sph}} = \text{sign}(R) k_0 \tilde{n} \sqrt{\rho^2 + R^2}$	$R = 9.1 \text{ mm}$	✓
piston	$Z_0^0 = 1$	$c_0^0 = 0.88\lambda$	✓
tilt $y$	$Z_1^{-1} = 2r \sin \theta$	$c_1^{-1} = -2.52\lambda$	✓
tilt $x$	$Z_1^1 = 2r \cos \theta$	$c_1^1 = -1.17\lambda$	✓
defocus	$Z_2^0 = \sqrt{3} (2\rho^2 - 1)$	$c_2^0 = -1.97\lambda$	✓
astigmatism $x$	$Z_2^2 = \sqrt{6} r^2 \cos 2\theta$	$c_2^2 = 27.6\lambda$	✓
trefoil $y$	$Z_3^{-3} = \sqrt{8} r^3 \sin 3\theta$	$c_3^{-3} = 6.14\lambda$	✓
coma $y$	$Z_3^{-1} = \sqrt{8} (3r^3 - 2r) \sin \theta$	$c_3^{-1} = 4.5\lambda$	✓
coma $x$	$Z_3^1 = \sqrt{8} (3r^3 - 2r) \cos \theta$	$c_3^1 = 6\lambda$	✓
trefoil $x$	$Z_3^3 = \sqrt{8} r^3 \cos 3\theta$	$c_3^3 = 3.84\lambda$	✓
tetrafoil $y$	$Z_4^{-4} = \sqrt{10} r^4 \sin 4\theta$	$c_4^{-4} = -3.53\lambda$	✓
spherical aberration	$Z_4^0 = \sqrt{5} (6r^4 - 6r^2 + 1)$	$c_4^0 = 0.001\lambda$	✓
secondary astigmatism $x$	$Z_4^2 = \sqrt{10} (4r^4 - 4r^2) \cos 2\theta$	$c_4^2 = 0.15\lambda$	✗

at any point in the definition domain, the homeomorphism condition is violated, and further measures need to be taken before the HFT algorithm can be applied.

This takes us to the practicalities of calculating, numerically, the point-wise second derivatives of the wavefront. There are several methods to attain this end, which can depend on the initial parametrization of the three-dimensional surface in question. For instance, a spline interpolation can provide the local gradient information. In this example, however, we choose to follow the proposed method of first performing a fitting for the linear phase, spherical phase, and any additional Zernike terms, in that order, starting from the initial numerical phase data. We consequently obtain an analytical expression,  $\psi^{\text{fit}}(\rho)$ , for the phase. For the specific case at hand, the result of this fit (expression and coefficients for the different terms) is presented in Table 9.

An analysis of the quality of the fit can be extracted from Fig. 15 (b), where we show the subtraction of the smooth, analytic function produced by the fit,

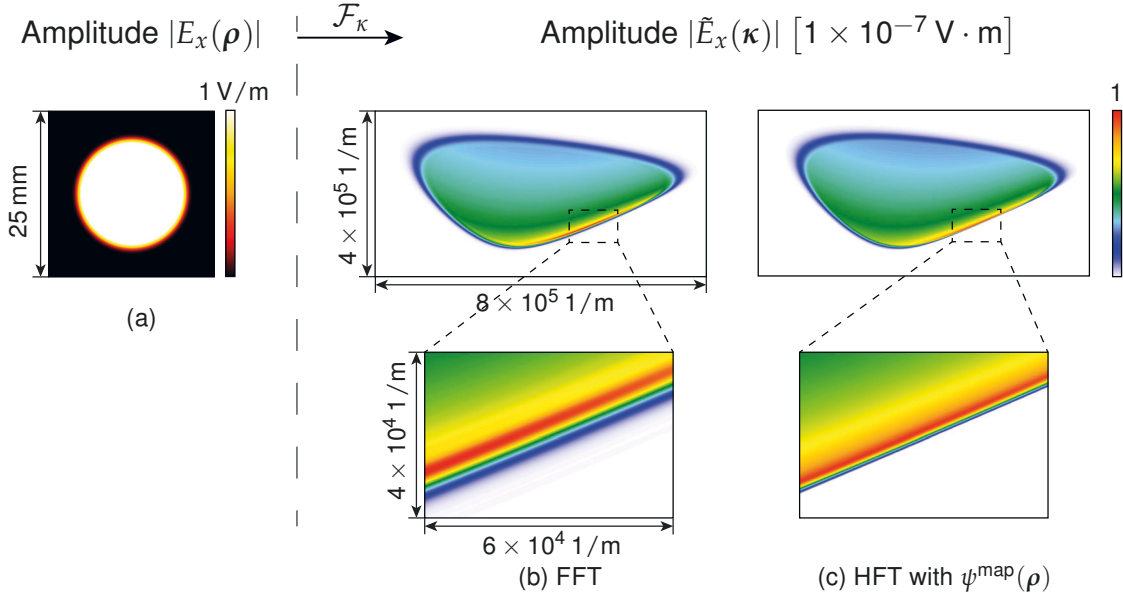


Figure 14: Fourier transform of a field with a non-bijective wavefront phase. Panel (a) shows the amplitude of the  $E_x$  component in the space domain, panel (b) shows the result of the Fourier transform as obtained via the rigorous Fast Fourier Transform, and panel (c) shows the result of the Fourier transform as per the approximation provided by the homeomorphic Fourier transform with bijective regularization of the mapping relation.

$\psi^{\text{fit}}(\rho)$ , from the initial, discretely sampled phase  $\psi(\rho)$ . Direct comparison of the scale used here ( $\sim 3 \times 10^{-6}$  rad) and that used for the initial phase in panel (a),  $\sim 970$  rad, confirms the accuracy of the fit. Let us now calculate the second derivatives of  $\psi^{\text{fit}}(\rho)$  in a point-wise manner; the sign of the result is graphically shown, color-coded, in Fig. 15 (e): while over most of the definition domain the second derivatives exhibit a positive sign, a small area in the bottom right is negative-valued. The homeomorphism condition is thus infringed, and the wavefront phase must be regularized before moving on with the computation of the homeomorphic Fourier transform.

We follow the elementary optimization approach presented in Section 3.1.4, whereby the highest Zernike term present in the fit will be successively removed from the wavefront part of the phase and the homeomorphism condition re-examined until it is fulfilled. In the specific example studied here, only one iteration is necessary, and it suffices to remove the secondary astigmatism in

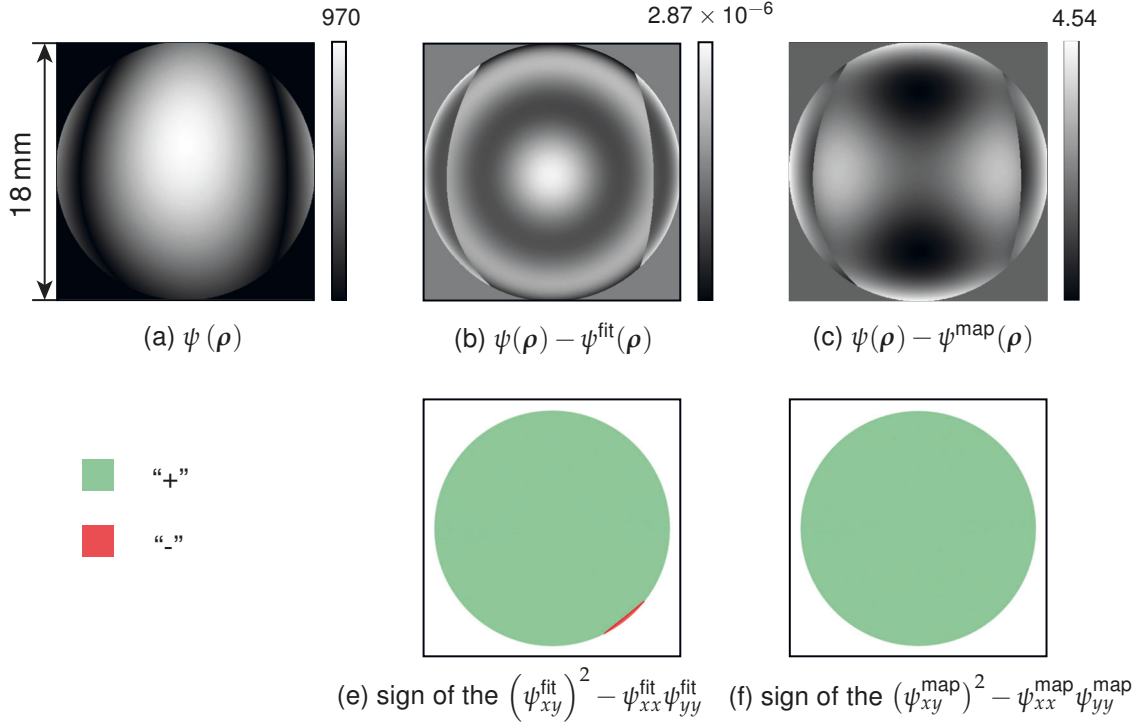


Figure 15: Analysis of the wavefront phase for the simulation task: Homeomorphic Fourier transform of a field with a non-bijective wavefront phase. Panel (a) shows the initial smooth phase, panel (b) the residual phase after performing the fitting, panel (c) the phase from which the bijective mapping will be obtained, panel (e) serves to examine the homeomorphism condition for the fitted phase (the violation of the condition is evident from the change in sign of the second derivatives) and panel (f), analogously to (e), serves to examine how the same condition is fulfilled in the case of the final regularized phase employed to compute the bijective mapping.

$x$ , leaving us with the final expression for the wavefront to be employed in the computation of the HFT,  $\psi^{\text{map}}$ , which fulfills the homeomorphism condition, as shown in panels (c) and (f) of Fig. 15.

We are finally in a situation to compute the now bijective mapping relation  $\rho \rightarrow \kappa^{\text{map}}$  from the regularized wavefront phase  $\psi^{\text{map}}$ , according to Eq. (47). Please note that the remainder of the phase after the part which can provide us with a bijective mapping has been extracted is not lost in the calculation of the HFT: the expression of the total field  $V_\ell(\rho)$  will be reorganized, according to Eq. (44), so that this remainder of the phase will be henceforth included in



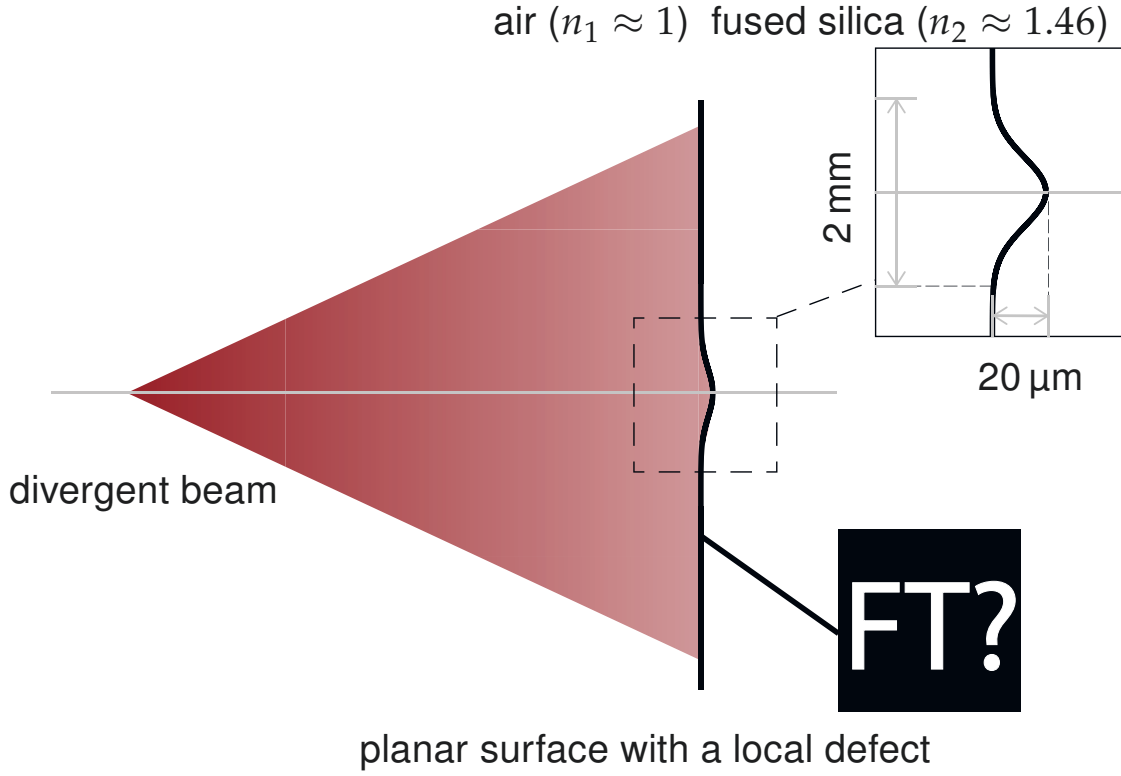


Figure 16: Sketch of the simulation setup: divergent beam incidents a surface with some local defect. There is a local defect in the central area of a planar surface. The local defect distributes smoothly and has a Gaussian profile. The local plane interface approximation (LPIA) is applied to deal with the light field going through the curved surface. Then, the HFT and regular FFT are respectively used to calculate the spectrum for the field behind the surface.

the  $U(\rho)$  term. The only effect of this regularization of the wavefront phase is on the mapping relation. Once the mapping is obtained, we can finally perform the HFT operation on the test field. Panels (b) and (c) of Fig. 14 show the results of performing the FFT and HFT respectively on said test field. Visually, the similarity between them is evident, with some small differences appearing in the bottom right (tellingly, the same area where the violation of the homeomorphism condition arose). The deviation of the HFT with respect to the FFT reference is about 1 %.

In the first experiment, we correctly use the proposed elementary optimization strategy to distinguish the bijective mapping phase and the higher-order



Zernike aberration phases. The simulation result reveals the vast potential of this approximated pointwise operation. However, we must admit that the first example is an extraordinary case that the aberration phase with a very low weight coefficient precisely causes non-homeomorphism. In practice, more general situations are that some local defects on the wavefront conduct non-homeomorphism. Therefore, we prepare another experiment to present the application of this robust algorithm to a more practical optical setup.

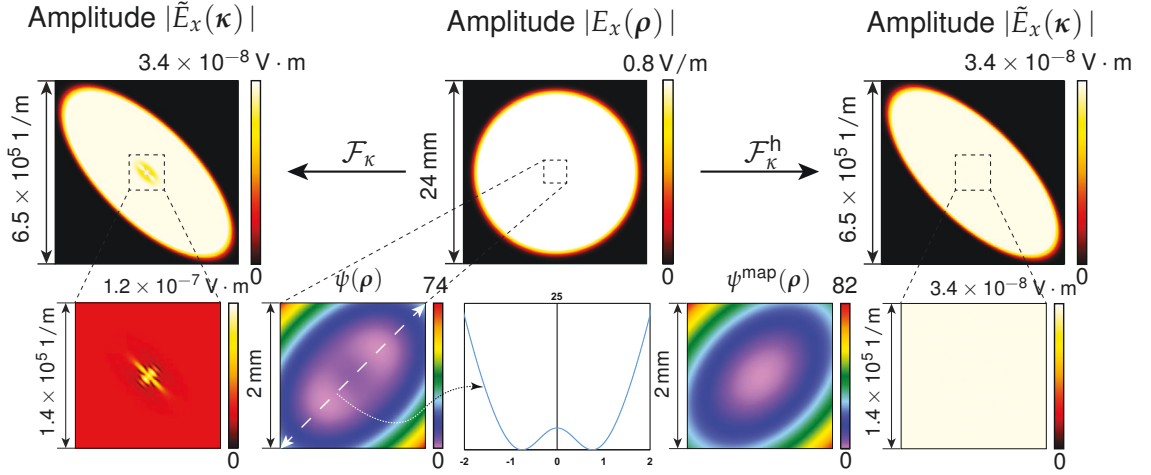


Figure 17: Fourier transform of a field with a non-bijective wavefront phase. The left picture shows the result of the Fourier transform as obtained via the rigorous Fast Fourier Transform. The middle picture is the amplitude of the transmitted field directly behind the interface. And, the right picture shows the result of the Fourier transform as per the approximation provided by the homeomorphic Fourier transform with bijective regularization of the mapping relation.

As depicted in Fig. 16, we build up the simulation setup for the second experiment. The incident field used in the simulation is a linearly  $E_x$  polarized divergent beam in the standard air, with a wavelength of 532 nm. Importantly, its wavefront phase is purely quadratic phases. In front of the interface, we measured the beam parameter and wavefront phase parameter for the incident field. Consequently, we know the diameter of the field in front of the surface is  $(20 \text{ mm} \times 20 \text{ mm})$ , and the wavefront phase at this position consists of the defocus phase and astigmatism  $y$ , shown in Table 17. The transmission medium

Table 10: Wavefront phase parameters of the incident field in front of the interface for the second example in Section 3.2.4.

name & type	expression	value
defocus	$Z_2^0 = \sqrt{3} (2\rho^2 - 1)$	$c_2^0 = 150\lambda$
astigmatism $x$	$Z_2^{-2} = \sqrt{6}r^2 \sin 2\theta$	$c_2^{-2} = -120\lambda$

behind the interface is fused silica, whose refractive index is  $n_2 \approx 1.46$ . The interface between two mediums is a planar surface with some local defects in the central area. In Fig. 16, by zooming in the local defect region, we can see that the defect has a Gaussian profile with a size of  $(2\text{ mm} \times 2\text{ mm})$ , which is much smaller than the beam size of the incident field.

We perform the local plane interface approximation (LPIA) to carry out the light field passing through the curved surface. The amplitude distribution of the transmitted field is shown in Fig. 17. It should be noted that the planar interface won't change the homeomorphism condition of the wavefront phase. As we mentioned, the incident wavefront phase is simply in the form of quadratic polynomials. The resulting wavefront phase behind the planar interface must still be quadratic and bijective. The elementary optimization strategy can precisely found this bijective transmitted wavefront phase, presented in Fig. 17. On the other hand, due to the introduction of the local defect, the transmitted wavefront phase is modulated in the defect region and becomes non-bijective. The real transmitted wavefront phase and the corresponding 1D cut are shown in Fig. 17.

As can be seen in Fig. 17, the PFT with regularized bijective phase and the regular FFT are respectively applied to calculate the Fourier transform of the transmitted field, and the simulation results are displayed on the same scale. First of all, we investigate the accuracy of the proposed PFT approach compared to the FFT reference. The deviation between the two methods is under 3%. This number looks not a significant difference. However, in the central area, we can observe a noticeable difference in the resulting pattern. When we zoom in the central area of the FFT spectrum pattern, we can see evident interference fringes. Meanwhile, HFT presents a sufficiently uniform distribution in the same area. Last but not least, we would like to note that besides the local defect region, the

resulting fields by both approaches are the same. This fact is different from the first example. It is because that the Zernike phases are global polynomials and having an effect on the full definition domain.

The closer look at the area of interest which is also presented in the figure reveals that the differences between the PFT and the FFT results stem from what could be described as a “diffraction-like” pattern in the FFT which is absent in the HFT case. This observation in the purely mathematical perspective we have maintained throughout this work could be obviated; however, when looking to apply the mathematical tool that is the HFT in an optics context this detail will prove immensely relevant: one of the main effects (if not *the* main effect) of employing the HFT in the simulation of an optical system is that it will neglect any diffraction effects which might be relevant at the plane where it is performed.



## APPLICATION IN THE FREE SPACE PROPAGATION

The physical-optics modeling means the ability to solve Maxwell's equations on the system level. Instead of employing a universal Maxwell solver for the whole system, we follow the concept of field tracing, i.e., to decompose the system into regions and apply various regional Maxwell solvers. The field solvers can be evaluated in either a rigorous manner or with certain mathematical approximations. And, they may work in different domains, e.g., the spatial ( $x$ ) or the spatial frequency ( $k$ ) domain [61, 98, 99]. Then, by matching the boundary values amongst regions, these regional solvers can be connected to complete the system. As we mentioned, to use different field solvers in connection, so as to enable the modeling of sophisticated systems, the Fourier transform is a crucial technology and frequently used. In the previous two chapters, we proposed two advanced Fourier transform techniques, i.e., the semi-analytical Fourier transform and the homeomorphic Fourier transform. Counting also the fast Fourier transform, we have three numerical tools in total to carry out the transforming between the  $x$ -domain and the  $k$ -domain. Motivated by both fundamental aspects and practical applications [100, 101], we would demonstrate how to achieve fast physical optics modeling and design with the help of the proposed innovative Fourier transform techniques. Instead of some complicated systems, as the starting point of the investigation, we are concentrating on the most fundamental but indispensable problem in optical modeling, i.e., the light field propagation within a homogeneous and isotropic media.

For the free space propagation, rigorous Maxwell's solutions have been found both in the spatial domain ( $x$ -domain) and the spatial-frequency domain ( $k$ -domain), namely the Rayleigh-Sommerfeld diffraction integral and the method of angular-spectrum-of-plane-waves (SPW). However, due to the complexity of the integral operation, both rigorous approaches suffer from severe numerical issues. Various approximate propagation methods are providing to overcome the drawback of the rigorous techniques. For example, in 1909, Debye published his

work to demonstrate the general features of a diffracted field near its focus [66, 102]. When comparing the Debye and the rigorous Rayleigh-Sommerfeld integrals, we can see how the Debye approximation reduces a double integral to a single one. Furthermore, In the numerical implementation of this single integral, the required sampling points are far fewer. Although the approximate approaches can provide a considerable reduction in the computational effort, the limited applicable scopes much restrict their usage in practical simulation. In short, it is urgent and vital to find a unified free space propagation operator, which has the advantages of both rigorous and approximate approaches.

#### 4.1 UNIFIED FREE SPACE PROPAGATION OPERATOR VIA THE K-DOMAIN

In physical optical modeling and design, the propagation of light fields from the source plane to the target plane in free space (where, by “free space”, we understand any isotropic and homogeneous medium) is either a fundamental or essential scenario. The corresponding techniques can be used in various applications, e.g., lens system, holographic microscopy and diffractive optics [103–105]. Thus, we would like to consider an arbitrary harmonic field defined in a plane and demonstrate how to propagate this field in free space. First of all, let us build up a Cartesian coordinate system  $X - Y - Z$  and assume the principal propagation direction and the optical axis along the  $+z$ -axis. Here,  $z = z_0$  is the axis position of the plane where we investigate the input light field. At this plane, the input field is known at the given transversal position vector  $\boldsymbol{\rho} = \mathbf{r}_\perp = (x, y)$ , with  $V_\ell(\boldsymbol{\rho}, z_0)$ . Then, the output field at the target plane  $z = z' = z_0 + \Delta z$  can be formulated by

$$V_\ell(\boldsymbol{\rho}', z') = \mathcal{P}V_\ell(\boldsymbol{\rho}, z_0) \quad (67)$$

where  $\mathcal{P}$  indicates the free space propagation operator and  $\boldsymbol{\rho}' = (x', y')$  represents the transversal position vector on the target plane.

As we mentioned, one well-known rigorous free space propagation operator is the Rayleigh-Sommerfeld diffraction (RSD), which is a two-dimensional complex-valued integral in the spatial domain. Since, in most practical situations, there is no analytical solution for this integral operation, it presents a numerical complexity of  $\mathcal{O}(N^2)$  for a function with  $N$  samples. With the help of the

Fourier transform integral, Eamon Lalor proposed another rigorous approach in the  $k$ -domain, namely the method of angular-spectrum-of-plane-waves (SPW). He demonstrated the equivalence of SPW operator and RSD integral theoretically. From the implementation point of view, the computational effort of the SPW operator can be reduced from  $\mathcal{O}(N^2)$  to  $\mathcal{O}(N \log N)$  by the fast Fourier transform (FFT). But, in the case of an intensive wavefront phase, the required sampling points  $N$  are massive to resolving the “ $2\pi$ -modulo” phase. In what follows, by employing the novel Fourier transform techniques as well as the extension for the propagation to inclined planes, we present the derivation and fundamental strategies of the unified free space propagation operator.

#### 4.1.1 Propagation operator between parallel planes

It is well known that general fields can be described as a superposition of plane waves presenting different propagation directions. By performing the Fourier transformation, we can achieve the shift from the spatial domain to the spatial frequency domain and vice versa. In the  $k$ -domain, each spatial frequency indicates an ideal plane wave whose physical response of the propagation follows the plane wave ansatz. We can refer to this response as the  $k$ -domain propagation operator and denote it by  $\tilde{\mathcal{P}}$ . Using the knowledge we have of ideal plane waves, the propagation kernel (between two parallel planes) in the  $k$ -domain is simply a pointwise operation, i.e., multiplying an exponential phase term

$$\tilde{\mathcal{P}} := \exp \left[ i\check{k}_z(\boldsymbol{\kappa}) \Delta z \right] = \exp \left( i \sqrt{k_0^2 \check{n}^2 - k_x^2 - k_y^2} \Delta z \right), \quad (68)$$

where  $\Delta z = z' - z_0$  is the propagating distance,  $\check{n}$  is the complex refractive index of the embedding medium and  $k_0 = \frac{2\pi}{\lambda}$  denotes the wavenumber of the harmonic field.

Combining forward and backward Fourier transform integrals, we can write down the compact mathematical expression of the angular-spectrum-of-plane-waves (SPW) operator,

$$V_\ell(\boldsymbol{\rho}', z') = \mathcal{F}_\kappa^{-1} \left\{ \mathcal{F}_\kappa[V_\ell(\boldsymbol{\rho}, z_0)] \times \exp \left[ i\check{k}_z(\boldsymbol{\kappa}) \Delta z \right] \right\}. \quad (69)$$

where  $\mathcal{F}_\kappa$  and  $\mathcal{F}_\kappa^{-1}$  denote the (inverse) Fourier transform integral operations.

The SPW formula reveals that the universal propagation operator via the  $k$ -domain is merely a sequence of two Fourier transform integrals together with a pointwise operation in the  $k$ -domain. Generally, employing the FFT and the IFFT in the numerical implementation enables a fast evaluation of the SPW operator that reduces the computational effort to  $\mathcal{O}(N \log N)$  where  $N = N_x \times N_y$  is the number of required sampling points for a given complex function. However, because of the periodic nature of the complex exponential function, i.e., the need to sample the exponential phase term  $\exp[i\psi(\boldsymbol{\rho})] = \cos[i\psi(\boldsymbol{\rho})] + i \sin[i\psi(\boldsymbol{\rho})]$ , the " $2\pi$ -wrapped" phase becomes jaggedly discontinuous. Furthermore, due to the phase modulation  $\exp[i\tilde{k}_z(\boldsymbol{\kappa}) \Delta z]$  in the  $k$ -domain, the forward FFT and backward IFFT usually are confronted with precisely different sampling issues. To sum up, as a matter of numerical difficulty, the SPW operator using only FFT cannot be a general solution to the problem of free space propagation.

Besides, the formula, expressed in Eq. (69), only holds in the problem of propagation between two parallel planes. However, propagating the light field to an inclined plane is of importance in optical modeling and design and also a fantastic subject of interest. In the coming two sections, we would demonstrate how to overcome the numerical issue in the Fourier transforms and enable the calculation of light propagation between non-parallel planes.

#### 4.1.2 Extension to the arbitrarily oriented planes

A rigorous physical-optics approach to solve the problem of field propagation between non-parallel planes has been presented by Zhang et al. [65]. The only difference in the derivation is the replacement of the propagation step in the  $k$ -domain, which is now denoted by  $\tilde{\mathcal{P}}$  as shown in Fig. 18. This step can be completely described in a pointwise manner. Without showing all derivations in detail, the connection between input and output field values can be summarized as

$$\tilde{V}_{\perp}^{\text{out}}(\boldsymbol{\kappa}^{\text{out}}, z^{\text{out}}) = \tilde{\mathcal{P}}[\boldsymbol{\kappa}^{\text{out}}(\boldsymbol{\kappa})] \tilde{V}_{\perp}(\boldsymbol{\kappa}, z_0), \quad (70)$$



with

$$\begin{aligned}\tilde{\mathcal{P}}[\kappa^{\text{out}}(\kappa)] &= \tilde{a}[\kappa^{\text{out}}(\kappa)] \tilde{\mathcal{B}}[\kappa^{\text{out}}(\kappa)] \tilde{\mathcal{M}}[\kappa^{\text{out}}(\kappa)] \\ &= \begin{bmatrix} \tilde{a} & 0 \\ 0 & \tilde{a} \end{bmatrix} \begin{bmatrix} \tilde{B} & 0 \\ 0 & \tilde{B} \end{bmatrix} \begin{bmatrix} \tilde{M}_{k_x k_x} & \tilde{M}_{k_x k_y} \\ \tilde{M}_{k_y k_x} & \tilde{M}_{k_y k_y} \end{bmatrix},\end{aligned}\quad (71)$$

where  $\kappa^{\text{out}}(\kappa)$  denotes the mapping relation between the input and output spatial frequency vectors because of the tilted plane,  $\tilde{a}(\kappa^{\text{out}})$  is the Jacobian determinant of this mapping,  $\tilde{\mathcal{B}}(\kappa^{\text{out}})$  is the propagation kernel,  $\tilde{\mathcal{M}}(\kappa^{\text{out}})$  is the field-components projection matrix, and  $\tilde{V}_\perp = (E_x, E_y)$  indicates the transversal components of the electric field.

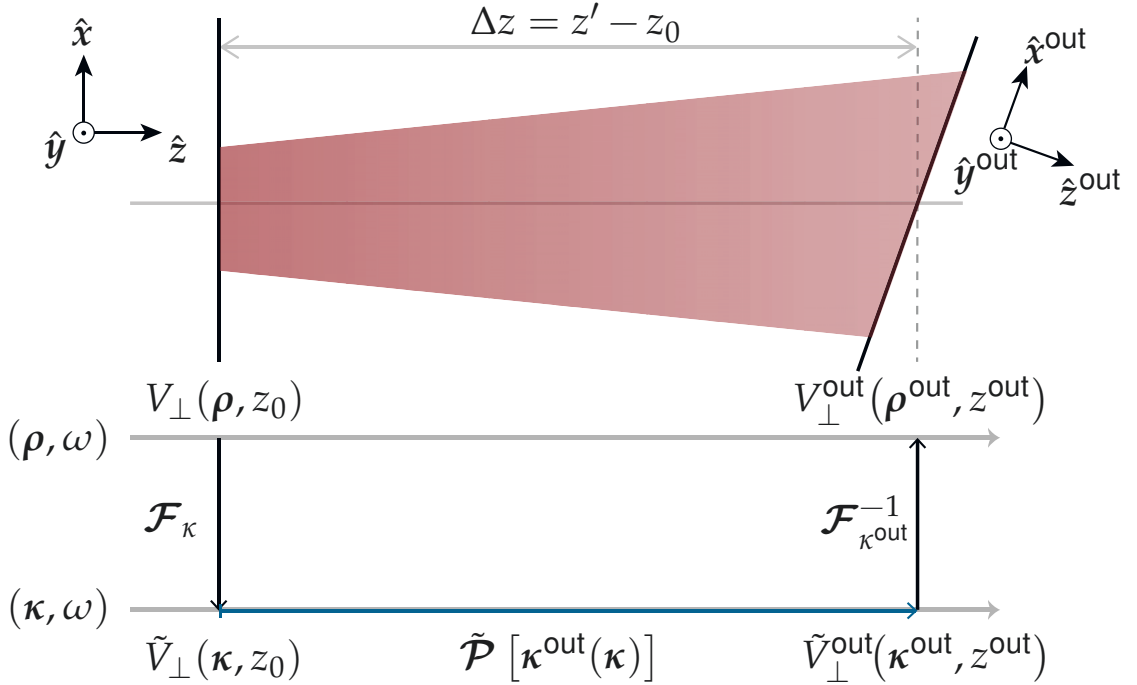


Figure 18: Propagation of a light field to a tilted plane in the free sapce, and the corresponding field-tracing diagram illustrating the same propagation process according to a spectrum-of-plane-wave (SPW) analysis. There we have two Cartesian coordinate systems,  $\Gamma^{\text{in}}$  and  $\Gamma^{\text{out}}$ , in which the input field  $V_\perp(\rho, z_0)$  and the output field  $V_\perp^{\text{out}}(\rho^{\text{out}}, z^{\text{out}})$  are respectively defined. The propagation distance  $\Delta z = z' - z_0$  is given in the coordinate system  $\Gamma^{\text{in}}$ .  $\tilde{\mathcal{P}}$  indicates the propagating operator in the spatial frequency domain.

Based on all the considerations above, the complete mathematical expression of the free space propagation operator between non-parallel planes can be explicitly written as

$$V_{\perp}^{\text{out}}(\boldsymbol{\rho}^{\text{out}}, z^{\text{out}}) = \mathcal{F}_{\kappa^{\text{out}}}^{-1} \{ \tilde{\mathcal{P}}[\kappa^{\text{out}}(\boldsymbol{\kappa})] \mathcal{F}_{\kappa}[V_{\perp}(\boldsymbol{\rho}, z_0)] \} . \quad (72)$$

In comparison to the situation of parallel planes, the numerical issues in the implementation of Eq. (72) is mainly focused on the usage of FFT techniques. Due to the non-linear mapping of spatial frequency vectors  $\kappa^{\text{out}}(\boldsymbol{\kappa})$ , the uniformly sampled input coordinate grid results in a non-uniform output coordinate grid in the  $k$ -domain. As a consequence, it is impossible to directly perform the IFFT to this non-uniform grid on the target plane. To enable the FFT techniques, we must interpolate the gridless sampled output spectrum. The corresponding difficulty and solution have been well-solved in [65]. In the present work, apart from the FFT technique, we have another two powerful advanced Fourier transform techniques. Certainly, the semi-analytical Fourier transform also requires the equidistant sampling. However, in the homeomorphic Fourier transform, there is no constraint on the format of the input field/spectrum. That means when HFT is allowed to use, the extension to non-parallel planes does not require significantly more computation time, since it entails just another pointwise operation which is based, together with the homeomorphic Fourier transform, on the gridless data concept in combination with mapping operations. Because of the tilt and the change of the coordinate system for the electric field vector Eq. (72) is in vectorial form. The other four field components can be calculated from  $(E_x, E_y)$  on demand.

#### 4.1.3 *Automatic selection of the Fourier transform techniques*

As we have shown in the previous two subsections, the  $k$ -domain propagation operator consists of a pair of Fourier transform integral operation and the pointwise propagation kernel. Generally, FFT techniques are used in its numerical implementation. However, due to the  $2\pi$ -modulo phase, FFT techniques also suffer from severe computational effort. A straightforward idea to overcome these numerical issues, is to employ the advanced Fourier transform techniques as long as the new technique is more efficient than the FFT and accurate enough.

Based on the field tracing diagram of the propagation between non-parallel planes, we added the further strategy about the usage of the Fourier transform techniques in Fig. 19. We can see that the only difference from the classic algorithms is on the freedom of Fourier transform operations. For both forward and backward Fourier transform, there are three choices of the advanced techniques. The validity condition and the critical threshold of the accuracy have been investigated for both the SFT and the HFT. Relative conclusions and formulas are respectively presented in Section. 2.1.5 and Section. 3.1.3. With the help of these

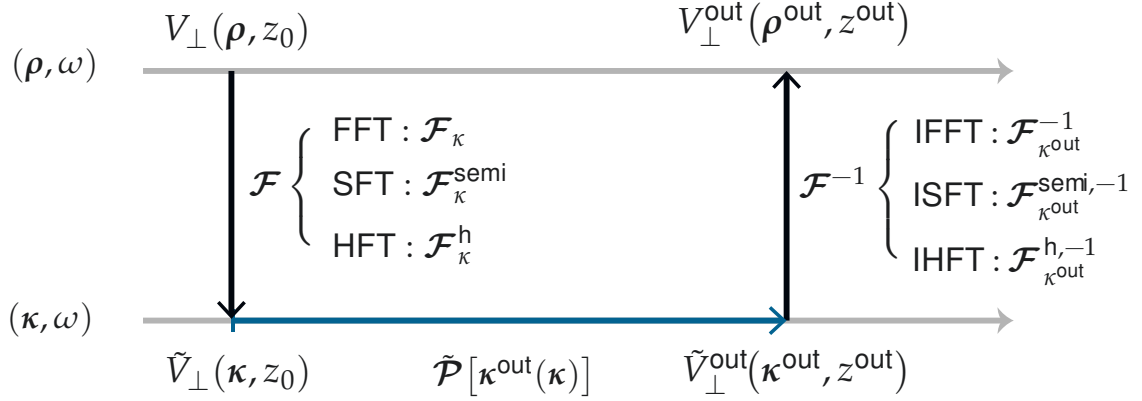


Figure 19: The field-tracing diagram of the free space propagation between two arbitrarily oriented planes.  $\mathcal{F}$  and  $\mathcal{F}^{-1}$  indicate the automatic selection of the most appropriate Fourier transform techniques in terms of the application scenes.

numerical criteria, we can precisely achieve the automatic selection for the most appropriate Fourier transform techniques in different situations. In the next sections, we generalize and interpret several well-known and influential diffraction integrals. Though entirely mathematical derivation, we prove these diffraction integral or propagation operators are the individual cases of the proposed  $k$ -domain propagation operator. Consequently, we concluded that the unified free space propagation operator, for different propagation scenes, would combine the most appropriate Fourier transform techniques and deliver the most numerically efficient solutions.

At last but not least, we would like to briefly introduce how to select the Fourier transform technique in the practical simulation. It is remarkable that the proposed strategy is not only applicable for the propagation operator but also other Maxwell's solvers as well.

1. HFT/IHFT: The pointwise operation has the highest priority. Firstly, we should perform the 1D-tests or the criteria given in Section. 3.1.3 to verify its validity.
2. SFT/ISFT: When the HFT is not allowed, we need to examine whether SFT/ISFT is more efficient than the FFT. the corresponding numerical criterion is given in Section. 2.1.5.
3. FFT/IFFT: In case both HFT and SFT are not suitable to select, we use the rigorous FFT/IFFT.

#### 4.2 GENERALIZATION OF TWO DIFFRACTION INTEGRALS

In the first section, we proposed the unified free space propagation operator via the  $k$ -domain analysis alongside the advanced Fourier transform techniques. As we learned during the derivation process, for different propagation scenes, the unified propagation operator would select the most appropriate Fourier transform pair automatically and result in the minimization of the computational effort. Analogous to some well-known diffraction integrals, at the corresponding situation, the proposed unified operator exhibits the same numerical characteristics. In the following section, we review and generalize two essential diffraction integrals from the aspect of the unified free space propagation operator.

##### 4.2.1 Generalized Debye integral

In 1909, Debye published his work to demonstrate the general features of a diffracted field near its focus. The Debye integral is commonly used to efficiently tackle the problem of focusing light in lens design. However, this approximate method is only valid for systems that are well designed and with high enough Fresnel numbers [62, 106]. Beyond this assumption, the integral formula fails to provide accurate results. In this section, we generalize the Debye integral to overcome some of its limitations [107]. Let us consider a convergent incident light field which is propagating in the positive  $z$  direction towards the target plane  $z = z'$  located in the focal region of the light field. The situation is illustrated in

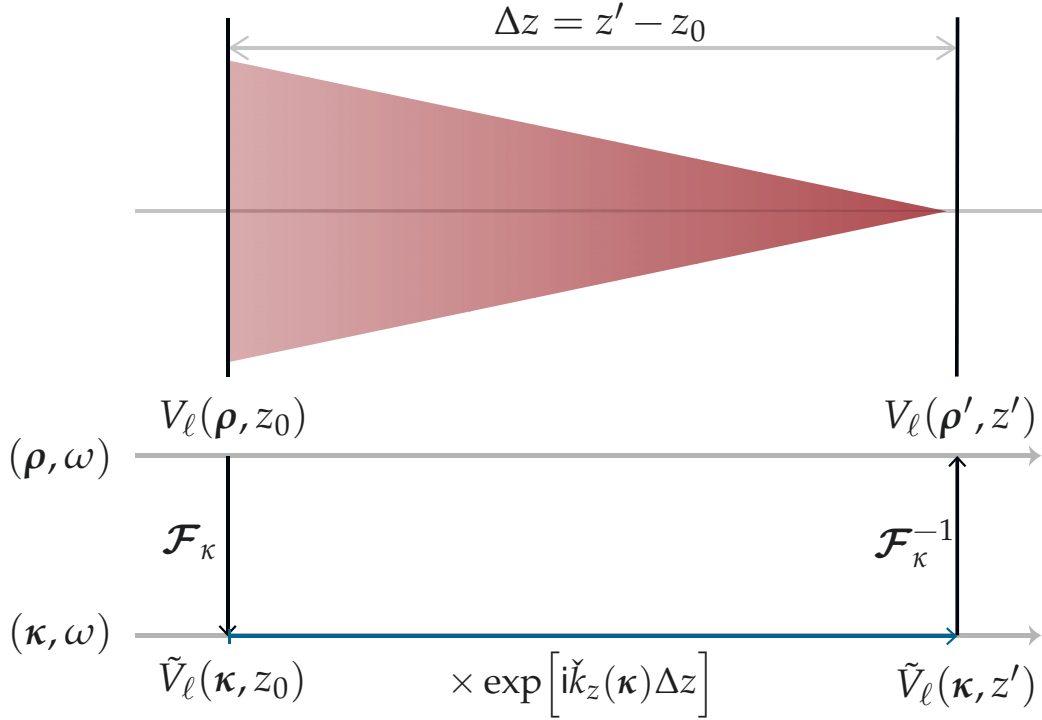


Figure 20: Schematic illustration of a convergent wave in free space (Debye integral), and the corresponding field-tracing diagram illustrating the same propagation process according to the  $k$ -domain analysis. The incident beam is propagated from the input plane located at  $z = z_0$  to the target plane, with propagating distance  $\Delta z = z' - z_0$ .

Fig. 20. In lens design,  $z = z_0$  might be the position of the exit pupil and  $\Delta z = f$  the back focal length. As any electromagnetic field component will, in general, be complex-valued, we can write the field at  $z = z_0$ ,  $V_\ell(\boldsymbol{\rho}, z_0)$ , in terms of its amplitude and phase,

$$V_\ell(\boldsymbol{\rho}, z_0) = |V_\ell(\boldsymbol{\rho}, z_0)| \exp \{i \arg [V_\ell(\boldsymbol{\rho}, z_0)]\}. \quad (73)$$

In general, the field at  $z_0$  possesses a smooth wavefront which is common to all field components. For instance, in an aberration-free focusing system, the wavefront phase should be ideal spherical without any additional residual phase.

Thus, we can reformulate Eq. (73) to yield

$$V_\ell(\boldsymbol{\rho}, z_0) = U_\ell(\boldsymbol{\rho}) \exp [i\psi^{\text{in}}(\boldsymbol{\rho})], \quad (74)$$

where we have extracted the smooth wavefront phase  $\psi^{\text{in}}(\boldsymbol{\rho})$  and grouped the residual of the phase alongside the amplitude  $|V_\ell(\boldsymbol{\rho}, z_0)|$  into  $U_\ell(\boldsymbol{\rho})$ . It should

be noted that the choice of function  $\psi^{\text{in}}(\boldsymbol{\rho})$  is arbitrary and Eq. (74) entails no approximation. It merely constitutes an alternative way of expressing  $V_\ell(\boldsymbol{\rho}, z_0)$ . Next, let us consider a general wavefront phase  $\psi^{\text{in}}(\boldsymbol{\rho})$ . Although there is no analytical expression of the given wavefront function, its gradient formula can be formulated implicitly as

$$\nabla_\perp \psi^{\text{in}}(\boldsymbol{\rho}) = \boldsymbol{\kappa}(\boldsymbol{\rho}). \quad (75)$$

Using the mapping from Eq. (75) allows us to reformulate the Fourier integral as a pointwise operation, i.e, homeomorphic Fourier transform. The resulting spectrum read as

$$\begin{aligned} \tilde{V}_\ell(\boldsymbol{\kappa}, z_0) &\approx a[\boldsymbol{\rho}(\boldsymbol{\kappa})] U_\ell[\boldsymbol{\rho}(\boldsymbol{\kappa})] \exp\{i\psi^{\text{in}}[\boldsymbol{\rho}(\boldsymbol{\kappa})] - i\boldsymbol{\kappa} \cdot \boldsymbol{\rho}(\boldsymbol{\kappa})\} \\ &= \tilde{A}_\ell(\boldsymbol{\kappa}) \exp[i\tilde{\psi}^{\text{in}}(\boldsymbol{\kappa})] \end{aligned} \quad (76)$$

The amplitude scaling factor  $a(\boldsymbol{\rho})$  is provided by the Jacobian determinant of the mapping from Eq. (75) so that, using the definition  $\psi_{x_i x_j} \stackrel{\text{def}}{=} \frac{\partial \psi}{\partial x_i \partial x_j}$ :

$$a(\boldsymbol{\rho}) = \begin{cases} \sqrt{\frac{i}{\psi_{xx}^{\text{in}}(\boldsymbol{\rho})}} \sqrt{-\frac{i\psi_{xx}^{\text{in}}(\boldsymbol{\rho})}{[\psi_{xy}^{\text{in}}(\boldsymbol{\rho})]^2 - \psi_{xx}^{\text{in}}(\boldsymbol{\rho}) \psi_{yy}^{\text{in}}(\boldsymbol{\rho})}} & , \quad \psi_{xx}^{\text{in}}(\boldsymbol{\rho}) \neq 0 \\ \frac{1}{|\psi_{xy}^{\text{in}}(\boldsymbol{\rho})|} & , \quad \psi_{xx}^{\text{in}}(\boldsymbol{\rho}) = 0 \end{cases} \quad (77)$$

In practice, the mapping  $\boldsymbol{\rho} = \boldsymbol{\rho}(\boldsymbol{\kappa})$  is known only numerically, and although this requires handling some gridless data in the algorithm, it should not pose a problem when performing the HFT in practice. By introducing appropriate error estimations within the algorithm, we can control the level of accuracy of replacing the FFT by the HFT. This is part of the mathematical concept of the HFT and does not rely on decisions of the physical model. To finalize the derivation of the generalized Debye integral, plugging Eq. (76) into Eq. (69) leads to the formula

$$\begin{aligned} V_\ell(\boldsymbol{\rho}', z') &= \mathcal{F}_\kappa^{-1} \left\{ \tilde{V}_\ell(\boldsymbol{\kappa}, z_0) \exp[i\check{k}_z(\boldsymbol{\kappa}) \Delta z] \right\} \\ &= \mathcal{F}_\kappa^{-1} \left\{ \tilde{A}(\boldsymbol{\kappa}) \exp[i\tilde{\psi}^{\text{in}}(\boldsymbol{\kappa}) + i\check{k}_z(\boldsymbol{\kappa}) \Delta z] \right\} \\ &= \mathcal{F}_\kappa^{-1} \left( a[\boldsymbol{\rho}(\boldsymbol{\kappa})] U_\ell[\boldsymbol{\rho}(\boldsymbol{\kappa})] \exp\{i\psi^{\text{in}}[\boldsymbol{\rho}(\boldsymbol{\kappa})] - i\boldsymbol{\kappa} \cdot \boldsymbol{\rho}(\boldsymbol{\kappa}) + i\check{k}_z(\boldsymbol{\kappa}) \Delta z\} \right), \end{aligned} \quad (78)$$

where  $\mathcal{F}_\kappa^{-1}$  indicates the inverse Fourier-transform operation from  $\boldsymbol{\kappa}$  to  $\boldsymbol{\rho}'$  at the target plane. Eq. (78) constitutes the major result of this work and expresses

the generalized Debye integral with the use of the Fourier integral operator  $\mathcal{F}$  for the sake of compactness. As mentioned before, the mapping relation  $\rho(\kappa)$  is in general available only numerically. Hence, it is not possible to resolve the integral analytically.

Different from the SPW formula of Eq. (69), in the generalized Debye integral, two FT integrals are reduced to one FT operation. More importantly, according to the homeomorphic Fourier transform, the wavefront phase  $\tilde{\psi}^{\text{in}}(\kappa)$  can be treated in an isolated manner during the process. This means that up until the last inverse Fourier-transform operation, it is possible to use different approaches to sample the wavefront phase  $\tilde{\psi}^{\text{in}}(\kappa)$ , instead of in the form of a “ $2\pi$ -modulo” phase. In the end, since the high-frequency phase component of  $\tilde{\psi}^{\text{in}}(\kappa)$  would be partly compensated by the propagating kernel  $k_z(\kappa)\Delta z$ , we can select the inverse FFT technique to carry out the inverse Fourier transform with low sampling effort.

#### *Standard Debye integral as a special case*

For a convergent spherical wavefront phase  $\psi^{\text{in}}$  with radius of curvature  $R$ , i.e.

$$\psi^{\text{in}}(\rho) = \psi^{\text{sph}}(\rho) = \text{sign}(R) k_0 n \sqrt{\rho^2 + R^2}, \quad (79)$$

the mapping in Eq. (75) and the factor  $a(\rho(\kappa))$  of Eq. (77) can be evaluated analytically. Here,  $n$  is the real part of the refractive index. And, in the considered cases,  $\psi^{\text{in}}$  is a convergent spherical phase, so the radius of curvature is negative, i.e.,  $R < 0$ . From Eq. (75) follow for the  $\psi^{\text{sph}}$  of Eq. (79) the mapping equations

$$\begin{cases} \kappa(\rho) = -k_0 n \frac{\rho}{\sqrt{\rho^2 + R^2}} \\ \rho(\kappa) = R \frac{\kappa}{k_z(\kappa)} \end{cases} \quad (80)$$

in explicit form. Here,  $k_z(\kappa)$  is defined as  $k_z(\kappa) = \sqrt{k_0^2 n^2 - \kappa^2}$ . The Jacobian determinant can be evaluated for this mapping and we obtain the scaling factor

$$a^{\text{sph}}(\rho(\kappa)) = i \frac{k_0 n R}{k_z^2(\kappa)} \quad (81)$$

in a compact and analytical form. The expression  $\psi^{\text{in}}(\rho(\kappa)) - \kappa \cdot \rho(\kappa) + \check{k}_z(\kappa)\Delta z$  in Eq. (78) reduces to  $\check{k}_z(\kappa)\Delta z + k_z(\kappa)R$  for the spherical wavefront phase by

using the mapping relations of Eq. (80). Inserting these results into Eq. (78) provides

$$V_\ell(\boldsymbol{\rho}, z) = i\mathcal{F}_\kappa^{-1} \left\{ \frac{k_0 n R}{k_z^2(\boldsymbol{\kappa})} U_\ell[\boldsymbol{\rho}(\boldsymbol{\kappa})] \exp \left[ i\check{k}_z(\boldsymbol{\kappa}) \Delta z + k_z(\boldsymbol{\kappa}) R \right] \right\}, \quad (82)$$

with  $\boldsymbol{\rho}(\boldsymbol{\kappa})$  from Eq. (80). This integral formula constitutes the special case of Eq. (78) which emerges when we select a spherical wavefront phase. The complex amplitude  $U_\ell$  comprises magnitude and phase variations, including aberrations.

To recognize that Eq. (82) is identical with the standard Debye integral, we express  $U$  as the magnitude of a spherical wave component:

$$U_\ell(\boldsymbol{\rho}) = \frac{T_\ell(\boldsymbol{\rho})}{r}, \quad (83)$$

with  $r = \sqrt{\boldsymbol{\rho}^2 + R^2}$ . The magnitude  $|T_\ell(\boldsymbol{\rho})|$  expresses apodization and vignetting effects in lens design, whereas  $\arg[T_\ell(\boldsymbol{\rho})]$  comprises the aberrations. With the mapping from Eq. (80),  $r = \sqrt{\boldsymbol{\rho}^2 + f^2}$  can be reformulated to yield  $1/r = k_z/(|R|k_0 n)$ . Inserting  $U_\ell(\boldsymbol{\rho})$  of Eq. (83) into (82) results in

$$V_\ell(\boldsymbol{\rho}, z) = -i\mathcal{F}_\kappa^{-1} \left\{ \frac{T_\ell(\boldsymbol{\rho}(\boldsymbol{\kappa}))}{k_z(\boldsymbol{\kappa})} \exp \left[ i\check{k}_z(\boldsymbol{\kappa}) \Delta z + k_z(\boldsymbol{\kappa}) R \right] \right\}, \quad (84)$$

which takes us to the standard Debye integral formula in a compact notation with the Fourier integral operator. In the case of a diffraction-limited field in the exit pupil the wavefront phase is purely spherical, and the extended and the standard Debye integral would therefore provide the same result. The difference between the two becomes obvious when aberrations are present. The standard Debye integral deals with them in  $\arg[T_\ell(\boldsymbol{\rho})]$ , whereas in the generalized formula of Eq. (78) the aberrations are included in  $\psi^{\text{in}}$ , a term which has direct influence on the mapping and which consequently provides more accurate results without incurring higher numerical effort.

#### 4.2.2 Generalized far-field integral

The diffraction pattern of a light field in the far-field zone is always a subject of interest [108–110]. The far-field integral is widely acknowledged to deal with



the propagation problem from the focal region to the far-field area. Conventionally, based on the far-field assumption, the Rayleigh-Sommerfeld integral of the first kind can be approximated and deduced to the far-field integral [26, 70, 111]. Analogous to the generalized Debye integral, we would generalize and interpret the far-field integral via the  $k$ -domain analysis, instead of the traditional  $x$ -domain approach. To illustrate the physical process, we present a sketch as well as the field tracing diagram in Fig. 21.

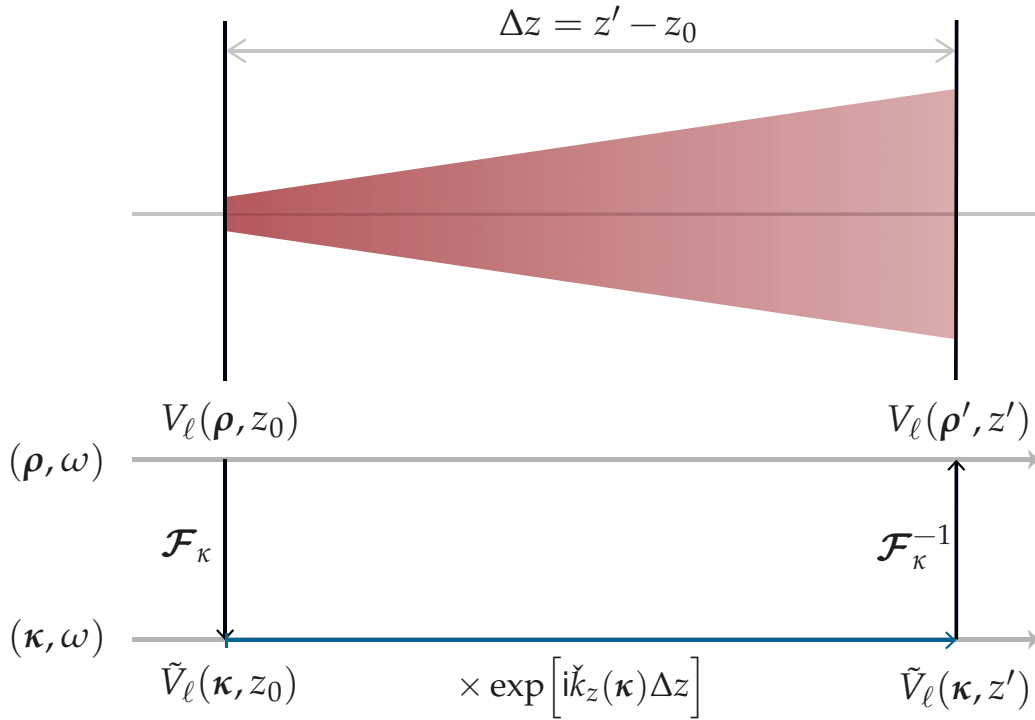


Figure 21: Schematic illustration of a divergent wave in free space (far-field integral), and the corresponding field-tracing diagram illustrating the same propagation process according to the  $k$ -domain analysis. The incident beam is propagated from the input plane located at  $z = z_0$  to the target plane, with propagating distance  $\Delta z = z' - z_0$ .

First of all, let us have a look at the forward Fourier transform operation at the input plane. As the input plane located in the focal region, the incident field doesn't contain an intense wavefront phase. Therefore, the homeomorphic

Fourier transform is not allowed, and we must select the rigorous FFT. The resulting spectrum can be written in terms of its amplitude and phase,

$$\tilde{V}_\ell(\boldsymbol{\kappa}, z_0) = \mathcal{F}_\kappa[V_\ell(\boldsymbol{\rho}, z_0)] = |\tilde{V}_\ell(\boldsymbol{\kappa}, z_0)| \exp \{i \arg [\tilde{V}_\ell(\boldsymbol{\kappa}, z_0)]\}. \quad (85)$$

Without loss of generality, reformulating Eq. (85) yields

$$\tilde{V}_\ell(\boldsymbol{\kappa}, z_0) = \tilde{A}_\ell(\boldsymbol{\kappa}) \exp[i\tilde{\psi}^{\text{in}}(\boldsymbol{\kappa})], \quad (86)$$

where we have extracted the smooth wavefront phase  $\tilde{\psi}^{\text{in}}(\boldsymbol{\kappa})$  and grouped the residual of the phase with the amplitude  $|\tilde{V}_\ell(\boldsymbol{\kappa}, z_0)|$  into  $\tilde{A}_\ell(\boldsymbol{\kappa})$ . For a typical system with some aberrations, the extracted wavefront phase corresponds to the mapped aberration phase in the  $k$ -domain. Thus, considering the propagation kernel phase term of Eq. (68), the output wavefront phase in the  $k$ -domain can be written as

$$\tilde{\psi}^{\text{out}}(\boldsymbol{\kappa}) = \Delta\tilde{\psi}^{\text{in}}(\boldsymbol{\kappa}) + \check{k}_z(\boldsymbol{\kappa}) \Delta z. \quad (87)$$

In the case of large propagation distance,  $\check{k}_z(\boldsymbol{\kappa}) \Delta z$  dominates the output wavefront phase, and  $\Delta\tilde{\psi}^{\text{in}}(\boldsymbol{\kappa})$  is regarded as the correction term for the aberration phases. Then, inserting Eq. (86-87) into Eq. (69) provides

$$\begin{aligned} V_\ell(\boldsymbol{\rho}', z') &= \mathcal{F}_\kappa^{-1} \left\{ \mathcal{F}_\kappa[V_\ell(\boldsymbol{\rho}, z_0)] \times \exp[i\check{k}_z(\boldsymbol{\kappa}) \Delta z] \right\} \\ &\approx \mathcal{F}_\kappa^{\text{h}, -1} \left\{ \tilde{A}_\ell(\boldsymbol{\kappa}, z_0) \exp[i\tilde{\psi}^{\text{out}}(\boldsymbol{\kappa})] \right\}. \end{aligned} \quad (88)$$

To this point, we can directly utilize the conclusion of the inverse homeomorphic Fourier transform,

$$V_\ell(\boldsymbol{\rho}', z') = \tilde{a}[\boldsymbol{\kappa}(\boldsymbol{\rho}')] \tilde{A}_\ell[\boldsymbol{\kappa}(\boldsymbol{\rho}'), z_0] \exp\{i\tilde{\psi}^{\text{out}}[\boldsymbol{\kappa}(\boldsymbol{\rho}')] + i\boldsymbol{\rho}' \cdot \boldsymbol{\kappa}(\boldsymbol{\rho}')\}, \quad (89)$$

with Jacobian determinant factor

$$\tilde{a}(\boldsymbol{\kappa}) = \begin{cases} \sqrt{\frac{i}{\tilde{\psi}_{k_x k_x}^{\text{out}}(\boldsymbol{\kappa})}} \sqrt{-\frac{i\tilde{\psi}_{k_x k_x}^{\text{out}}(\boldsymbol{\kappa})}{[\tilde{\psi}_{k_x k_y}^{\text{out}}(\boldsymbol{\kappa})]^2 - \tilde{\psi}_{k_x k_x}^{\text{out}}(\boldsymbol{\kappa}) \tilde{\psi}_{k_y k_y}^{\text{out}}(\boldsymbol{\kappa})}} & , \quad \tilde{\psi}_{k_x k_x}^{\text{out}}(\boldsymbol{\kappa}) \neq 0 \\ \frac{1}{|\tilde{\psi}_{k_x k_x}^{\text{out}}(\boldsymbol{\kappa})|} & , \quad \tilde{\psi}_{k_x k_x}^{\text{out}}(\boldsymbol{\kappa}) = 0 \end{cases}. \quad (90)$$

Substituting Eq. (86-87) into Eq. (89), we can write the generalized far-field integral in a compact form,

$$V_\ell(\boldsymbol{\rho}', z') = \tilde{a}[\boldsymbol{\kappa}(\boldsymbol{\rho}')] \exp\{i\check{k}_z[\boldsymbol{\kappa}(\boldsymbol{\rho}')] \Delta z + i\boldsymbol{\rho}' \cdot \boldsymbol{\kappa}(\boldsymbol{\rho}')\} \mathcal{F}_\kappa[V_\ell(\boldsymbol{\rho}, z_0)]_{\boldsymbol{\kappa} \rightarrow \boldsymbol{\rho}'}, \quad (91)$$

where the backward mapping  $\kappa = \kappa(\rho')$  is provided by the gradient of the output wavefront phase

$$\tilde{\nabla}_{\perp} \tilde{\psi}^{\text{out}}(\kappa) = -\rho'. \quad (92)$$

Like the mapping in the generalized Debye integral, there is no analytical expression for the pointwise mapping relation  $\kappa = \kappa(\rho')$ . Eq. (91-92) must be handled entirely in a numerical manner. Fortunately, this should not pose an issue since all related problem has been fully solved in the implementation of the homeomorphic Fourier transform. From a numerical point of view, the generalized far-field integral simplifies the inverse FFT of substantial computational effort into a pointwise operation. It leads to a significant reduction of the sampling points and outstanding improvement of the performance. From a physical point of view, the only approximation used in the generalized far-field integral is on the inverse HFT. The inclusion of the aberrant phase  $\Delta\tilde{\psi}^{\text{in}}(\kappa)$  dramatically extends the application scope of the proposed approach. The inclusion of the aberrant phase  $\Delta\tilde{\psi}^{\text{in}}(\kappa)$  in Eq. (87) dramatically extends its application scope, that the generalized far-field integral is not strictly restricted to the far-field region. Consequently, the generalized far-field integral enables the propagation task for the field with intensive aberrations and of a medium propagating distance. Also, in practice, by examining the level of accuracy of the inverse HFT, we can decide whether to employ the proposed algorithm.

#### *Standard far-field integral as a special case*

As we mentioned in above content, the mapping relation  $\kappa \rightarrow \rho'$  is available only numerically. For resolving the diffraction integral analytically, we must simplify the experimental model and introduce more approximations. Therefore, we omit the aberration phase term and assume the wavefront phase of the output spectrum in the  $k$ -domain is fully contributed by the propagation kernel. Thus, the Eq. (87) becomes

$$\tilde{\psi}^{\text{out}}(\kappa) = \tilde{\psi}^{\text{far}}(\kappa) = \check{k}_z(\kappa) \Delta z. \quad (93)$$

Plugging Eq. (93) into Eq. (69) leads

$$V_{\ell}(\rho', z') \approx \mathcal{F}_{\kappa}^{\text{h}, -1} \left\{ \tilde{V}_{\ell}(\kappa, z_0) \exp \left[ i \tilde{\psi}^{\text{far}}(\kappa) \right] \right\}. \quad (94)$$

Following Eq. (92), the bijective mapping relation of the  $\tilde{\psi}'(\kappa)$  can be written in an explicit form

$$\kappa(\rho') = k_0 \tilde{n} \frac{\rho'}{R(\rho')} \quad (95)$$

where  $R(\rho') = \sqrt{||\rho'||^2 + \Delta z^2}$ . For this mapping, the scaling factor (Jacobian determinant) can be evaluated by

$$\tilde{a}[\kappa(\rho')] = -i \frac{k_0 \tilde{n} \Delta z}{R^2(\rho')}, \quad (96)$$

and the phase modulation term can be derived

$$\tilde{\psi}^{\text{far}}[\kappa(\rho')] + \kappa(\rho') \cdot \rho' = k_0 \tilde{n} R(\rho'). \quad (97)$$

According to the inverse homeomorphic Fourier transform formula, we obtain

$$\begin{aligned} V_\ell(\rho', z') &\approx \tilde{a}[\kappa(\rho')] \tilde{V}_\ell[\kappa(\rho'), z_0] \exp\{i \tilde{\psi}^{\text{far}}[\kappa(\rho')] + i \kappa(\rho') \cdot \rho'\} \\ &= -i k_0 \tilde{n} \frac{\Delta z}{R(\rho')} \frac{\exp[i k_0 \tilde{n} R(\rho')]}{R(\rho')} \mathcal{F}_\kappa[V_\ell(\rho, z_0)]_{\kappa = -k_0 \tilde{n} \frac{\rho'}{R(\rho')}}. \end{aligned} \quad (98)$$

Eq. (98) reveals that any light field component in the far-field zone turns into a spherical wave function. This spherical wave function is modulated by the Fourier transform of the input field. The modulation scales are not linear to the transversal coordinates but obey the mapping relation of Eq. (96). In contrast to the generalized far-field integral of Eq. (91), the far-field integral makes more approximation on Fourier transform that we assume the mapping of inverse HFT follows a spherical phase function. So, in the case of an aberration-free system, both approaches would provide precisely the same result. But, for the system presenting aberrations, the inclusion of the aberration phase of Eq. (87) has a direct influence on the mapping and would significantly improve the accuracy of the inverse homeomorphic Fourier transform. To distinguish the application scope of the far-field integral and the generalized approach, we would like to introduce two new notions in terms of the usage of the homeomorphic Fourier transform:

- Homeomorphic field zone (HFZ): in which the field presents a general homeomorphic wavefront phase. HFT is allowed and can provide an accurate result as the rigorous FFT.

- Far-field zone (FFZ): in which the field presents a purely spherical wavefront phase. Restricted HFT (mapping provided by only the spherical phase function) can provide the accurate result.

With this, the far-field zone indicates the application scope of the far-field integral, and the homeomorphic field zone corresponds to the generalized far-field integral. It is no doubt that any field would present a spherical wavefront at an infinite distance from the source. Thus, the far-field zone must be a subset of the homeomorphic field zone.

### 4.3 INTERPRETATION OF TWO FAST PROPAGATION OPERATORS

Besides the Debye integral and far-field integral, there are also various approximate propagation operators. For instance, benefits from its computational advantage, the ray-tracing algorithm is the most widely used propagation scenario in modern optical modeling and design, especially for the lens system [3, 112]. In this section, using the same logic as before, we would discuss two essential propagation operators.

#### 4.3.1 *Pointwise operator: ray tracing algorithm*

In the ray tracing, the light field is described by discrete idealized narrow beams, and the propagation problem is entirely solved by the conventional geometric optics, i.e., Fermat's principle and Snell's law. Different from the other integral operator, the ray tracing algorithm thoroughly performs a pointwise operation that exhibits the impressive computational characteristic. Its numerical complexity is linearly proportional to the number of sampling points, i.e.,  $\mathcal{O}(N)$ .

Turning our attention back to the unified free space propagation operator, the intuition tells us there must be an internal connection between the ray tracing operator and the unified approach. We have learned that the homeomorphic Fourier transform and its inverse transform are both pointwise operations. Besides, we know that the propagation kernel in the  $k$ -domain is also in the manner of pointwise. Therefore, let us assume both the input field and the output field are in the homeomorphic field zone. Substituting the pointwise Fourier trans-

form techniques for the rigorous Fourier transform integrals in Eq. (69), the resulting expression reads

$$V_\ell(\rho', z') \approx \mathcal{F}_\kappa^{\text{h}, -1} \left\{ \mathcal{F}_\kappa^{\text{h}} [V_\ell(\rho, z_0)] \times \exp \left[ i \check{k}_z(\kappa) \Delta z \right] \right\}. \quad (99)$$

Under our assumption of the homeomorphic field zone, the input field at  $z = z_0$  possesses a smooth wavefront which is common to all field components. So, we can write the input field  $V_\ell(\rho, z_0)$  as

$$\begin{aligned} V_\ell(\rho, z_0) &= |V_\ell(\rho, z_0)| \exp \{ i \arg [V_\ell(\rho, z_0)] \} \\ &= U_\ell(\rho, z_0) \exp [i\psi^{\text{in}}(\rho)], \end{aligned} \quad (100)$$

where  $\psi^{\text{in}}(\rho)$  is the extracted smooth wavefront phase at the input plane. Please note that Eq. (100) is merely an alternative way to express the field component without any approximation. In homeomorphic Fourier transform, the pointwise bijective mapping  $\rho \leftrightarrow \kappa$  is governed by

$$\nabla_\perp \psi^{\text{in}}(\rho) = \kappa(\rho). \quad (101)$$

By employing homeomorphic Fourier transform, we obtain the spectrum at the input plane

$$\begin{aligned} \tilde{V}_\ell(\kappa, z_0) &\approx \mathcal{F}_\kappa^{\text{h}} [V_\ell(\rho, z_0)] \\ &= a^{\text{in}}[\rho(\kappa)] U[\rho(\kappa), z_0] \exp \{ i\psi^{\text{in}}[\rho(\kappa)] - i\kappa \cdot \rho(\kappa) \}. \end{aligned} \quad (102)$$

Here, the amplitude scaling factor  $a^{\text{in}}(\rho)$  is provided by the Jacobian determinant of the mapping from Eq. (101), and it is defined as

$$a^{\text{in}}(\rho) = \begin{cases} \sqrt{\frac{i}{\psi_{xx}^{\text{in}}(\rho)}} \sqrt{-\frac{i\psi_{xx}^{\text{in}}(\rho)}{[\psi_{xy}^{\text{in}}(\rho)]^2 - \psi_{xx}^{\text{in}}(\rho) \psi_{yy}^{\text{in}}(\rho)}} & , \quad \psi_{xx}^{\text{in}}(\rho) \neq 0 \\ \frac{1}{|\psi_{xy}^{\text{in}}(\rho)|} & , \quad \psi_{xx}^{\text{in}}(\rho) = 0 \end{cases} \quad (103)$$

where  $\psi_{x_i x_j} \stackrel{\text{def}}{=} \frac{\partial \psi}{\partial x_i \partial x_j}$ .

Plugging Eq. (102) into Eq. (99), we have

$$\begin{aligned} V_\ell(\rho', z') &\approx \mathcal{F}_\kappa^{\text{h}, -1} \left\{ a^{\text{in}}[\rho(\kappa)] U[\rho(\kappa), z_0] \exp \left( i\psi^{\text{in}}[\rho(\kappa)] - i\kappa \cdot \rho(\kappa) + i\check{k}_z(\kappa) \Delta z \right) \right\} \\ &= \mathcal{F}_\kappa^{\text{h}, -1} \left\{ a^{\text{in}}[\rho(\kappa)] U[\rho(\kappa), z_0] \exp [i\tilde{\psi}^{\text{out}}(\kappa)] \right\}. \end{aligned} \quad (104)$$

Again, let us formulate the expression of the output spectrum,

$$\begin{aligned}\tilde{V}_\ell(\boldsymbol{\kappa}, z') &= a^{\text{in}}[\boldsymbol{\rho}(\boldsymbol{\kappa})] U[\boldsymbol{\rho}(\boldsymbol{\kappa}), z_0] \exp[i\tilde{\psi}^{\text{out}}(\boldsymbol{\kappa})] \\ &= \tilde{A}(\boldsymbol{\kappa}, z') \exp[i\tilde{\psi}^{\text{out}}(\boldsymbol{\kappa})]\end{aligned}\quad (105)$$

where  $\tilde{\psi}^{\text{out}}(\boldsymbol{\kappa})$  is the extracted smooth wavefront phase of the output spectrum in the  $k$ -domain. The backward mapping from  $\boldsymbol{\kappa}$  to  $\boldsymbol{\rho}'$  is provided by

$$\tilde{\nabla}_\perp \tilde{\psi}^{\text{out}}(\boldsymbol{\kappa}) = \boldsymbol{\rho}'(\boldsymbol{\kappa}). \quad (106)$$

where  $\boldsymbol{\rho}' = (x', y')$  spans the transverse plane at  $z' = z + z_0$ . Following an analogous process, the inverse homeomorphic Fourier transform can be achieved

$$\begin{aligned}V_\ell(\boldsymbol{\rho}', z') &\approx \mathcal{F}_\kappa^{\text{h}, -1} [\tilde{V}_\ell(\boldsymbol{\kappa}, z')] \\ &= \tilde{a}^{\text{out}}[\boldsymbol{\kappa}(\boldsymbol{\rho}')] \tilde{A}[\boldsymbol{\kappa}(\boldsymbol{\rho}'), z'] \exp\{i\tilde{\psi}^{\text{out}}[\boldsymbol{\kappa}(\boldsymbol{\rho}')] + i\boldsymbol{\rho}' \cdot \boldsymbol{\kappa}(\boldsymbol{\rho}')\}\end{aligned}\quad (107)$$

with

$$\tilde{a}^{\text{out}}(\boldsymbol{\kappa}) = \begin{cases} \sqrt{\frac{i}{\tilde{\psi}_{k_x k_x}^{\text{out}}(\boldsymbol{\kappa})}} \sqrt{-\frac{i\tilde{\psi}_{k_x k_x}^{\text{out}}(\boldsymbol{\kappa})}{[\tilde{\psi}_{k_x k_y}^{\text{out}}(\boldsymbol{\kappa})]^2 - \tilde{\psi}_{k_x k_x}^{\text{out}}(\boldsymbol{\kappa}) \tilde{\psi}_{k_y k_y}^{\text{out}}(\boldsymbol{\kappa})}} & , \quad \tilde{\psi}_{k_x k_x}^{\text{out}}(\boldsymbol{\kappa}) \neq 0 \\ \frac{1}{|\tilde{\psi}_{k_x k_y}^{\text{out}}(\boldsymbol{\kappa})|} & , \quad \tilde{\psi}_{k_x k_x}^{\text{out}}(\boldsymbol{\kappa}) = 0 \end{cases} \quad (108)$$

where  $\tilde{\psi}_{k_i k_j} \stackrel{\text{def}}{=} \frac{\partial \tilde{\psi}}{\partial k_i \partial k_j}$ .

At this point, we should emphasize that since the forward mapping in Eq. (101) and the backward mapping in Eq. (106) are both bijective. So, we have a completely interconnected mapping relation  $\boldsymbol{\rho} \leftrightarrow \boldsymbol{\kappa} \leftrightarrow \boldsymbol{\rho}'$ . Therefore, it is flexible to use any one of these three variables to describe the expression. Then, let us turn our attention on the phase term in Eq. (107), and reformulate it with the variable  $\boldsymbol{\kappa}$ ,

$$\begin{aligned}\tilde{\psi}^{\text{out}}(\boldsymbol{\kappa}) + \boldsymbol{\rho}'(\boldsymbol{\kappa}) \cdot \boldsymbol{\kappa} &= \psi^{\text{in}}[\boldsymbol{\rho}(\boldsymbol{\kappa})] + [\boldsymbol{\rho}'(\boldsymbol{\kappa}) - \boldsymbol{\rho}(\boldsymbol{\kappa})] \cdot \boldsymbol{\kappa} + \check{k}_z(\boldsymbol{\kappa}) \Delta z \\ &= \psi^{\text{in}}[\boldsymbol{\rho}(\boldsymbol{\kappa})] + k_x \Delta x + k_y \Delta y + \check{k}_z \Delta z \\ &= \psi^{\text{in}}[\boldsymbol{\rho}(\boldsymbol{\kappa})] + \psi^{\text{OPL}}[\boldsymbol{\rho}(\boldsymbol{\kappa})],\end{aligned}\quad (109)$$

where  $\boldsymbol{\rho}' - \boldsymbol{\rho} = (\Delta x, \Delta y)$  is the transverse displacement in the spatial domain. Eq. (101) and Eq. (106) reveals that  $\boldsymbol{\kappa}$  is the local gradient of the wavefront phase. And, in terms of the property of Fourier transform,  $\boldsymbol{\kappa}$  also corresponds to the

propagation direction of the decomposed plane wave. Considering the bijective mapping feature and geometric relation, we deduced that  $\psi^{\text{OPL}}[\boldsymbol{\rho}(\boldsymbol{\kappa})]$  indicates the phase term corresponding to the optical path length.

Last but not least, by inserting Eq. (102) and Eq. (109) into Eq. (107), we concluded the compact expression for the pointwise propagation operator,

$$\begin{aligned} V_\ell(\boldsymbol{\rho}', z') &\approx a^{\text{in}}[\boldsymbol{\rho}(\boldsymbol{\rho}')] \tilde{a}^{\text{out}}[\boldsymbol{\kappa}(\boldsymbol{\rho}')] U[\boldsymbol{\rho}(\boldsymbol{\rho}'), z_0] \exp \{i\psi^{\text{in}}[\boldsymbol{\rho}(\boldsymbol{\rho}')] + i\psi^{\text{OPL}}[\boldsymbol{\rho}(\boldsymbol{\rho}')] \} \\ &= a^{\text{in}}[\boldsymbol{\rho}(\boldsymbol{\rho}')] \tilde{a}^{\text{out}}[\boldsymbol{\kappa}(\boldsymbol{\rho}')] V_\ell[\boldsymbol{\rho}(\boldsymbol{\rho}'), z_0] \exp \{i\psi^{\text{OPL}}[\boldsymbol{\rho}(\boldsymbol{\rho}')] \} . \end{aligned} \quad (110)$$

This expression constitutes an elegant physical-optics outcome that the geometric polarization ray tracing operator can be entirely derived from the unified free space propagation operator. The approximation used in this process can be mathematically demonstrated and numerically examined by the Fourier transformation. At the end, a short physical interpretation for different terms in the Eq. (110) is given:

- $a^{\text{in}}[\boldsymbol{\rho}(\boldsymbol{\rho}')] \tilde{a}^{\text{out}}[\boldsymbol{\kappa}(\boldsymbol{\rho}')]$ : scaling factor, Jacobian determinant of coordinate transformation.
- $V_\ell[\boldsymbol{\rho}(\boldsymbol{\rho}'), z_0]$ : pointwise mapping of the initial field.
- $\psi^{\text{OPL}}[\boldsymbol{\rho}(\boldsymbol{\rho}')]$ : phase modulation, corresponding to the optical path length.

The meaning of the pointwise propagation operator resides in the fact that the structure of the formula pleasingly reveals the anatomy of the propagation. It lays bare the different physical phenomena that are the sole preserve of a rigorous physical-optics approach, such as, perhaps most poignantly, the Gouy phase [113].

#### 4.3.2 Paraxial domain operator: Fresnel integral

If we assume a paraxial input field in  $z = z_0$ , the beam consists of plane waves with only small inclinations with respect to the optical axis. From that follows the Taylor expansion at the origin  $\boldsymbol{\kappa} = 0$  in the spatial-frequency domain as

$$\begin{aligned} \check{k}_z(\boldsymbol{\kappa}) &= \sqrt{k_0^2 \check{n}^2 - \boldsymbol{\kappa}^2} \\ &= k_0 \check{n} - \frac{1}{2} \frac{\boldsymbol{\kappa}^2}{k_0 \check{n}} + \delta(\boldsymbol{\kappa}) , \end{aligned} \quad (111)$$



where  $\delta(\kappa)$  indicates the remaining part of the Taylor expansion, which would be neglected in the paraxial approximation [68, 114]. Remarkably, the paraxial approximation implies that the bandwidth of the given spectrum is narrow enough so that we can omit the remaining term. Here, we don't make any approximation. Then, substituting Eq. (111) into Eq. (69) provides

$$V_\ell(\rho', z') = \exp(ik_0\check{n}\Delta z) \mathcal{F}_\kappa^{-1} \left\{ \tilde{V}_\ell(\kappa, z_0) \exp[i\delta(\kappa) \Delta z] \exp\left(-i\frac{\Delta z}{2k_0\check{n}}\kappa^2\right) \right\}. \quad (112)$$

We can define the modified spectrum in the spatial frequency domain as

$$\tilde{V}_\ell^m(\kappa, z_0) = \tilde{V}_\ell(\kappa, z_0) \exp[i\delta(\kappa) \Delta z]. \quad (113)$$

Afterward, the inverse SFT can be used to replace the regular Fourier transform of the spectrum  $\tilde{V}_\ell^m(\kappa, z_0) \exp\left(-i\frac{\Delta z}{2k_0\check{n}}\kappa^2\right)$ . Expanding the inverse semi-analytical Fourier transform equation, we concluded the mathematical expression of the quasi-paraxial domain propagation operator:

$$\begin{aligned} V_\ell(\rho', z') &= \exp(ik_0\check{n}\Delta z) \mathcal{F}_\kappa^{-1, \text{semi}} \left[ \tilde{V}_\ell^m(\kappa, z_0) \exp\left(-i\frac{\Delta z}{2k_0\check{n}}\kappa^2\right) \right] \\ &= -\frac{ik_0\check{n}}{\Delta z} \exp\left[ik_0\check{n}\Delta z + i\frac{k_0\check{n}}{2\Delta z}(\rho')^2\right] \mathcal{F}_{\tilde{\beta}} \left\{ \mathcal{F}_\kappa^{-1} [\tilde{V}_\ell^m(\kappa, z_0)] \exp\left(i\frac{k_0\check{n}}{2\Delta z}\rho^2\right) \right\} \end{aligned} \quad (114)$$

with

$$\tilde{\beta} = \frac{k_0\check{n}}{\Delta z} \rho'. \quad (115)$$

Here,  $\mathcal{F}_{\tilde{\beta}}$  denotes the Fourier transform operation. Since we don't make any approximation during the derivation process, the quasi-paraxial domain operator is as rigorous as the SPW operator. Comparing Eq. (114) with the SPW formula, we can see that the quadratic phases of the propagating kernel are extracted and excluded from the Fourier operations. Because of the analytical handling of the quadratic phases, in some suitable situations, the required sampling points for the residual field is much fewer than the original field. Especially in paraxial cases, the remaining phase  $\exp[i\delta(\kappa) \Delta z]$  almost be zero that the numerical effort of three FFT operations are not problem. Then, in the case of a medium divergent beam, the remaining phase cannot be neglected but should still require less sampling than the original propagating phase kernel  $\exp[i\check{k}_z(\kappa) \Delta z]$ . In that situation, the quasi-paraxial domain operator can also ensure the improvement of the computational performance while maintains the level of accuracy. At the

end, when the input field is non-paraxial, since the remaining phase becomes huge and leads to massive sampling and computational effort, the proposed approach cannot bring any improvement.

*Standard Fresnel integral as a special case*

Let us consider the dispersion relation of Eq. (111) and employ the paraxial approximation. The resulting equation can be written as

$$\begin{aligned}\check{k}_z(\boldsymbol{\kappa}) &= \sqrt{k_0^2 \check{n}^2 - \boldsymbol{\kappa}^2} \\ &\approx k_0 \check{n} - \frac{1}{2k_0 \check{n}} \boldsymbol{\kappa}^2.\end{aligned}\quad (116)$$

Next, inserting Eq. (116) into the SPW formula of Eq. (69) yields

$$V_\ell(\boldsymbol{\rho}', z') \approx \exp(ik_0 \check{n} \Delta z) \mathcal{F}_\kappa^{-1} \left[ \tilde{V}_\ell(\boldsymbol{\kappa}, z_0) \exp\left(-i \frac{\Delta z}{2k_0 \check{n}} \boldsymbol{\kappa}^2\right) \right]. \quad (117)$$

To solve our problem, we need to perform an inverse Fourier transform, whose object becomes the sum of the input spectrum and an additional quadratic phase term. Here, we can directly utilize the conclusion of the semi-analytical Fourier transform. According to Eq. (21), the free space propagation formalism can be simplified as

$$\begin{aligned}V_\ell(\boldsymbol{\rho}', z') &\approx \exp(ik_0 \check{n} \Delta z) \mathcal{F}_\kappa^{-1, \text{semi}} \left[ \tilde{V}_\ell(\boldsymbol{\kappa}, z_0) \exp\left(-i \frac{\Delta z}{2k_0 \check{n}} \boldsymbol{\kappa}^2\right) \right] \\ &= -\frac{ik_0 \check{n}}{\Delta z} \exp\left[ik_0 \check{n} \Delta z + i \frac{k_0 \check{n}}{2\Delta z} (\boldsymbol{\rho}')^2\right] \mathcal{F}_{\tilde{\beta}} \left[ V_\ell(\boldsymbol{\rho}, z_0) \exp\left(i \frac{k_0 \check{n}}{2\Delta z} \boldsymbol{\rho}^2\right) \right]\end{aligned}\quad (118)$$

with

$$\tilde{\beta} = \frac{k_0 \check{n}}{\Delta z} \boldsymbol{\rho}'. \quad (119)$$

The propagation operator of Eq. (118) is referred to as Fresnel diffraction integral. It involves only one Fourier integral and the resulting expression becomes more compact. It is of great value in optical modeling because of some numerical advantages compared to the rigorous SPW and the Rayleigh-Sommerfeld integral. However, to obtain the Fresnel integral, we made the assumption, i.e., the paraxial approximation of Eq. (116). In contrast to the Fresnel integral, the quasi-paraxial domain propagation operator is rigorous and enables fast evaluation of the propagation problem in both paraxial and medium divergent situations.

Table 11: Physical interpretation of different propagation operators: selection and combination of the Fourier transform techniques

Propagation integral	Fourier transform	Inverse Fourier transform
SPW operator	FFT	IFFT
Fresnel integral	FFT	ISFT
Far-field integral	FFT	IHFT of $\tilde{\psi}^{\text{far}}(\kappa)$
Debye integral	HFT of $\psi^{\text{sph}}(\rho)$	IFFT
generalized Far-field integral	FFT	IHFT
generalized Debye integral	HFT	IFFT
pointwise propagation operator	HFT	IHFT

Finally, in Table 11, we summarized the characteristics of all presented propagation operators in terms of the combination of the Fourier transform techniques.

#### 4.4 NUMERICAL EXAMPLES

The numerical implementation for the unified free space propagation operator and some other diffraction integrals has been done in the physical-optics modeling and design software VirtualLab Fusion. In what follows, we present several examples to demonstrate the accuracy and performance of the proposed unified propagation approach.

To have a clear-cut discussion, we would like to emphasize that, for each simulation example, we compare the results of the unified free space propagation operator with the standard diffraction integral. For instance, in the case of the focusing system, we investigate the difference between standard Debye integral and the proposed unified propagation operator. The following expression provides the deviation between the reference and the testing approach:

$$\sigma := \frac{\sum_{x,y} |V^{\text{ref}}(\rho) - V^{\text{test}}(\rho)|^2}{\sum_{x,y} |V^{\text{ref}}(\rho)|^2}, \quad (120)$$

Table 12: Simulation parameters of the aberrant phase for the example presented in Section 4.4.1.

Name & Type	Mathematical Expression	Scaling Factor
Coma X	$Z_3^1(r, \theta) = \sqrt{8}(3r^3 - 2r) \cos \theta$	$c_3^1 = 0 \sim 5\lambda$
Secondary Astigmatism Y	$Z_4^{-2}(r, \theta) = \sqrt{10}(4r^4 - 3r^2) \sin 2\theta$	$c_4^{-2} = 0 \sim 5\lambda$
Secondary Trefoil X	$Z_6^4(r, \theta) = \sqrt{14}(6r^6 - 5r^4) \cos 4\theta$	$c_6^4 = 0 \sim 5\lambda$

where the reference  $V^{\text{ref}}(\rho)$  is typically provided by the rigorous SPW technique and  $V^{\text{test}}(\rho)$  denotes the result obtained by the unified free space propagation operator or standard diffraction integral, respectively.

#### 4.4.1 Focusing of an aberrant field

The initial field used in the first example is linearly  $E_x$ -polarized, with a wavelength of 532 nm. The amplitude is distributed uniformly and truncated by an aperture with a circular shape and a diameter of 6 mm. A convergent spherical phase with a radius of curvature  $R = -100$  mm, is superimposed on this field. We can calculate the corresponding numerical aperture (NA) according to these parameters;  $\text{NA} = n \sin \theta \approx 0.03$ . Based on the initial configuration, we continue by superimposing different types of Zernike aberrant phases on it. The variable being tested would be the type of Zernike aberration and its weighting factor. We selected three types of aberrant phase, which are described in the form of Zernike polynomials,

$$\psi^{\text{Zer}}(\rho) = k \sum_{m=0}^M \sum_{n=0}^N c_n^m Z_n^m(r, \theta), \quad (121)$$

where  $r = \frac{|\rho|}{\rho_{\max}}$  and  $\theta = \arctan(\frac{y}{x})$ ;  $c_n^m$  denotes the coefficients of the corresponding Zernike term. In Table 12, we present the mathematical expression of different Zernike aberrant phases and the range of their scaling factor.

For the following results we have tested the accuracy of the unified free space propagation operator by comparing it with the SPW solution. In all cases we found values of  $\sigma < 0.02\%$ , which demonstrates the high accuracy of the proposed approach. In the subsequent part of Section 4.4.1 we compare the standard

Debye integral and the unified free space propagation operator via  $\sigma$  as defined in Eq. (120).

In Fig. 22, simulation results for secondary trefoil X with the scaling factor  $c_4^{-2} = 5\lambda$  are shown. Comparing, via a naked-eye observation, the obtained amplitude distributions of the  $E_x$  component in sub-figures (a) and (d), it is not possible to detect the difference, with a mathematical calculation revealing a standard deviation lower than 0.05 %. However, when we turn our attention to

unified free space propagation operator

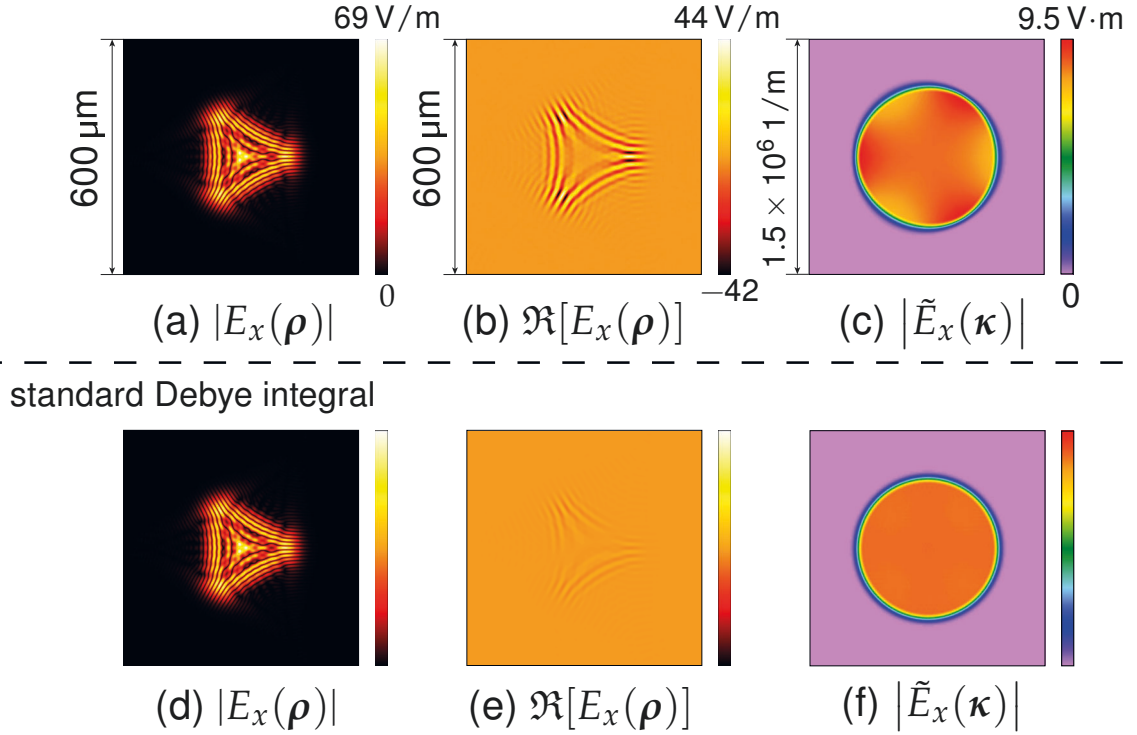


Figure 22: Comparison of accuracy between the unified free space propagation operator and the standard Debye integral for the focusing of a convergent field with a secondary trefoil X aberrant phase (SPW results are not shown, since the deviation between the unified propagation operator result and the rigorous SPW technique is just 0.02 %). Simulation results for both approaches are respectively shown in the upper and lower rows. Panels (a) and (d) present the amplitude distribution of the  $E_x$  component at the focal plane; panels (b) and (e) present the real part of the  $E_x$  component; panels (c) and (f) show the amplitude distribution of the  $\tilde{E}_x$  component at the focal plane (i.e. the Fourier transform of the output field).

the full complex amplitude (including phase), the standard deviation ascends to 25%. The differences in this case, we must conclude, are mainly located in the phase. This effect can be observed by the comparison of the real part of the  $E_x$  component. As shown in Fig. 22 (b) and (e), where the same scaling is used, the unified free space propagation operator result exhibits a higher contrast. The

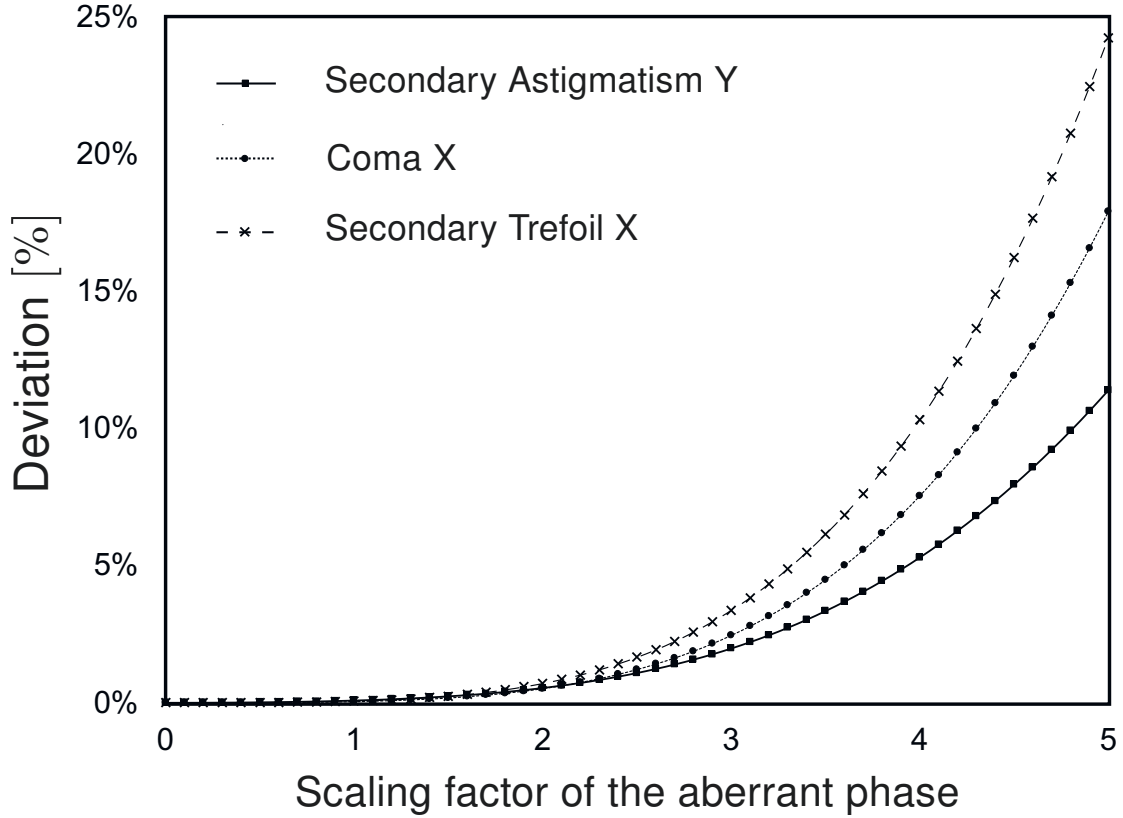


Figure 23: Comparison of accuracy between the unified free space propagation operator and the standard Debye integral for the simulation task of calculating the focal field for a convergent field with different single types of aberrant phase. The abscissa records the scaling factor – i.e., the factor  $C_n^m$  in Tab. 12 – of the corresponding Zernike term, while the ordinate marks the deviation between the two approaches, with the unified free space propagation operator as reference. It should be noted that in this experiment, the deviation between the unified free space propagation operator result and the rigorous SPW technique is just 0.02 %.

high accuracy of the unified propagation operator can be explained by something we already covered when we presented the two approaches used here: the

unified free space propagation operator uses a more general extracted wavefront phase than the standard one. In Fig. 22 (c) and (f), the Fourier transform of the output field on the focal plane for both approaches is given. In contrast to the unified free space propagation operator, the resulting spectrum of the standard Debye integral presents a uniform amplitude distribution. This is due to the fact that, considering we are dealing with a relatively low-NA situation, the point-wise mapping relation generated by the primary spherical phase employed in the standard Debye integral, in Eq. (80), approximately becomes a linear mapping. The experimental results coincide well with our theoretical expectations.

In a further investigation we did a full series of comparisons with different aberrant phases. The curves corresponding to the standard deviation between the two approaches are presented in Fig. 23. Three types of aberrant phase are superimposed, individually and in turns, onto the given input field. Even though the variation rate of the standard deviation error is different depending on the type of aberrant phase, the resulting curves reveal the same tendency. At the weak-aberration end of the scale or, in other words, for the ideal focusing system, both approaches provide an identical result. Then, as the scaling factor of the aberrant phase increases, the deviation between the two approaches grows fast. That is, when the aberration of the focusing system is too strong to be neglected, the standard Debye integral cannot predict a correct result at the focal plane. On the other hand, the high accuracy and the validity of the unified free space propagation operator was tested in advance, as mentioned before ( $\sigma < 0.02\%$ ).

#### 4.4.2 Propagation of an aberrant divergent wave

Besides the light focusing system, another essential propagation scenario is to propagate the divergent field from its focal region to the far-field region. First of all, let us briefly introduce the specification of the experimental setup. The electromagnetic field, with a wavelength of 532 nm, is initialized at a distance of  $z = -40$  mm away from the input plane. It is linearly polarized in  $E_x$  and its

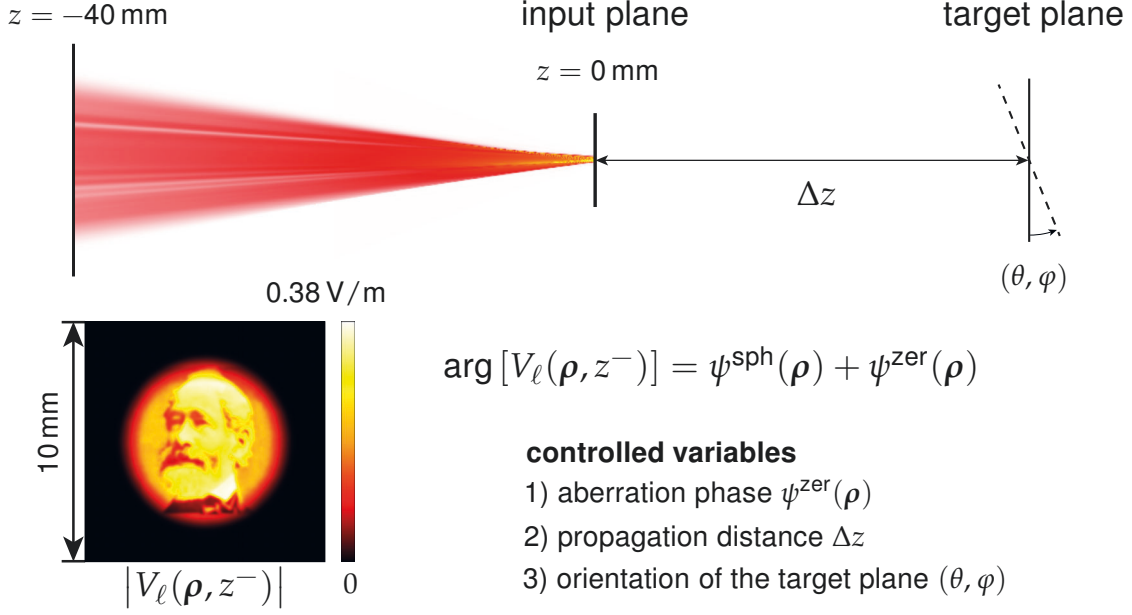


Figure 24: Illustration of the simulation task: propagation of an aberrant divergent beam, from the focal region to an arbitrarily oriented target plane. The testing field is initialized on the plane  $z = -40$  mm. The bottom left panel shows the amplitude distribution of  $E_x$  component on the initial plane. The phase on this plane consists of two parts, the fixed spherical phase  $\psi^{\text{sph}}(\boldsymbol{\rho})$  of a spherical radius  $R = -40$  mm and the varying aberration phase  $\psi^{\text{zer}}(\boldsymbol{\rho})$ .

amplitude distribution  $|V_{\ell}(\boldsymbol{\rho}, z^{-})|$  is modulated as a photo of Carl Zeiss. The phase distribution is specified by

$$\arg [V_{\ell}(\boldsymbol{\rho}, z^{-})] = \psi^{\text{sph}}(\boldsymbol{\rho}) + \psi^{\text{zer}}(\boldsymbol{\rho}) . \quad (122)$$

In our configuration, the divergent spherical phase  $\psi^{\text{sph}}(\boldsymbol{\rho}) = -k_0 \tilde{n} \sqrt{\boldsymbol{\rho}^2 + R^2}$  is fixed with a constant spherical radius of  $R = -40$  mm while we set the aberration phase  $\psi^{\text{zer}}(\boldsymbol{\rho})$  as one controlled variable. By modifying the type and weighting coefficients of the Zernike phase, we can adjust the aberration in this system. The complete light field should be numerically sampled on the initial  $xy$ -plane. By performing the rigorous SPW operator, we obtain the input field on the plane  $z = 0$  mm. Before we investigate the propagation from the focal region to the target plane, we need to set another two controlled parameters, the propagation distance  $\Delta z$  and the orientation of the target plane  $(\theta, \phi)$ .



Table 13: Simulation parameters of the aberrant phase  $\psi^{\text{zer}}(\rho)$  for the first example presented in Section. 4.4.2.

Name & Type	Mathematical Expression	Value
Spherical aberration	$Z_4^0(r, \theta) = \sqrt{5}(6r^4 - 6r^2 + 1)$	$c_4^0 = 0 \sim 10\lambda$
Tertiary astigmatism y	$Z_6^{-2} = \sqrt{14}(15r^6 - 20r^4 + 6r^2) \sin 2\theta$	$c_2^{-2} = 0 \sim 10\lambda$
Coma X	$Z_3^1 = \sqrt{8}(3r^3 - 2r) \cos \theta$	$c_3^1 = 0 \sim 10\lambda$

#### *Accuracy vs. the single aberrant phase*

In the first example, we would like to investigate the influence of the aberration phase on the level of accuracy for both the unified free space propagation operator and the standard far-field integral. Firstly, let us clarify the configuration of the experimental setup for this simulation task: (1) only consider the propagation between parallel planes, i.e., setting the orientation of the target plane to  $(\theta, \varphi) = (0^\circ, 0^\circ)$ ; (2) fix the propagation distance as  $\Delta z = 60 \text{ mm}$  (the target plane doesn't locate in the far-field region); (3) select some single Zernike phase and employ the comparison.

We selected three types of single Zernike aberrant phase and individually superimposed them into the light field. The corresponding mathematical expression and scaling coefficients are described in Table. 13. In the following tests, we firstly compared the unified free space propagation operator result with the rigorous SPW solution. For all cases, the deviation between them is smaller than 0.01%. The fact proves that when the target plane located in the so-called homeomorphic field zone, the HFT is accurate enough to replace the rigorous FFT. Next, in the subsequent part, we would concentrate on the deviation between the unified free space propagation operator and the standard far-field integral.

In Fig. 25, the curves of the standard deviation between two approaches varying with the scaling coefficients of the aberrant phase are presented. We can see that all three types of aberrant phases reveal the same tendency: (1) For the aberration-free or tiny aberration cases, the standard far-field integral can also provide accurate result. (2) As the scaling factor of the aberration phase grows, the deviation between the two approaches increases rapidly. These experimental behaviors reflect sufficiently the influence of the approximation used in the

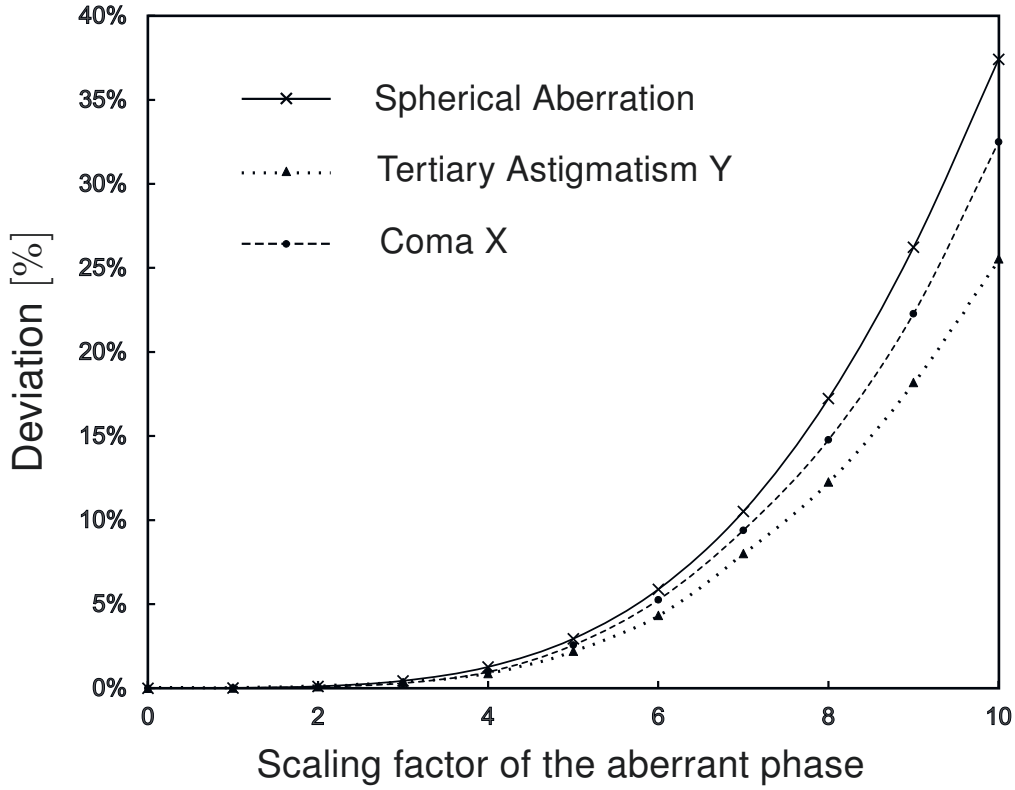


Figure 25: Comparison of accuracy between the unified free space propagation operator and the standard far-field integral for the first example presented in Section. 4.4.2. The abscissa records the scaling factor of the aberrant phase  $\psi^{\text{zer}}(\rho)$ , while the ordinate marks the deviation between the two approaches, with the generalized far-field integral as reference. It should be noted that in this experiment, the deviation between the generalized far-field integral result and the rigorous SPW technique is lower than 0.01%.

derivation of two approaches. In the unified propagation operator, not only the primary spherical phase but also all aberration phases are taken into account in the mapping of the inverse homeomorphic Fourier transform. But, the standard far-field integral consider just the primary spherical phase so that the inverse homeomorphic Fourier transform fails fast in the situation of a strong aberrant phase.

### *Accuracy vs. the propagation distance*

In the first example, we have investigated the influence of three single Zernike phase to the level of accuracy. While, in the second set of experiments, we would

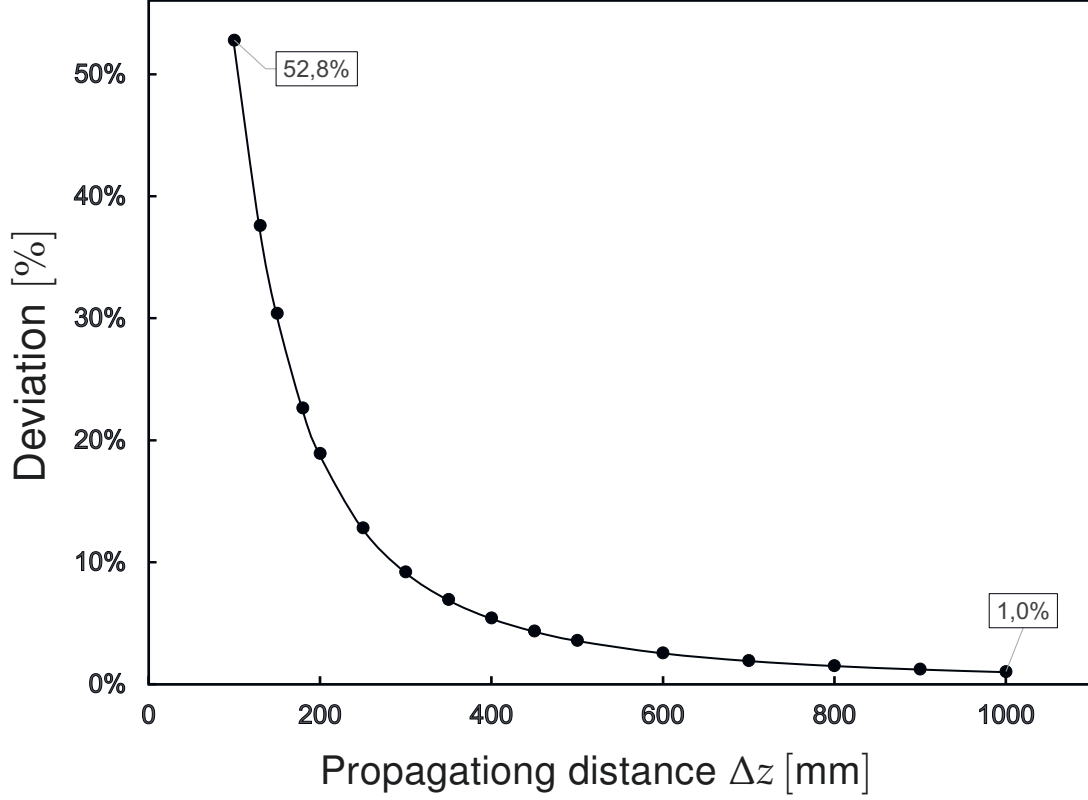


Figure 26: Comparison of the accuracy of the unified free space propagation operator and the standard far-field integral for second example presented in Section 4.4.2. The abscissa records the propagation distance along the  $z$ -axis, while the ordinate marks the deviation of two methods, with the unified free space propagation operator as reference.

like to turn our attention to another parameter, the propagation distance. Similarly, let us clarify the configuration of the experimental setup for this simulation task: (1) only consider the propagation between parallel planes, i.e., setting the orientation of the target plane to  $(\theta, \varphi) = (0^\circ, 0^\circ)$ ; (2) specify the aberrant phase  $\psi^{\text{zer}}(\rho)$  and set it to be constant; (3) customize the value of propagation distance  $\Delta z$ .

Table 14: Simulation parameters of the primary spherical phase and the aberrant phase for the second example presented in Section. 4.4.2.

Name & Type	Mathematical Expression	Value
Spherical phase	$\psi^{\text{sph}}(\boldsymbol{\rho}) = -k_0 \tilde{n} \sqrt{\boldsymbol{\rho}^2 + R^2}$	$R = -40 \text{ mm}$
Tilt X	$Z_1^1(r, \theta) = 2r \sin \theta$	$c_1^1 = 3\lambda$
Astigmatism Y	$Z_2^{-2}(r, \theta) = \sqrt{6}r^2 \sin 2\theta$	$c_2^{-2} = 5\lambda$
Spherical aberration	$Z_4^0(r, \theta) = \sqrt{5}(6r^4 - 6r^2 + 1)$	$c_4^0 = -6\lambda$
Trefoil Y	$Z_3^{-3}(r, \theta) = \sqrt{8}r^3 \sin 3\theta$	$c_3^{-3} = 8\lambda$
Tetrafoil X	$Z_4^4(r, \theta) = \sqrt{10}r^4 \sin 4\theta$	$c_4^4 = -8\lambda$
Tertiary Coma X	$Z_7^1(r, \theta) = 4(35r^7 - 60r^5 + 30r^3 - 4r) \cos \theta$	$c_7^1 = 10\lambda$

Simulation parameters for the phase of the light field  $\arg|V_\ell(\boldsymbol{\rho}, z^-)|$  on the initial plane  $z = -40 \text{ mm}$  are presented in Table 14. And, the propagation distance is set in the range of  $[100 \text{ mm}, 1 \text{ m}]$ . As same as the first experiment, for all propagation distances in the definition domain, the unified free space propagation operator can predict exactly the same result as the reference SPW operator. In contrast, the standard far-field integral results, more or less, are distinct from the reference. To compare the accuracy of the unified propagation approach and the standard far-field integral, we calculated the deviation between them of different propagation distances. And, the curve of deviation varying with the propagation distance is presented in Fig. 26. The experimental result coincides very well with our expectation that the deviation drops as the propagation distance increases. It means that the standard far-field integral performs well for the propagation of the aberrant field in the far-field region. From the physical point of view, it is because the propagation kernel will attenuate the weight of the wavefront phase  $\tilde{\psi}(\boldsymbol{\kappa})$  in Eq. (87) as propagation distance becomes larger and larger. Even though the aberrant phase becomes less critical in the case of a considerable distance, we cannot neglect its influence on the homeomorphic Fourier transform. Thus, there is still a 1% difference in the situation of  $\Delta = 1 \text{ m}$ .

#### 4.4.3 Propagation of the light field to the inclined planes

In Section 4.1.2, we discussed how to extend the free space propagation operator deal with the situation of arbitrarily oriented target planes. Afterward, in Sec-

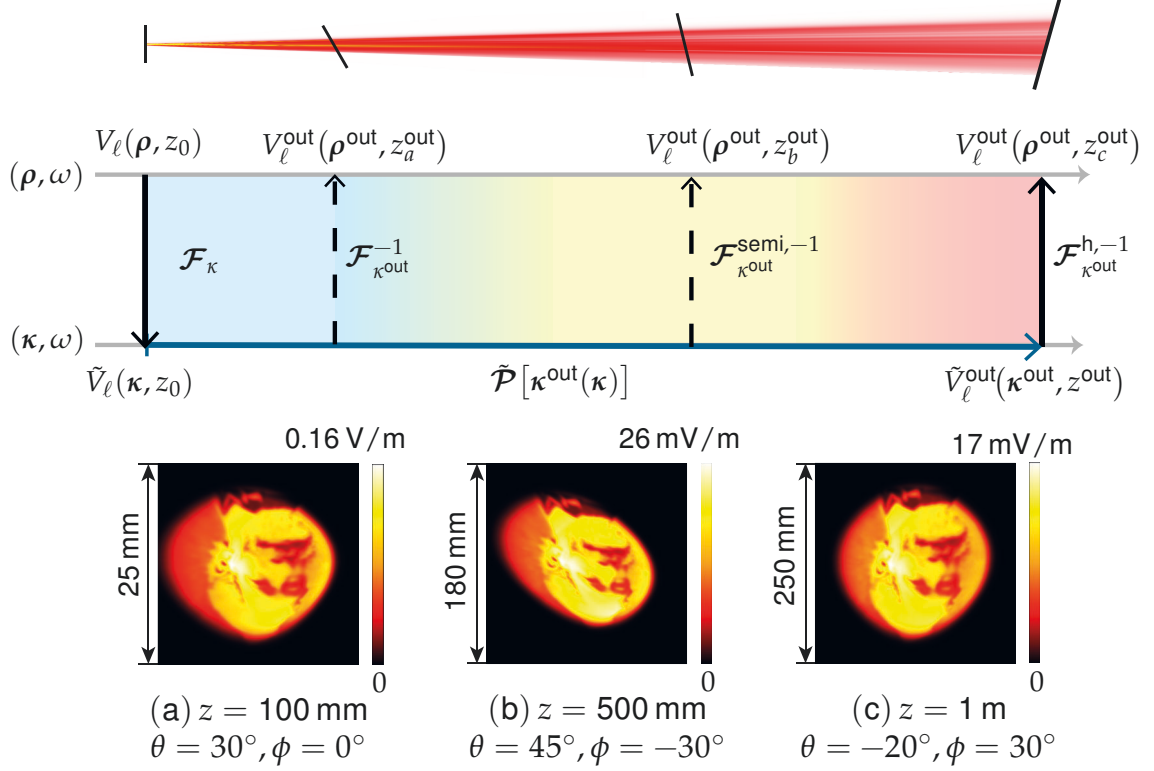


Figure 27: Field distribution computed by the unified free space propagation operator at three different  $z$  positions and for different inclination angles of the plane of observation. The corresponding field tracing diagram indicates the automatic selection of Fourier transform techniques in different field zones.

tion 4.1.3, we explained the automatic selection rules of the Fourier transform techniques. For the demonstration, we use the same input field presented in the last example and place the screen at three different distances as well as different inclination angles along the optical axis. Simulation results by the unified free space propagation operator are presented in Fig. 27. In addition, the corresponding inverse Fourier transform techniques at different field regions are also denoted in the field tracing diagram. In all cases, we verified the accuracy of the proposed unified propagation operator by comparing it with the rigorous SPW method from Eq. (120) and found  $\sigma \approx 0.02 \%$ .



## SUMMARY AND OUTLOOK

---

The Fourier transform operation lays the foundation for the fast physical-optics modeling of sophisticated systems. By performing a Fourier transform, we can move between the spatial ( $x$ ) and the spatial frequency ( $k$ ) domain. The performance of its implementation determines the efficiency of the simulation for the whole system. In this work, we proposed two advanced Fourier transform techniques: the semi-analytical Fourier transform (SFT) and the homeomorphic Fourier transform (HFT).

Both the SFT and the HFT allow us to carry out the Fourier transform efficiently. The SFT is a rigorous approach without approximation. The idea of this method is to extract the quadratic phase from the input field/spectrum with the help of a numerical evaluation technique, e.g., the Levenberg-Marquardt method. Then, the semi-analytical Fourier transform can be used to replace the regular FFT of the fully sampled field by two FFTs of complex functions that require significantly fewer sampling points. The sampling issue is entirely dependent on the residual field so that, in comparison to the regular FFT, the numerical effort is reduced dramatically.

On the other hand, the HFT is a fast, pointwise, but approximated Fourier transform operation to deal with field components presenting strong wavefront phases. This approximate approach is inspired by the method of stationary phase, but formulated in purely mathematical form. In regard to the implementation, we use a hybrid sampling strategy to deal separately with the smooth wavefront phase  $\psi(\boldsymbol{\rho})$  and the remnant of the field,  $U_\ell(\boldsymbol{\rho})$ . Since we avoid sampling the wrapped phase  $\exp[i\psi(\boldsymbol{\rho})]$ , the decline in computational effort is significant,  $N(U) \ll N(V)$ . We present the full theoretical derivation and the validity conditions that would support the application of this method to more pragmatic scenarios. Furthermore, to develop a robust algorithm for more practical tasks, we extend the HFT to cover fields with a non-bijective wavefront phase. However, the regularization of the mapping relation results in a dislocation in the

spectrum position and leads to an inevitable error. So far, we have investigated the error numerically and compared it against a given accuracy threshold. But there is no alternative approach to deal with the Fourier transform of a field with a strong non-bijective wavefront phase efficiently. As a next step, we would like to pursue not only efficient but also rigorous solutions for that specific case.

In total, three advanced Fourier transform algorithms (FFT, SFT, and HFT) are available. To demonstrate their vast potential in physical-optics modeling, we apply them to an essential modeling scenario, namely free space propagation, and investigate how to realize improvements in performance, with the help of the aforementioned tools. As a result, we concluded a unified free space propagation operator. The derivation follows the angular-spectrum-of-plane-waves (SPW) approach, includes the propagation between inclined planes, and adopts an automatic selection strategy of the Fourier transform techniques. Specifically, the propagation kernel (including the handling of the non-parallel planes) in the  $k$  domain is always a pointwise operation. Thus, in different propagation scenes, by selecting the most efficient and accurate Fourier transform techniques to carry out the transformation between the two domains, we can ensure the numerical effort is minimized. For the sake of in-depth understanding, from the point of view of the selected and combined Fourier transform pairs, we generalize and re-interpret several well-known diffraction integrals and propagation operators. For instance, in the case of a focusing system, we can deduce the generalized Debye integral from the unified propagation operator, while the standard Debye integral can be understood as a particular case of the generalized Debye integral formula. Remarkably, the analysis method and strategy of the unified operator are not confined to the problem of light propagation. It is totally justified to employ the same logic to solve other modeling scenarios.



## APPENDIX

---

### A.1 HOMEOMORPHISM CONDITION FOR THE SMOOTH PHASE FUNCTION

Let us consider two subsets  $X \subseteq \mathbb{R}^2$  and  $K \subseteq \mathbb{R}^2$ . A mapping function between two such subsets can mathematically be described as  $f : \rho \in X \Rightarrow f(\rho) = \kappa \in K$ , where  $\rho = (x, y)$  and  $\kappa = (k_x, k_y)$ . One such mapping function is precisely the vector mapping relation effected by the homeomorphic Fourier transform, which establishes a link between the two domains via the gradient of the wave-front phase function,

$$\kappa = f(\rho) = \nabla \psi(\rho) . \quad (\text{A-123})$$

It is made evident in the body of the work above that to identify whether this vector mapping constitutes a homeomorphism or not is key when it comes to applying the homeomorphic Fourier transform. In this section of the appendix we shall analyze this condition in a more in-depth manner from the strictly mathematical point of view, with a view to ascertaining a valid, easy-to-check criterion.

Let us then begin from the topological definition of a homeomorphism: a continuous bijection whose inverse is also continuous. A bijection describes a function which pairs each element contained in the domain  $X$  with exactly one element in the domain  $K$  and which leaves no element unpaired. For one-dimensional cases, it has been proved by Kenneth George that a strictly monotone real function is bijective [115]. Mathematically, the strict monotonicity of a one-dimensional function entails its first derivatives being all non-negative or non-positive.

Working from the one-dimensional result, we investigate the extrapolation of the criteria to the two-dimensional case. First, let us reformulate the vector mapping functions in Eq. A-123 in terms of their scalar components, thus:

$$\kappa = (k_x, k_y) := \begin{cases} k_x = \frac{\partial}{\partial x} \psi(\rho) = \psi_x(\rho) , \\ k_y = \frac{\partial}{\partial y} \psi(\rho) = \psi_y(\rho) . \end{cases} \quad (\text{A-124})$$

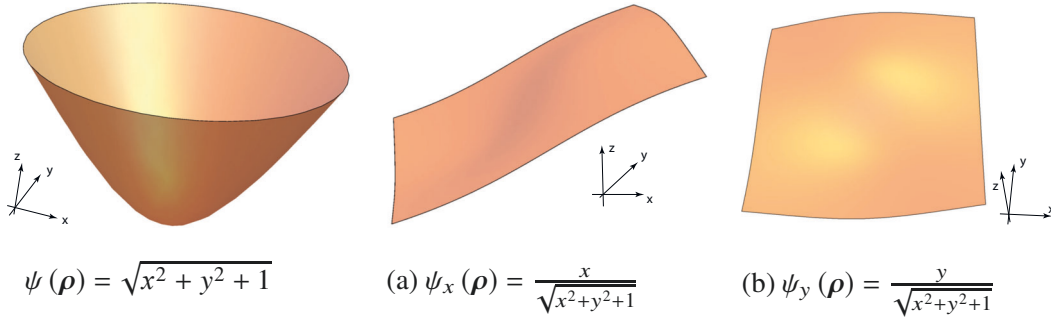


Figure 28: Spherical phase function  $\psi(\rho)$  and its partial derivative functions.

In what follows the derivation process is demonstrated for the example of a spherical function. As shown in Fig. 28, each of the two components of the mapping vector  $(k_x, k_y)$  corresponds, respectively, to a parametric surface. It is evident that, in order to prove the bijection, we must ensure that for two different positions  $\rho_1 \neq \rho_2$  in the definition domain  $X$ , the corresponding mapping vectors are also different,  $\kappa(\rho_1) \neq \kappa(\rho_2)$ .

Let us then pick out a random, arbitrary position  $\rho_i$  from the domain  $X$ . The corresponding mapping vector  $\kappa_i = (k_{xi}, k_{yi})$  can be obtained from the application of Eq. A-124. Next, fixing the  $k_x$  component so that henceforth it remains constant, we obtain a 3D parametric curve which corresponds to the intersection of  $\psi_x(\rho)$  and the plane  $\psi_x(\rho) = k_{xi}$ . As can be seen in Fig. 29, it is possible to introduce a new variable  $t_{\min} < t < t_{\max}$  to describe this parametric curve in the form  $\rho(t) = [x(t), y(t)] = \psi_x^{-1}(k_{xi})$  where  $\rho(t_{\min})$  and  $\rho(t_{\max})$  are the two end points of the curve.

The curve  $\rho(t)$  is obviously a subset of the definition domain  $X$ , whose mapping vectors all have the same  $k_x$  component. Therefore, if we are to have a bijection, it is inescapable that the  $k_y$  component corresponding to the points of this curve be all different from each other, that is, that along the path  $\rho(t) =$

$[x(t), y(t)]$  no two  $k_y = \psi_y[\rho(t)]$  have the same value. Or, in other words, the one-dimensional function  $\psi_y[\rho(t)]$  is strictly monotonic. This same test can then be applied to all the dense set of  $\rho$  paths which arise from considering all possible different fixed  $k_{xi}$ . If the condition holds for all points in  $X$ , then it can be concluded that the mapping in question is indeed a homeomorphism.

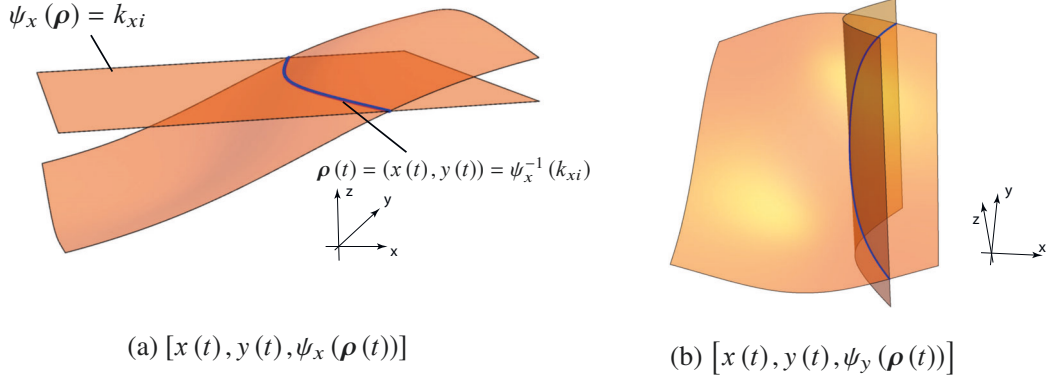


Figure 29: First derivatives of the spherical phase function: (a) The blue curve corresponds to the intersection of the first derivative of the spherical phase function  $\psi_x(\rho)$  with the constant plane given by  $\psi_x(\rho) = k_{xi}$ . (b) Along the path  $\rho(t) = [v(t), y(t)]$ , we can find another parametric curve on the surface  $\psi_y(\rho)$ .

Before we move on to the rigorous demonstration, let us list some important arguments and summarize the most fundamental concepts discussed up to this point:

- (i) A one-dimensional function is bijective if it is strictly monotonic, and that is true if and only iff the first derivatives are all non-negative or non-positive.
- (ii) We say that  $\psi(\rho)$  is a smooth function when the derivatives (of all orders) are continuous and differentiable, i.e. when  $\psi(\rho) \in C^\infty$ .
- (iii) The condition  $\psi_{xy}^2(\rho) - \psi_{xx}(\rho) \psi_{yy}(\rho) \neq 0$  implies that  $\psi_{xy}(\rho)$  and  $\psi_{xx}(\rho) \psi_{yy}(\rho)$  cannot be 0 simultaneously.
- (iv) The mapping from the scalar variable  $t$  to the vector  $\rho$ ,  $t \rightarrow \rho(t)$ , is bijective.

The  $\psi_x$  component is a constant along the intersection parametric curve. Therefore, we have

$$\frac{d\psi_x[x(t), y(t)]}{dt} = \psi_{xx} \frac{dx}{dt} + \psi_{xy} \frac{dy}{dt} = 0. \quad (\text{A-125})$$

Additionally, we can write

$$\frac{d\psi_y[x(t), y(t)]}{dt} = \psi_{xy} \frac{dx}{dt} + \psi_{yy} \frac{dy}{dt}, \quad (\text{A-126})$$

so that we can substitute Eq. A-125 into Eq. A-126, thus:

$$\frac{d\psi_y[x(t), y(t)]}{dt} = \begin{cases} \frac{\psi_{xy}^2 - \psi_{xx}\psi_{yy}}{-\psi_{xx}} \frac{dy}{dt} & , \quad \psi_{xx} \neq 0 \\ \psi_{xy} \frac{dx}{dt} & , \quad \psi_{xx} = 0 \end{cases} \quad (\text{A-127})$$

As already established, bijection requires that  $\frac{d}{dt}\psi_y$  be non-negative or non-positive throughout. To investigate how this condition applies to Eq. A-127, we consider three types of cases:

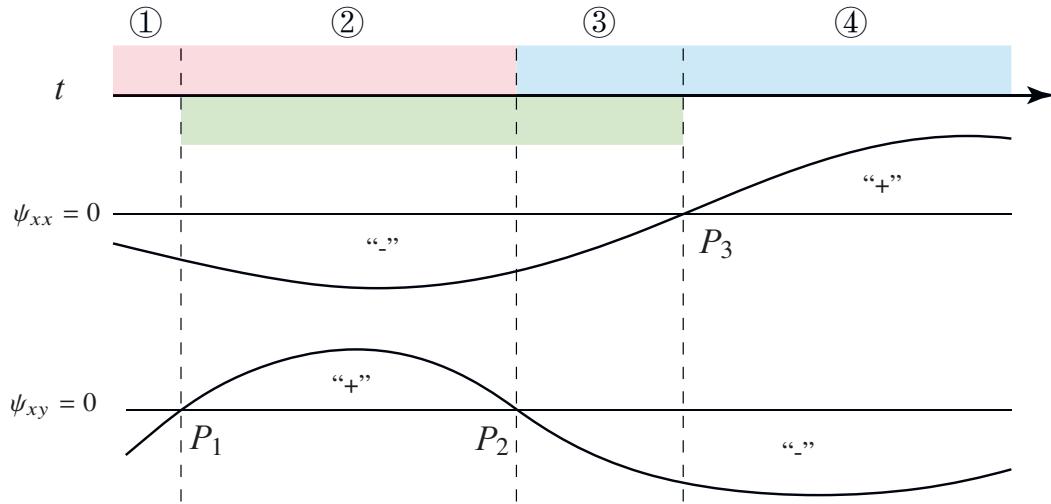


Figure 30: Example of the third kind of smooth function phase. At  $P_1$ ,  $P_2$  and  $P_3$  the second derivative of  $\psi(\rho)$  is equal to zero. Based on these three points, the definition domain is divided into four segments. Comparing the variation of the derivatives between two neighboring segments, we can analyze the continuity of the zero position.

#### 1. $\psi_{xx} = \forall \rho(t)$

- From Eq. A-125, we get  $\frac{dy}{dt} = 0$ . From this we can conclude that  $y(t) = \text{constant}$ .

- Considering condition (iv), the mapping  $t \rightarrow x(t)$  is bijective.
  - From condition (i),  $\psi_{xy}$  is non-negative or non-positive in its entirety.
  - If  $\psi_{xy}$  is negative or positive throughout, then  $\frac{d}{dt}\psi_y$  is non-negative or non-positive throughout.
2.  $\psi_{xx} \neq 0$  and  $\psi_{xy} \neq 0 \forall \rho(t)$
- From condition (ii),  $\psi_{xx}$  and  $\psi_{xy}$  are each either positive or negative throughout.
  - From Eq. A-125 we deduce that  $\frac{dy}{dt} = \frac{dx}{dt} = 0$  or that  $\frac{dy}{dt}$  and  $\frac{dx}{dt}$  are positive or negative throughout.
  - Condition (iv) preempts the possibility of  $\frac{dy}{dt} = \frac{dx}{dt} = 0$ .
  - $\frac{dy}{dt}$  is positive or negative throughout  $\rho(t)$ .
  - If  $\psi_{xy}^2 - \psi_{xx}\psi_{yy}$  is either negative or positive throughout,  $\frac{d}{dt}\psi_y$  is negative or positive throughout.
3. At some singular points  $\psi_{xx} = 0$  or  $\psi_{xy} = 0$ , e.g. curves in Fig. 30
- From condition (iii), we conclude that  $\psi_{xy}(\rho)$  and  $\psi_{xx}(\rho)$  cannot be zero simultaneously.
  - We can divide the curve  $\rho(t)$  into a series of fragments separated by the zero-valued points.
  - For each fragment, the situation is analogous to that analyzed in the second kind (point 2. above), so each fragment can be analyzed independently according to those criteria.
  - Because of the continuity – condition (i) – we can connect the result of any two neighboring fragments. We find that the term  $\frac{1}{\psi_{xx}} \frac{dy}{dt}$  is non-negative or non-positive throughout.
  - If  $\psi_{xy}^2 - \psi_{xx}\psi_{yy}$  is either negative or positive throughout, then  $\frac{d}{dt}\psi_y$  is either non-negative or non-positive throughout.

From the above analysis we can conclude that, for all three different kinds of situations, the homeomorphism condition is contained in the requirement that  $\psi_{xy}^2 - \psi_{xx}\psi_{yy}$  be either negative or positive throughout.



## BIBLIOGRAPHY

---

- [1] Bob D Guenther. *Modern optics*. OUP Oxford, 2015.
- [2] National Research Council et al. *Harnessing light: optical science and engineering for the 21st century*. National Academies Press, 1998.
- [3] Herbert Gross, Fritz Blechinger, and Bertram Achtner. *Handbook of optical systems*. Vol. 1. Wiley Online Library, 2005.
- [4] Robert Edward Fischer, Biljana Tadic-Galeb, Paul R Yoder, Ranko Galeb, Bernard C Kress, Stephen C McClain, Tom Baur, Richard Plympton, Bob Wiederhold, and Bob Grant Alastair J. *Optical system design*. Vol. 599. Cite-seer, 2000.
- [5] Andrew S Glassner. *An introduction to ray tracing*. Elsevier, 1989.
- [6] Sergei Aleksandrovich Akhmanov and S Yu Nikitin. *Physical optics*. Clarendon Press, 1997.
- [7] Daniel F Walls and Gerard J Milburn. *Quantum optics*. Springer Science & Business Media, 2007.
- [8] John Maxwell Cowley. *Diffraction physics*. Elsevier, 1995.
- [9] Julius Adams Stratton. *Electromagnetic theory*. Vol. 33. John Wiley & Sons, 2007.
- [10] Frank L Pedrotti, Leno M Pedrotti, and Leno S Pedrotti. *Introduction to optics*. Cambridge University Press, 2017.
- [11] Hwi Kim, Junghyun Park, and Byoungho Lee. *Fourier modal method and its applications in computational nanophotonics*. CRC Press, 2017.
- [12] MG Moharam and TK Gaylord. “Rigorous coupled-wave analysis of planar-grating diffraction.” In: *JOSA* 71.7 (1981), pp. 811–818.
- [13] MG Moharam and TK Gaylord. “Rigorous coupled-wave analysis of grating diffraction—E-mode polarization and losses.” In: *JOSA* 73.4 (1983), pp. 451–455.

- [14] K\_ Knop. "Rigorous diffraction theory for transmission phase gratings with deep rectangular grooves." In: *JOSA* 68.9 (1978), pp. 1206–1210.
- [15] Junuthula Narasimha Reddy. "An introduction to the finite element method." In: *New York* 27 (1993).
- [16] Olek C Zienkiewicz, Robert L Taylor, and Jian Z Zhu. *The finite element method: its basis and fundamentals*. Elsevier, 2005.
- [17] Peng Long, Wang Jinliang, and Zhu Qiding. "Methods with high accuracy for finite element probability computing." In: *Journal of computational and applied mathematics* 59.2 (1995), pp. 181–189.
- [18] Frank Wyrowski and Michael Kuhn. "Introduction to field tracing." In: *Journal of Modern Optics* 58.5-6 (2011), pp. 449–466.
- [19] Michael Kuhn, Frank Wyrowski, and Christian Hellmann. "Non-sequential optical field tracing." In: *Advanced Finite Element Methods and Applications*. Springer, 2013, pp. 257–273.
- [20] F Wyrowski. "Unification of the geometric and diffractive theories of electromagnetic fields." In: *Proc. DGaO*. 2017, A36.
- [21] Albrecht V Pfeil and Frank Wyrowski. "Wave-optical structure design with the local plane-interface approximation." In: *Journal of Modern Optics* 47.13 (2000), pp. 2335–2350.
- [22] Rui Shi and Frank Wyrowski. "Comparison of aplanatic and real lens focused spots in the framework of the local plane interface approximation." In: *J. Opt. Soc. Am. A* 36.10 (2019), pp. 1801–1809.
- [23] Jochen Brüning and Victor W Guillemin. *Mathematics Past and Present: Fourier Integral Operators*. Springer, 1994.
- [24] Joseph W Goodman. *Introduction to Fourier optics*. Roberts and Company Publishers, 2005.
- [25] James W Cooley and John W Tukey. "An algorithm for the machine calculation of complex Fourier series." In: *Mathematics of computation* 19.90 (1965), pp. 297–301.
- [26] Ronald Newbold Bracewell. *The Fourier transform and its applications*. McGraw-Hill, 1986.



- [27] Boualem Boashash. *Time-frequency signal analysis and processing: a comprehensive reference*. Academic Press, 2015.
- [28] Clare D McGillem and George R Cooper. *Continuous and discrete signal and system analysis*. Oxford University Press, USA, 1991.
- [29] Henri J Nussbaumer. "The fast Fourier transform." In: *Fast Fourier Transform and Convolution Algorithms*. Springer, 1981, pp. 80–111.
- [30] Charles Van Loan. *Computational frameworks for the fast Fourier transform*. SIAM, 1992.
- [31] HJ Landau. "Necessary density conditions for sampling and interpolation of certain entire functions." In: *Acta Mathematica* 117.1 (1967), pp. 37–52.
- [32] Ping Feng. "Universal minimum-rate sampling and spectrum-blind reconstruction for multiband signals." PhD thesis. University of Illinois at Urbana-Champaign, 1998.
- [33] Ervin Sejdic, Igor Djurovic, and Ljubisa Stankovic. "Quantitative performance analysis of scalogram as instantaneous frequency estimator." In: *IEEE Transactions on Signal Processing* 56.8 (2008), pp. 3837–3845.
- [34] Kazuyoshi Itoh. "Analysis of the phase unwrapping algorithm." In: *Applied optics* 21.14 (1982), pp. 2470–2470.
- [35] Donald J Bone. "Fourier fringe analysis: the two-dimensional phase unwrapping problem." In: *Applied optics* 30.25 (1991), pp. 3627–3632.
- [36] L Rabiner, R W Schafer, and C Rader. "The chirp z-transform algorithm." In: *IEEE transactions on audio and electroacoustics* 17.2 (1969), pp. 86–92.
- [37] Tien T Wang. "The segmented chirp z-transform and its application in spectrum analysis." In: *IEEE Transactions on instrumentation and measurement* 39.2 (1990), pp. 318–323.
- [38] Raoqiong Tong and Robert W Cox. "Rotation of NMR images using the 2D chirp-z transform." In: *Magnetic Resonance in Medicine: An Official Journal of the International Society for Magnetic Resonance in Medicine* 41.2 (1999), pp. 253–256.

- [39] Zongzhao Wang, Site Zhang, Olga Baladron-Zorita, Christian Hellmann, and Frank Wyrowski. "Application of the semi-analytical Fourier transform to electromagnetic modeling." In: *Opt. Express* 27.11 (2019), pp. 15335–15350.
- [40] Leonard Mandel and Emil Wolf. *Optical coherence and quantum optics*. Cambridge university press, 1995.
- [41] Claude Sabbah. "An explicit stationary phase formula for the local formal Fourier-Laplace transform." In: *arXiv preprint arXiv:0706.3570* (2007).
- [42] Jakob J Stamnes. "Waves, rays, and the method of stationary phase." In: *Optics express* 10.16 (2002), pp. 740–751.
- [43] O. Bryngdahl. "Geometrical transformations in optics." In: *JOSA* 64.8 (1974), pp. 1092–1099.
- [44] Zongzhao Wang, Olga Baladron-Zorita, Christian Hellmann, and Frank Wyrowski. "Theory and algorithm of the homeomorphic Fourier transform for optical simulations." In: *Opt. Express* 28.7 (2020), pp. 10552–10571.
- [45] Frank Wyrowski and Christian Hellmann. "The geometric Fourier transform." In: *Proc. DGO*. Vol. 118. 2017, P37.
- [46] Daniel Asoubar, Site Zhang, Frank Wyrowski, and Michael Kuhn. "Parabasal field decomposition and its application to non-paraxial propagation." In: *Opt. Express* 20.21 (2012), pp. 23502–23517.
- [47] Daniel Asoubar, Site Zhang, Frank Wyrowski, and Michael Kuhn. "Efficient semi-analytical propagation techniques for electromagnetic fields." In: *JOSA A* 31.3 (2014), pp. 591–602.
- [48] Éamon Lalor. "Conditions for the validity of the angular spectrum of plane waves." In: *JOSA* 58.9 (1968), pp. 1235–1237.
- [49] Pusheng Liu and Baida Lü. "The vectorial angular-spectrum representation and Rayleigh Sommerfeld diffraction formulae." In: *Optics & Laser Technology* 39.4 (2007), pp. 741–744.
- [50] Arnold Sommerfeld. "Lectures on theoretical physics, Vol. I." In: *I* (New York: Academic) (1964).

- [51] John C Heurtley. "Scalar Rayleigh–Sommerfeld and Kirchhoff diffraction integrals: a comparison of exact evaluations for axial points." In: *JOSA* 63.8 (1973), pp. 1003–1008.
- [52] Jan AC Veerman, Jurgen J Rusch, and H Paul Urbach. "Calculation of the Rayleigh–Sommerfeld diffraction integral by exact integration of the fast oscillating factor." In: *JOSA A* 22.4 (2005), pp. 636–646.
- [53] Fabian Shen and Anbo Wang. "Fast-Fourier-transform based numerical integration method for the Rayleigh-Sommerfeld diffraction formula." In: *Applied optics* 45.6 (2006), pp. 1102–1110.
- [54] Noé Alcalá Ochoa. "Alternative approach to evaluate the Rayleigh-Sommerfeld diffraction integrals using tilted spherical waves." In: *Optics express* 25.10 (2017), pp. 12008–12019.
- [55] Jakob J Stamnes. "Hybrid integration technique for efficient and accurate computation of diffraction integrals." In: *JOSA A* 6.9 (1989), pp. 1330–1342.
- [56] Soheil Mehrabkhani and Thomas Schneider. "Is the Rayleigh-Sommerfeld diffraction always an exact reference for high speed diffraction algorithms?" In: *Optics express* 25.24 (2017), pp. 30229–30240.
- [57] Matthias Hillenbrand, Armin Hoffmann, Damien P Kelly, and Stefan Sinzinger. "Fast nonparaxial scalar focal field calculations." In: *JOSA A* 31.6 (2014), pp. 1206–1214.
- [58] B. Richards and E. Wolf. "Electromagnetic diffraction in optical systems, II. Structure of the image field in an aplanatic system." In: *Proceedings of the Royal Society of London A: Mathematical, Physical and Engineering Sciences* 253.1274 (1959), pp. 358–379. ISSN: 0080-4630.
- [59] Luigi A D’Arcio, Joseph JM Braat, and Hans J Frankena. "Numerical evaluation of diffraction integrals for apertures of complicated shape." In: *JOSA A* 11.10 (1994), pp. 2664–2674.
- [60] Marcel Leutenegger, Ramachandra Rao, Rainer A Leitgeb, and Theo Lasser. "Fast focus field calculations." In: *Optics express* 14.23 (2006), pp. 11277–11291.

- [61] JA Koch, OL Landen, LJ Suter, and LP Masse. "Simple solution to the Fresnel–Kirchhoff diffraction integral for application to refraction-enhanced radiography." In: *JOSA A* 30.7 (2013), pp. 1460–1463.
- [62] Colin JR Sheppard. "Limitations of the paraxial Debye approximation." In: *Opt. Letters* 38.7 (2013), pp. 1074–1076.
- [63] George C Sherman and Weng Cho Chew. "Aperture and far-field distributions expressed by the Debye integral representation of focused fields." In: *JOSA* 72.8 (1982), pp. 1076–1083.
- [64] Tullio Tommasi and Bruno Bianco. "Frequency analysis of light diffraction between rotated planes." In: *Opt. Letters* 17.8 (1992), pp. 556–558.
- [65] Site Zhang, Daniel Asoubar, Christian Hellmann, and Frank Wyrowski. "Propagation of electromagnetic fields between non-parallel planes: a fully vectorial formulation and an efficient implementation." In: *Applied optics* 55.3 (2016), pp. 529–538.
- [66] Peter Debye. "Das Verhalten von Lichtwellen in der Nähe eines Brennpunktes oder einer Brennnlinie." In: *Annalen der Physik* 335.14 (1909), pp. 755–776.
- [67] Matthew R Foreman, Sherif S Sherif, Peter RT Munro, and Peter Török. "Inversion of the Debye-Wolf diffraction integral using an eigenfunction representation of the electric fields in the focal region." In: *Opt. Express* 16.7 (2008), pp. 4901–4917.
- [68] Max Born and Emil Wolf. *Principles of optics: electromagnetic theory of propagation, interference and diffraction of light*. Elsevier, 2013.
- [69] YP Kathuria. "Fresnel and far-field diffraction due to an elliptical aperture." In: *JOSA A* 2.6 (1985), pp. 852–857.
- [70] Jakob J Stamnes. *Waves in focal regions: propagation, diffraction and focusing of light, sound and water waves*. Routledge, 2017.
- [71] Jerome A Hudson. "Fresnel-Kirchhoff diffraction in optical systems: an approximate computational algorithm." In: *Applied optics* 23.14 (1984), pp. 2292–2295.

- [72] Physical optics simulation and design software "Wyrowski VirtualLab Fusion", developed by **Wyrowski Photonics UG**, distributed by **LightTrans GmbH**, Jena, Germany.
- [73] Christodoulos A Floudas and Panos M Pardalos. *Encyclopedia of optimization*. Springer Science & Business Media, 2008.
- [74] Walter F Mascarenhas. "The divergence of the BFGS and Gauss Newton methods." In: *Mathematical Programming* 147.1-2 (2014), pp. 253–276.
- [75] Ananth Ranganathan. "The levenberg-marquardt algorithm." In: *Tutorial on LM algorithm* 11.1 (2004), pp. 101–110.
- [76] Yusuf Z Umul. "Modified theory of physical optics." In: *Optics Express* 12.20 (2004), pp. 4959–4972.
- [77] Yusuf Z Umul. "Equivalent functions for the Fresnel integral." In: *Optics express* 13.21 (2005), pp. 8469–8482.
- [78] Jakob J Stamnes. "Focusing of two-dimensional waves." In: *JOSA* 71.1 (1981), pp. 15–31.
- [79] Denis Panneton, Guillaume St-Onge, Michel Piché, and Simon Thibault. "Exact vectorial model for nonparaxial focusing by arbitrary axisymmetric surfaces." In: *JOSA A* 33.5 (2016), pp. 801–810.
- [80] Alexey Andrianov, Aron Szabo, Alexander Sergeev, Arkady Kim, Vladimir Chvykov, and Mikhail Kalashnikov. "Computationally efficient method for Fourier transform of highly chirped pulses for laser and parametric amplifier modeling." In: *Optics express* 24.23 (2016), pp. 25974–25982.
- [81] Guy W. Cherry. "Integration in finite terms with special functions: the error function." In: *Journal of Symbolic Computation* 1.3 (1985), pp. 283–302.
- [82] C Van der Avoort\*, JJM Braat, P Dirksen, and AJEM Janssen. "Aberration retrieval from the intensity point-spread function in the focal region using the extended Nijboer–Zernike approach." In: *Journal of Modern Optics* 52.12 (2005), pp. 1695–1728.

- [83] E. Wolf. "Electromagnetic diffraction in optical systems - I. An integral representation of the image field." In: *Proceedings of the Royal Society of London A: Mathematical, Physical and Engineering Sciences* 253.1274 (1959), pp. 349–357. ISSN: 0080-4630.
- [84] Norman G Worku and Herbert Gross. "Propagation of truncated Gaussian beams and their application in modeling sharp-edge diffraction." In: *JOSA A* 36.5 (2019), pp. 859–868.
- [85] Zernike von F. "Beugungstheorie des schneidenverfahrens und seiner verbesserten form, der phasenkontrastmethode." In: *physica* 1.7-12 (1934), pp. 689–704.
- [86] Robert J Noll. "Zernike polynomials and atmospheric turbulence." In: *JOSA* 66.3 (1976), pp. 207–211.
- [87] Virendra N Mahajan and José Antonio Díaz. "Imaging characteristics of Zernike and annular polynomial aberrations." In: *Applied Optics* 52.10 (2013), pp. 2062–2074.
- [88] Kieran G Larkin. "Natural demodulation of two-dimensional fringe patterns. II. Stationary phase analysis of the spiral phase quadrature transform." In: *JOSA A* 18.8 (2001), pp. 1871–1881.
- [89] Robert Rolleston and Nicholas George. "Stationary phase approximations in Fresnel-zone magnitude-only reconstructions." In: *JOSA A* 4.1 (1987), pp. 148–153.
- [90] Shoshichi Kobayashi and Katsumi Nomizu. *Foundations of differential geometry*. Vol. 1. 2. New York, London, 1963.
- [91] Wolfgang Kühnel. *Differential geometry*. Vol. 77. American Mathematical Soc., 2015.
- [92] Farokh Marvasti. *Nonuniform sampling: theory and practice*. Springer Science & Business Media, 2012.
- [93] Charles A Hall and W Weston Meyer. "Optimal error bounds for cubic spline interpolation." In: *Journal of Approximation Theory* 16.2 (1976), pp. 105–122.
- [94] Philip J Davis. *Interpolation and approximation*. Courier Corporation, 1975.

- [95] Edwin Catmull and James Clark. "Recursively generated B-spline surfaces on arbitrary topological meshes." In: *Computer-aided design* 10.6 (1978), pp. 350–355.
- [96] ETY Lee. "A simplified B-spline computation routine." In: *Computing* 29.4 (1982), pp. 365–371.
- [97] Hartmut Prautzsch, Wolfgang Boehm, and Marco Paluszny. *Bézier and B-spline techniques*. Springer Science & Business Media, 2002.
- [98] Virendra N Mahajan and José A Díaz. "Comparison of geometrical and diffraction imaging in the space and frequency domains." In: *Applied optics* 55.12 (2016), pp. 3241–3250.
- [99] Jan L Bakx. "Efficient computation of optical disk readout by use of the chirp z transform." In: *Applied optics* 41.23 (2002), pp. 4897–4903.
- [100] Zhang Cao, Lijun Xu, and Jie Ding. "Integral inversion to Fraunhofer diffraction for particle sizing." In: *Applied optics* 48.25 (2009), pp. 4842–4850.
- [101] Christoph Bösel and Herbert Gross. "Compact freeform illumination system design for pattern generation with extended light sources." In: *Applied optics* 58.10 (2019), pp. 2713–2724.
- [102] Carlos J Zapata-Rodríguez. "Debye representation of dispersive focused waves." In: *JOSA A* 24.3 (2007), pp. 675–686.
- [103] Herbert Gross. "Cascaded diffraction in optical systems. Part I: simulation model." In: *JOSA A* 37.2 (2020), pp. 240–249.
- [104] Herbert Gross. "Cascaded diffraction in optical systems. Part II: example calculations." In: *JOSA A* 37.2 (2020), pp. 250–256.
- [105] Davud Hebri, Saifollah Rasouli, and Ali Mardan Dezfouli. "Theory of diffraction of vortex beams from structured apertures and generation of elegant elliptical vortex Hermite–Gaussian beams." In: *JOSA A* 36.5 (2019), pp. 839–852.
- [106] EW Marchand. "Derivation of the point spread function from the line spread function." In: *JOSA* 54.7 (1964), pp. 915–919.



- [107] Zongzhao Wang, Olga Baladron-Zorita, Christian Hellmann, and Frank Wyrowski. "Generalized Debye integral." In: *Optics Express* 28.17 (2020), pp. 24459–24470.
- [108] LN Hazra and A Guha. "Far-field diffraction properties of radial Walsh filters." In: *JOSA A* 3.6 (1986), pp. 843–846.
- [109] AI Mahan, CV Bitterli, and CG Wein. "Far-Field Diffraction and Boresight Error Properties of a Two-Dimensional Wedge." In: *JOSA* 49.6 (1959), pp. 535–556.
- [110] Peter Török, Peter R Munro, and Emmanouil E Kriezis. "Rigorous near-to far-field transformation for vectorial diffraction calculations and its numerical implementation." In: *JOSA A* 23.3 (2006), pp. 713–722.
- [111] Fred E Lytle. "An introduction to diffraction. Part II: the far field." In: *Applied Spectroscopy* 53.7 (1999), 262A–276A.
- [112] Marco Mout, Andreas Flesch, Michael Wick, Florian Bociort, Joerg Petschulat, and Paul Urbach. "Ray-based method for simulating cascaded diffraction in high-numerical-aperture systems." In: *JOSA A* 35.8 (2018), pp. 1356–1367.
- [113] Olga Baladron-Zorita, Zongzhao Wang, Christian Hellmann, and Frank Wyrowski. "Isolating the Gouy phase shift in a full physical-optics solution to the propagation problem." In: *JOSA A* 36.9 (2019), pp. 1551–1558.
- [114] David Mendlovic, Zeev Zalevsky, and Naim Konforti. "Computation considerations and fast algorithms for calculating the diffraction integral." In: *Journal of Modern Optics* 44.2 (1997), pp. 407–414.
- [115] Kenneth George Binmore and Kenneth George Binmore. *Mathematical Analysis: a straightforward approach*. Cambridge University Press, 1982.



## LIST OF FIGURES

---

Figure 1	Illustration of the physical-optics modeling of a light path by a field-tracing diagram. . . . .	4
Figure 2	Extraction of the quadratic phase from a general function .	19
Figure 3	Field distribution of a truncated Laguerre Gaussian 01-mode at the waist plane . . . . .	24
Figure 4	Semi-analytical Fourier transform of a truncated Laguerre Gaussian 01-mode with a purely quadratic phase . . . . .	25
Figure 5	Semi-analytical Fourier transform of a field with a spherical phase, part I . . . . .	28
Figure 6	Semi-analytical Fourier transform of a field with a spherical phase, part II . . . . .	29
Figure 7	Semi-analytical Fourier transform of a field with a general wavefront phase . . . . .	30
Figure 8	Illustration of the relationship between the geometric shape and the second fundamental form of a smooth parametric surface . . . . .	36
Figure 9	Fast Fourier transform of a field with house-shaped amplitude and different values of the spherical-phase radius. . . . .	46
Figure 10	Homeomorphic Fourier transform of the same house-shaped amplitude with a superimposed spherical phase . . . . .	47
Figure 11	Comparison of the numerical effort of the homeomorphic and the Fast Fourier transforms for the case of a house-shaped field with a spherical phase . . . . .	49
Figure 12	Homeomorphic Fourier transform of a field with amplitude shaped in the form of a letter sequence spelling "Light" . . . . .	52
Figure 13	Homeomorphic Fourier transform of a field with a general bijective wavefront phase. . . . .	55
Figure 14	Fourier transform of a field with a non-bijective wavefront phase . . . . .	58

Figure 15	Analysis of the wavefront phase for the simulation task: Homeomorphic Fourier transform of a field with a non- bijective wavefront phase . . . . .	59
Figure 16	Sketch of the simulation setup: divergent beam incidents a surface with some local defect . . . . .	60
Figure 17	Fourier transform of a field with a non-bijective wavefront phase. . . . .	61
Figure 18	Propagation of a light field to a tilted plane . . . . .	69
Figure 19	The field-tracing diagram of the free space propagation between two arbitrarily oriented planes . . . . .	71
Figure 20	Illustration of the Debye integral . . . . .	73
Figure 21	Illustration of the far-field integral . . . . .	77
Figure 22	Comparison of accuracy between the unified free space propagation operator and the standard Debye integral . .	89
Figure 23	Accuracy curves of the unified free space propagation op- erator and the standard Debye integral . . . . .	90
Figure 24	Illustration of the simulation task: propagation of an aber- rant divergent beam . . . . .	92
Figure 25	Comparison of the accuracy: deviation vs. the scaling fac- tor of the aberrant phase . . . . .	94
Figure 26	Comparison of the accuracy: deviation vs. propagation distance . . . . .	95
Figure 27	Simulation result for the simulation task: propagation to inclined planes . . . . .	97
Figure 28	Spherical phase function and its partial derivative functions.	102
Figure 29	First derivatives of the spherical phase function. . . . .	103
Figure 30	Example of the third kind of smooth function phase. . . .	104

## LIST OF TABLES

---

Table 1	Comparison of the required sampling points for the Fourier transform of a truncated Laguerre Gaussian mode . . . . .	26
Table 2	Comparison of the required sampling points for the Fourier transform of truncated spherical wave . . . . .	27
Table 3	Simulation parameters of the general wavefront phase for the example presented in Section 2.2.3. . . . .	30
Table 4	Physical implications of the amplitude scaling factor of the forward homeomorphic Fourier transform. . . . .	37
Table 5	Physical implications of the amplitude scaling factor for the inverse homeomorphic Fourier transform. . . . .	39
Table 6	Comparison of the homeomorphic Fourier transform and the fast Fourier transform: number of sampling points and deviation . . . . .	48
Table 7	Simulation parameters of the aberrant phase for the example presented in Section 3.2.2. . . . .	52
Table 8	Simulation parameters of the aberrant phase for the example in Section 3.2.3. . . . .	54
Table 9	Simulation parameters of the aberrant phase for the first example in Section 3.2.4. . . . .	57
Table 10	Wavefront phase parameters of the incident field in front of the interface for the second example in Section 3.2.4. . .	62
Table 11	Physical interpretation of different propagation integrals .	87
Table 12	Simulation parameters of the aberrant phase for the example presented in Section 4.4.1. . . . .	88
Table 13	Simulation parameters of the aberrant phase $\psi^{\text{zer}}(\rho)$ for the first example presented in Section. 4.4.2. . . . .	93
Table 14	Simulation parameters of the primary spherical phase and the aberrant phase for the second example presented in Section. 4.4.2. . . . .	96



## ACKNOWLEDGEMENTS

---

First of all, I would like to thank my supervisor Prof. Dr. Frank Wyrowski, for his constant encouragement and precious advice. During my Ph.D. study in the past years, his unique insights on physical optics profoundly inspired me so as to enhance my ability to analyze and solve problems. When I encounter the bottleneck, Frank can always motivate me with his helpful suggestions and critical comments. I enjoy the fruitful discussions with him.

Also, I would like to express my great thanks to Mr. Christian Hellmann and Mr. Torsten Schöning. They generously shared their experience in programming and imparted knowledge in software technologies. I benefited so much from every conversation with them. Furthermore, many thanks go to my colleagues in the Applied Computational Optics Group. Dr. Site Zhang and Ms. Olga Baladron-Zorita cooperated with me on several research projects. I appreciate their professional support and help in academic writing. In the same way, I would like to thank Huiying Zhong, Rui Shi, Liangxin Yang, Dominik Kuhn, and Irfan Badar. These warm-heart colleagues establish a great working environment and create an energetic atmosphere in the group.

Finally, I must offer my faithful thanks to my parents and twin brother. With their constant support and unending patience, I can bravely overcome all difficulties in the oversea study.



## PUBLICATIONS

---

### JOURNAL ARTICLES

1. **Zongzhao Wang**, Site Zhang, Olga Baladron-Zorita, Christian Hellmann and Frank Wyrowski. "Application of the semi-analytical Fourier transform to electromagnetic modeling." In: *Opt. Express* 27.11 (2019), pp. 15335-15350.
2. **Zongzhao Wang**, Olga Baladron-Zorita, Christian Hellmann and Frank Wyrowski. "Theory and algorithm of the homeomorphic Fourier transform for optical simulations." In: *Opt. Express* 28.7 (2020), pp. 10552-10571.
3. **Zongzhao Wang**, Olga Baladron-Zorita, Christian Hellmann and Frank Wyrowski. "Generalized Debye integral." In: *Opt. Express* 28.17 (2020), pp. 24459-24470.
4. **Zongzhao Wang**, Olga Baladron-Zorita, Christian Hellmann and Frank Wyrowski. "Generalized far-field integral." In: *Opt. Express* 29.2 (2021), pp. 1774-1787.
5. Olga Baladron-Zorita, **Zongzhao Wang**, Christian Hellmann and Frank Wyrowski. "Isolating the Gouy phase shift in a full physical-optics solution to the propagation problem." *J. Opt. Soc. Am. A* 36.9 (2019), pp. 1551-1558.
6. Rui Shi, **Zongzhao Wang**, Shih-Te Hung, Christian Hellmann and Frank Wyrowski. "Numerical analysis of tiny-focal-spot generation by focusing linearly, circularly, and radially polarized beams through a micro/nanoparticle." In: *Opt. Express* 29.2 (2021), pp. 2332-2347.

## CONFERENCE PROCEEDINGS

1. **Zongzhao Wang**, Huiying Zhong and Frank Wyrowski. "Rigorous modeling of dispersive, reflective, and polarization prisms." *Deutsche Gesellschaft für angewandte Optik-116. Jahrestagung*, 2015.
2. **Zongzhao Wang**, Site Zhang, and Frank Wyrowski. "Modeling laser beam propagation through components with internal multiple reflections." In: *Components and Packaging for Laser Systems* (Vol. 9346, p. 934616). International Society for Optics and Photonics, 2015.
3. Site Zhang, **Zongzhao Wang** and Frank Wyrowski. "Generation of complex light using uniaxial and biaxial crystals: an efficient and accurate vectorial simulation technique." *Complex Light and Optical Forces X* (Vol. 9764, p. 97640I). International Society for Optics and Photonics, 2016.

## ORAL PRESENTATION

1. **Zongzhao Wang**, Site Zhang, Olga Baladron-Zorita, Christian Hellmann and Frank Wyrowski. "Semi-analytical Fourier transform and its application to physical-optics modelling." *SPIE Optical Systems Design*, Frankfurt am Main, Germany, 2018.
2. **Zongzhao Wang**, Olga Baladron-Zorita, Christian Hellmann and Frank Wyrowski. "Numerical implementation of the homeomorphic Fourier transform and its application to physical-optics modeling." *EOS Topical Meeting on Diffractive Optics*, Jena, Germany, 2019.



## EHRENWÖRTLICHE ERKLÄRUNG

---

Ich erkläre hiermit ehrenwörtlich, dass ich die vorliegende Arbeit selbständig, ohne unzulässige Hilfe Dritter und ohne Benutzung anderer als der angegebenen Hilfsmittel und Literatur angefertigt habe. Die aus anderen Quellen direkt oder indirekt übernommenen Daten und Konzepte sind unter Angabe der Quelle gekennzeichnet.

Bei der Auswahl und Auswertung folgenden Materials haben mir die nachstehend aufgeführten Personen in der jeweils beschriebenen Weise unentgeltlich geholfen:

- Herr Prof. Dr. Frank Wyrowski als Betreuer dieser Arbeit.

Weitere Personen waren an der inhaltlich-materiellen Erstellung der vorliegenden Arbeit nicht beteiligt. Insbesondere habe ich hierfür nicht die entgeltliche Hilfe von Vermittlungs-bzw. Beratungsdiensten (Promotionsberater oder andere Personen) in Anspruch genommen. Niemand hat von mir unmittelbar oder mittelbar geldwerte Leistungen für Arbeiten erhalten, die im Zusammenhang mit dem Inhalt der vorgelegten Dissertation stehen.

Die Arbeit wurde bisher weder im In- noch im Ausland in gleicher oder ähnlicher Form einer anderen Prüfungsbehörde vorgelegt. Die geltende Promotionsordnung der Physikalisch-Astronomischen Fakultät ist mir bekannt. Ich versichere ehrenwörtlich, dass ich nach bestem Wissen die reine Wahrheit gesagt und nichts verschwiegen habe.

*Ort, Datum*

---

Unterschrift